Optimizing Analysis Standards for Pulsar Timing Arrays and Gravitational Wave Detection

Jun Wang

Supervisor: Prof. Dr. Joris P. W. Verbiest

Faculty of Physics
Bielefeld University

This dissertation is submitted for the degree of
Doctor of Philosophy

Bielefeld October 2021

Supervisor:
Prof. Dr. Joris Verbiest

Thesis Defense Committee:
Prof. Dr. Walter Pfeiffer [Chair]
Prof. Dr. Joris Verbiest [Supervisor]
Prof. Dr. Dominik Schwarz
Prof. Dr. Jürgen Schnack

Printed on permanent paper °° ISO 9706

Dedicated to my family.

Declaration

I hereby declare that except where specific reference is made to the work of others, the contents of this dissertation are original and have not been submitted in whole or in part for consideration for any other degree or qualification in this, or any other university.

Jun Wang
October 2021

Acknowledgements

The way to pursue a doctorate is a kind of spiritual practice. The result is important, but what really matters are the research habits and academic vision I cultivated during this journey. It is a really good fortune to meet so many interesting people during the past three years.

First of all, I would like to express my heartfelt thanks to my supervisor, Prof. Dr. Joris P. W. Verbiest. I really appreciate him for accepting me into this excellent research group and supporting me every step since then. I can still remember the day when I arrived in Germany when Joris and his whole family picked me up at the train station and took me to my new home, I was deeply moved. As I struggle through the initial adaptation to living in a totally different culture and language environment, Joris help me to go through that period with his meticulous care and concern. Also, alone my whole doctorate study period, Joris also provided his detailed guidance and assistance. I am really fortunate to have Joris as my "Doktorvater".

Secondly, I am very grateful to Dr. Golam Shaifullah, who has provided a lot of constructive suggestions and help in my research work. At the same time, he used his rich scientific research experience to tell me how to analyze data and how to write scientific papers. In addition, he also spent a lot of precious time proofreading and revising my paper.

Furthermore, I also need to express my appreciation to Dr. Caterina Tiburzi, whose enthusiastic help made me learn a lot of basic knowledge in pulsar timing. Except for Joris and myself, she is the only non-German member in our group. In the first several weeks, it is hard for me to get used to her accent, but she is always so kind to me and patiently explaining to me what pulsar timing is and how it works.

Special thanks to other members of our radio astronomy group. Thank you, to Julian Donner for your frank advice and willingness to help me with the dispersion measure variation measurement and software usage, and to Lars Künkel for providing and teaching me to use his radio frequency interference mitigation code. To my fellow students, Yulan Liu, Ziwei Wu, Philip Bergjann, and Bilel Ben Salem, thank you for your help and support in both science and life here.

Throughout my Ph.D. research, I had been actively participating in the European Pulsar Timing Array (EPTA), and thus learned a lot from my EPTA collaborators, especially from

Dr. Gemma Janssen of the Netherlands Institute for Radio Astronomy (ASTRON), Dr. Kuo Liu, Huanchen Hu and Dr. James McKee of the Max Planck Institute for Radio Astronomy (MPIfR), Prof. Dr. Ben Stappers, Dr. Michael Keith and Lin Wang of the Jodrell Bank Centre for Astrophysics, and Dr. Lucas Guillemot of the Radiotélescope de Nançay. I have benefited tremendously from them through daily contact and semiannual EPTA meeting. EPTA is a broad platform with plenty of opportunities, where we can share our thoughts and improve mutually.

Over the years, I have been very grateful to Susi Reder and Dr. Jörn Künsemöller, without whose patient assistance in administrative and technical support respectively, I may not have settled down in Bielefeld so easily. To Susi, thanks for your assistance both in living and administration, which helped me to save a lot of time and energy for scientific research. To Jörn, thanks for your assistance in software installation and coding, I learned a lot from you.

I also thank the members of my dissertation committee: Prof. Dr. Jürgen Schnack, Prof. Dr. Dominik Schwarz, and Prof. Dr. Walter Pfeiffer for their helpful comments and advice about this work.

To my parents, thanks for your silent support and dedication behind. My siblings Lulu and Qianqian, who always believe in me and unconditionally support me. Thanks for your company by our parents when I was studying abroad. I love you all forever.

Last but definitely not least, Jingya has been my constant companion throughout my graduate career, providing love, trust, as well as the necessary encouragement for me to see this to completion.

Abstract

Pulsars are super dense, highly magnetized, and rapidly rotating neutron stars (NSs) that emit electromagnetic (EM) radiation from their magnetic poles. Ideally, when the emission beam sweeps across the Earth, we can detect a pulse of radiation. Due to their short and stable pulse periods, pulsars can be used for a variety of studies. In particular, a set of the most stable millisecond pulsars (MSPs) can be used to detect nanohertz gravitational waves (GWs) produced by super-massive black holes. The eventual detection of these GWs highly relies on the pulsar timing precision.

In this dissertation, I investigate the timing precision potential of European pulsar timing array (EPTA) telescopes equipped with the newest back-ends and study the noise floor for 16 pulsars observed by four EPTA telescopes. A practical demonstration is first presented with three MSPs. Our demonstration shows that data-derived and smoothed templates are typically preferred to some more commonly applied alternatives; the Fourier-domain with Markov-chain Monte Carlo (FDM) template-matching algorithm is generally superior to or competitive with other algorithms. To verify our conclusions, a confirmatory test was then performed with a larger dataset, data of 13 EPTA MSPs are utilized in this work. Based on this work, I refined the above-mentioned conclusions. I noticed that for some extreme cases, such as extremely low S/N or too few TOAs, other combinations may work better. In addition, the added templates combined with the FDM template-matching method are usually superior to other possibilities. The effect of pulse phase jitter noise is not a serious factor that influences the EPTA timing precision, since the jitter levels I derived are far smaller than the radiometer noise. The system-limited noise floor was shown to be above the jitter-noise level and it was found to be significantly different between telescopes.

At the end of this thesis, I analyze the low-frequency noise of the selected six pulsar data obtained with the EPTA telescopes and compare our results with the finalized common-noise analysis led by the EPTA community. Our results show that data are less discriminant between the models than the EPTA data. I have a clear detection of red noise, but I cannot determine if it's a GWB or timing noise, or both.

Table of contents

List of figures

List of tables

Nomenclature

Astronomical / Physical Constants

c	Speed of light	$2.998 \times 10^{8}\ \mathrm{m\,s^{-1}}$
e	Elementary charge	$1.602 \times 10^{-19}\ \mathrm{C}$
G	Gravitational constant	$6.670 \times 10^{-11}\ \mathrm{m^{3}\,kg^{-1}\,s}$
m_e	Electron mass	$9.109 \times 10^{-31}\ \mathrm{kg}$
$M_\odot$	Solar mass	$1.989 \times 10^{30}\ \mathrm{kg}$
1 AU	Astronomical unit	$1.496 \times 10^{11}\ \mathrm{m}$
1 Jy	Jansky	$10 \times 26\ \mathrm{W\,m^{-2}\,Hz^{-1}}$
1 pc	Parsec	$3.086 \times 10^{16}\ \mathrm{m}$
1 yr	Julian year	$3.156 \times 10^{7}\ \mathrm{s}$

Numerical Constants

π	= 3.14159
e	= 2.71828
1 rad	= 57.296°

Acronyms / Abbreviations

ADC	Analog-to-Digital Converter
BAT	Barycentric Arrival Time
BH	Black Hole

BIPM	Bureau International des Poids et Mesures
CCA	Cross Correlation Algorithm
DM	Dispersion Measure
DNS	Double Neutron Star
EM	Electromagnetic
EPTA	European Pulsar Timing Array
FDM	Fourier Domain with Markov chain Monte Carlo
GIS	Gaussian Interpolation Shif
GR	General Relativity
GW	Gravitational Wave
GWB	Gravitational Wave Background
HD	Hellings-Downs
IISM	Ionized Interstellar Medium
IPTA	International Pulsar Timing Array
JPL	Jet Propulsion Laboratory
LIGO	Laser Interferometer Gravitational-wave Observatory
LISA	Laser Interferometer Space Antenna
LNA	Low-Noise Amplifier
LOS	Line of Sight
MCMC	Markov Chain Monte Carlo
MJD	Modified Julian Dates
MS	Main Sequence
MSP	Millisecond Pulsar
NANOGrav	North American Nanohertz Observatory for Gravitational Waves

NIST	National Institute of Standard and Technology
NS	Neutron Star
PGS	Fourier Phase Gradient
PPTA	Parkes Pulsar Timing Array
PTA	Pulsar Timing Array
RFI	Radio Frequency Interference
RM	Rotation Measure
RMS	Root Mean Square
RRAT	Rotating Radio Transient
S/N	Signal-to-Noise Ratio
SAT	Site Arrival Times
SEFD	System Equivalent Flux Density
SLNF	System Limited Noise Floor
SMBHB	Super-Massive Black Hole Binary
SSB	Solar System Barycentre
SSE	Solar System Ephemeris
SW	Solar Wind
SWIMS	Stochastic Wide-band Impulse Modulated Self-noise
TAI	International Atomic Time
TOA	Time of Arrival
TT	Terrestrial Time
UTC	Universal Coordinated Time
WD	White Dwarf

Chapter 1

Introduction

Pulsars are highly magnetized and fast-spinning neutron stars (NSs). A NS is a super dense star, with its density generally up to 10^{17} kg m^{-3}. When Baade & Zwicky (1934) first proposed the idea that a supernova explosion can transform an ordinary star into a NS, almost no one at that time thought that we could observe them. However, the discovery of NSs happened by accident after more than 30 years. The first pulsar, PSR J1921+2153, was discovered by Hewish et al. (1968). Although Pacini (1967) predicted that NSs can radiate energy through magnetic dipole radiation, he also expected the radiation to be undetectable due to reflections by the circumstellar gas. It was not until the discoveries of the Vela (PSR J0813−4510, Large et al., 1968) and the Crab (PSR J0534+2200, Staelin & Reifenstein, 1968) pulsars, both with pulse periods less than 100 ms, that the sources of the periodic signal were confirmed as rapidly rotating NSs (Gold, 1968).

The discovery of pulsars and confirmation that pulsars are extremely dense, highly magnetized and fast-rotating NSs soon made pulsars ideal celestial laboratories for a rich variety of astrophysical experiments, and thus opened the door to pulsar astronomy.

In this chapter, I will give an overview of pulsars, introducing their formation, discovery history, basic characteristics and their applications in both astronomy and physics. I first introduce the concept and properties of pulsars in Section 1.1. Section 1.2 discussed how the interstellar medium affects our observations of pulsars. Finally, Section 1.3 describes how pulsars can be used in Gravitational Wave (GW) astronomy.

1.1 Pulsars and Millisecond Pulsars

Pulsars are super-dense rapidly spinning remnants from supernova explosions (Baade & Zwicky, 1934). Their formation is a comprehensive action of several forces. Besides, they can be divided into different types according to different characteristics. For example, they

can be classified as optical, radio, X-ray and γ-ray pulsars according to the frequency of observation. Normally in the radio pulsar timing realm, pulsar can be divided into two distinct groups: normal pulsars (also referred to as canonical pulsars, pulsars with a spin period larger than 30 ms) and millisecond pulsars (MSPs, with a spin period less than 30 ms, Alpar et al., 1982).

In this section, I will introduce the basic properties of pulsars. I will first discuss the origins of pulsars, followed by the history of the discovery of the first pulsar. Then, several typical kinds of pulsars will be introduced. Finally, I will give an overview of the properties of pulsars.

1.1.1 Pulsar Formation

Like the Sun, most of the stars in the Universe are powered by hydrogen. Normally, the main sequence (MS) star forms a self-regulating system in hydrostatic equilibrium provided by two opposite forces: the outward radiation pressure due to nuclear fusion (Russell, 1931), which pushes inner masses up to the surface of the star, and the inward pressure due to gravity, which attract everything back to the center.

As the star evolves, it continues fusing hydrogen into helium, but along with the consumption of hydrogen, the outward radiation pressure decreases, thus leading to the core gradually contracting due to gravity. The compression of the core causes the core temperature to rise and then the core will begin to fuse helium. When an MS star runs out of light nuclei in the core, and the fusion of heavy nuclei becomes hard and unsustainable, the star will reach its end of life. But what it could turn to depends on its original mass. Partially, there are three main types for its destination.

If the mass of the progenitor is not large enough ($\leq$ 8 solar masses, $M_\odot$), the fusion will stop at carbon and oxygen, the gravitational collapse of the core will be halted due to electron degeneracy pressure, leading to the formation of a white dwarf (WD). If the star's mass beyond 10 $M_\odot$ (Prialnik, 2000), the fusion process will be terminated at iron. Since fusing iron is no longer exothermic but endothermic, iron cannot be fused into anything heavier. The core masses of these massive stars will eventually exceed the Chandrasekhar limit (Chandrasekhar, 1931), of approximately 1.4 $M_\odot$. The core collapse process will not be halted by the electron degeneracy pressure anymore. Instead, the Fermi energy (Fermi, 1926) of the electrons will increase significantly, enough to combine electrons with protons to create neutrons (via inverse beta decay). Just as WDs are sustained by electron degeneracy pressure, a phenomenon described by the Pauli exclusion principle (Pauli, 1925), NSs are similarly supported against further collapse by the neutron degeneracy pressure. Analogous to the Chandrasekhar limit for an electron degenerate object, there is also an upper bound

to the mass of neutron degenerate objects, referred to as the Tolman–Oppenheimer–Volkoff limit (Oppenheimer & Volkoff, 1939; Tolman, 1939). The most massive stars ($\gtrsim 20M_{\odot}$) can break through this limitation and keep on collapsing until forming a black hole (BH). The gravity near a BH is too strong to let particles and electromagnetic (EM) radiation escape from it.

As illustrated in Figure 1.1, the generally accepted pulsar geometry model is analogous to the 'lighthouse' model. NSs are born highly energetic, with high angular momentum retained. Since they also have a quite small radius, they tend to rotate with a very small period. A beam of radiation is emitted along the magnetic axis of the pulsar, but since the magnetic axis and the rotation axis are in general misaligned, the beam sweeps through space like the beam of a lighthouse.

1.1.2 The Discovery of Pulsars

The existence of NSs was first hypothesized by Baade & Zwicky (1934), not long after the discovery of the neutron. They suspected that after nuclear fusion ends, massive stars will undergo a supernova explosion and become NSs, which were predicted to be extremely dense, fast-spinning, with a tiny radius of the order of $\sim$10 km (Lattimer & Prakash, 2001), and to possess strong magnetic fields. However, at that time, they thought it was impossible to detect NSs with Earth-based telescopes. This opinion was revised in 1967 when Pacini (1967) put forward the concept that fast-rotating NSs with strong magnetic fields could emit EM radiation (as shown in Figure 1.2). He also suspected that this rotational energy could be released to a supernova remnant around it. It was not until the first discovery of PSR B1919+21 (also known as PSR J1921+2153) by Hewish et al. (1968) that astronomers finally reached an agreement that pulsars are rotating NSs and thus NSs are detectable.

Unlike other targeted scientific discoveries, the discovery of the first pulsar was serendipitous. On November 28, 1967, when Jocelyn Bell was analyzing the interplanetary scintillation data from the Interplanetary Scintillation Array of the Mullard Radio Astronomy Observatory, she noticed small periodic pulses of radiation when their telescope was looking at a particular area of the sky. After ruling out man-made radio frequency interference (RFI) and scintillation effects, still, some periodic "scruff" signals remained. Subsequent observations and analysis of this source showed that this signal kept sidereal time, suggesting that the signal originated from an extra-terrestrial source (Hewish et al., 1968). This pulsating source was later confirmed as a rotating NS and soon opened the prologue of pulsar astronomy. This first discovered PSR J1921+2153[1], also known as CP 1919 [2], is a NS with a period of 1.3373

[1] PSR represents "Pulsating Radio Source"

[2] which stands for Cambridge Pulsar at right ascension 19h 19m

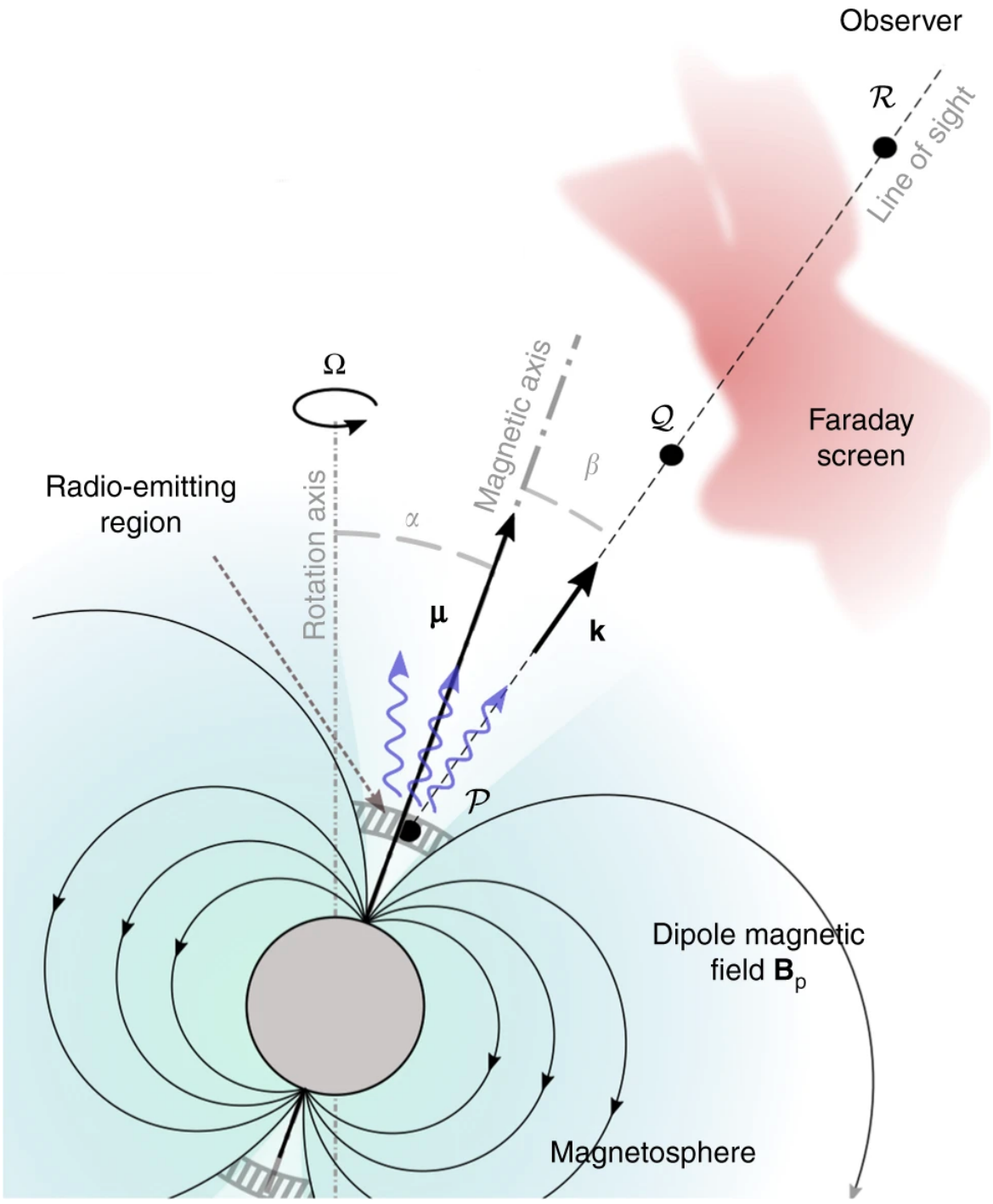

Figure 1.1 The Pulsar geometry: The magnetic axis is inclined to the rotational axis at an angle α and an observer views the phenomenon at an angle $(\alpha + \beta)$ to the rotation axis. Figure credit: Fig. 1 of Gueroult et al. (2019).

seconds and a pulse width of 0.04 seconds. In 1974, due to his decisive role in the discovery of pulsars, Antony Hewish was awarded the Nobel Prize in Physics.

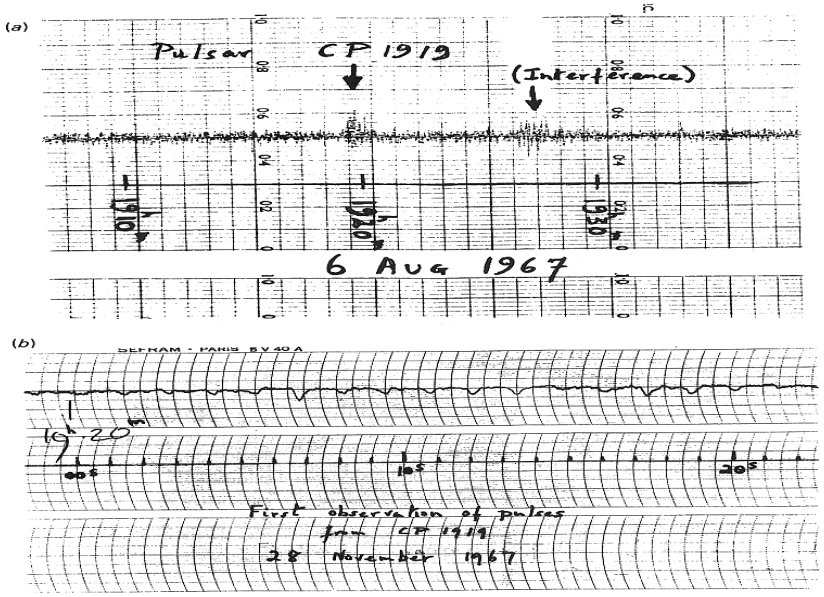

Figure 1.2 Discovery observations of the first pulsar: B1919+21. (a) The first recording of PSR B1919+21; the signal resembled radio interference also seen on the same plot. (b) Fast chart recording showing individual pulses.
Figure credit: Hewish et al. (1968)

The discovery of the first pulsar attracted more efforts on pulsar searches and pulsar surveys. For example, Pilkington et al. (1968) announced three new pulsars in the same year. Several hypotheses had been put forward straight after the discovery, such as pulsating (Hewish et al., 1968), rotating (Gold, 1968; Ostriker, 1968), and orbiting Saslaw et al. (1968) NSs or WDs. But the pulsating and rotating WDs and NSs hypothese were soon negated after the discovery of faster-rotating pulsars, i.e. the Vela and the Crab pulsar.

1.1.3 Binary and Millisecond Pulsars

So far, there are 2872 pulsars observed, according to the ATNF Pulsar Catalog (v.1.64, Manchester et al., 2005). Similar to the Hertzsprung-Russell diagram, the $P-\dot{P}$ diagram is commonly adopted in pulsar astronomy to demonstrate the evolution of NSs. The majority of the pulsar population is classified as 'normal' pulsar, usually with a spin period, P, between 0.1-10 s, the first derivative of the spin period, $\dot{P} > 10^{-17}\mathrm{s}^{-1}$, and magnetic field strengths of $B_s \sim 10^{10-13}$ G.

Among the huge number of discovered pulsars, in the lower-left part of figure 1.3, there is one typical kind of pulsar, which is commonly a binary pulsar. As can be seen from

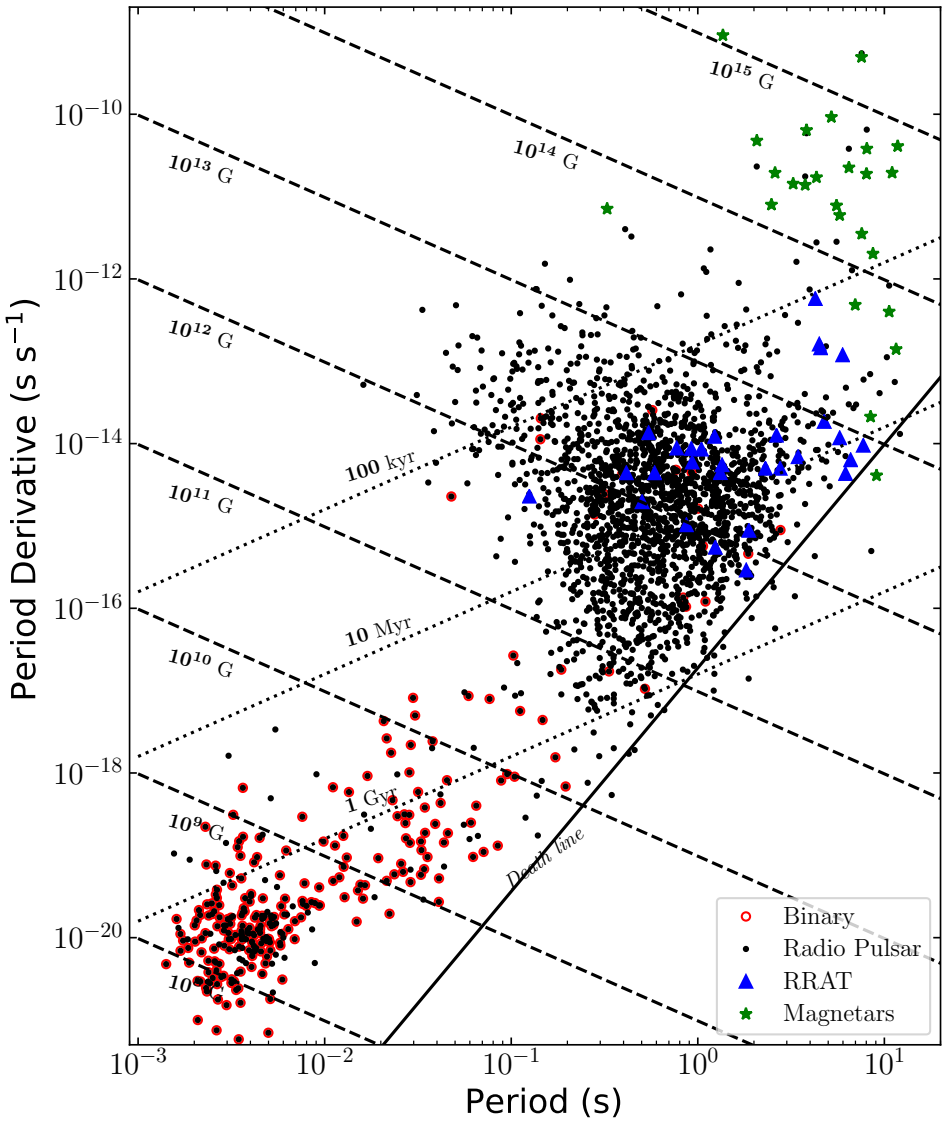

Figure 1.3 $P - \dot{P}$ Diagram created of all known pulsars available in the ATNF pulsar catalog[a] (PSRCAT v1.64; Manchester et al., 2005). In addition, pulsars in binary system are presented with red circles, magnetars listed in the McGill Online Magnetar Catalog[b] are shown with green stars and RRATs listed in the RRATalog[c] are plotted with blue triangles. Inclined dotted lines represent the characteristic age (τ_c) of the pulsars, the dashed lines show the surface magnetic field strength (B_s) and the pulsar death line proposed by Chen & Ruderman (1993) is shown ass a solid line.

[a] http://www.atnf.csiro.au/research/pulsar/psrcat
[b] http://www.physics.mcgill.ca/~pulsar/magnetar/main.html
[c] http://astro.phys.wvu.edu/rratalog

their name, binary pulsars are pulsars in binary systems, usually accompanied by a WD, another NS, or even less likely, another pulsar. Binary pulsars are ideal laboratories that allow physicists and astronomers to test general relativity (GR) due to the strong gravitational fields involved. The first binary pulsar PSR J1915+1606 (also known as PSR B1913+16) was discovered by Hulse & Taylor (1975). It is a pulsar accompanied by another NS, the orbital period of this binary system is 7.75 hours long and both of these two stars are determined to have approximately equal mass, that is 1.4 $M_{\odot}$ (Weisberg et al., 2010).

In 1916, Albert Einstein first predicted the existence of GWs in his GR theory. GWs are generated by accelerated masses and propagate outward in waveform with the speed of light. There are many cataclysmic events in the universe, such as BHs coalescing, massive stars exploding (supernovae) and NS mergers, all of which could produce strong GWs. As BHs and NSs are normally far away from the Earth, the amplitude of these waves is too tiny to be detected. However, things changed after the discovery of the binary pulsar: PSR B1913+16. Einstein's GR predicts that the binary system will lose mass due to the orbit around the common center of mass. The lost energy will be emitted away in the form of GWs. After a high precision pulsar timing analysis of PSR B1913+16, it can be noticed that their orbital period is decaying in precise agreement with that predicted from the GW emission model described by Einstein's GR (Hulse & Taylor, 1975; Weisberg et al., 2010).

Another special kind of pulsars are MSPs. Just as their name implies, MSPs are usually pulsars that have been spun up or "recycled" to rotational periods shorter than $\sim$30 milliseconds through the accretion of matter from their binary companion star (Alpar et al., 1982; Bhattacharya & van den Heuvel, 1991).

In 1982, the first MSP, PSR B1937+21 (also called PSR J1939+2134) was discovered by Backer et al. (1982). This pulsar, located in the sky a few degrees away from the first discovered pulsar, PSR B1919+21, spins around 641 times per second which equals a rotational period of 1.56 ms. The fastest-spinning pulsar is PSR J1748$-$2446ad, an MSP spinning 716 times per second (Hessels et al., 2006). However, it is believed that there should be an upper limit to the spin rate. It is deduced that pulsars would be flung apart by the centrifugal force if they spun at a rate of 1000-1500 rotations per second (Chakrabarty et al., 2003; Cook et al., 1994; Miller & Miller, 2015; Patruno et al., 2017).

The most noticeable property of MSPs is their spin stability, which is comparable to atomic clocks over a longer period of time. By using these high-precision timekeepers, we can investigate stellar evolution, the ionized interstellar medium (IISM), and even the essence of space-time. Since the pulses emitted from the pulsars are so reliable, a tiny deviation of the pulses' arrival time, their intensity, or profile variations could help us to understand the

details as well as the changes around the pulsar or the IISM environment between the pulsar and the Earth.

According to recent research (e.g. Alpar et al., 1982; Bhattacharya & van den Heuvel, 1991), MSPs are referred to as recycled pulsars because they are created by the recycling of an old, slowly rotating and even dead pulsar via accretion of mass and angular momentum from its binary companion (Alpar et al., 1982; Radhakrishnan & Srinivasan, 1981). That's to say, MSPs usually evolved in a binary system, some isolated MSPs may have lost their companions due to its violent supernova explosion (Fruchter et al., 1988; Tauris & Takens, 1998). Most of the known binary MSPs have either WDs or smaller companions. If the angular momentum gain from the accretion is larger than the energy lost due to the emission process, the pulsar will spin up (Bhattacharya & van den Heuvel, 1991). This recycling process will also result in the decrease of strength of the pulsar's magnetic field and the period derivative (Bhadra, 2002; Shibazaki et al., 1989).

In addition to the two kinds of pulsars mentioned above, there are several other kinds of extreme neutron stars, such as Rotating Radio Transients (RRATs) and magnetars. RRATs are generally considered as a type of pulsar that emits radio bursts with irregular intervals, and they were first discovered by McLaughlin et al. (2006). Magnetars are thought to be NSs with an extremely strong magnetic field ($10^{14} - 10^{15}$ G) and a long rotation period (Duncan & Thompson, 1992; Kaspi & Beloborodov, 2017). Most magnetars are discovered through their short X-ray bursts. According to recent research (e.g., Bochenek et al., 2020; CHIME/FRB Collaboration et al., 2020; Zhang, 2020), magnetars are associated with fast radio bursts (Lorimer et al., 2007).

Since MSPs have extremely stable spin periods, various efforts have been take to test fundamental physics through pulsar timing research.

1.1.4 Pulsar Properties

Research on pulsars has flourished since their discovery in 1967. Pulsars have been found to be observable in all EM spectral bands, but the typical frequencies we can observe with ground-based telescopes are between 1 GHz and 2 GHz, at radio wavelengths. Throughout this thesis, I will only discuss radio pulsars, which constitute the overwhelming majority of all pulsars. As introduced above, pulsars are super-dense core remnants of supernova explosions and are in a state of equilibrium between outward pressure and inward gravity. Since the fast-spinning pulsars are emitting radiation from their magnetic poles and this radiation can be detected with telescopes, we can study some fundamental properties, and a full understanding of the properties would be of great use for exploring the mysterious universe. In this section, I will discuss some of these properties, namely pulse profiles, the

spin-down energy loss rate and the characteristic age, characteristic surface magnetic field strength, and flux density.

1.1.4.1 Pulse Profiles

Pulsar signals are very weak EM radiation. Although there are some bright pulsars or giant pulses of normal pulsars which are easily detectable, for most pulsars, the individual pulses are too weak to be detected or distinguished from noise. For the detectable single pulses, the individual pulses also vary noticeably. A detailed understanding of the pulsar emission mechanism can be obtained by investigating single pulses and their behaviors over time and frequency. Due to the single pulse profile variation, we can investigate the pulse profile stochastic variability in both amplitude and phase: stochastic wide-band impulse modulated self-noise (SWIMS Osłowski et al., 2011), giant pulses (Knight et al., 2006), mode changing (Backer, 1970), nulling (Wang et al., 2007) and drifting (Drake & Craft, 1968).

For most pulsars, single-pulse studies are unrealistic. But one remarkable thing about pulse profiles is that the integrated profiles, produced through the addition of thousands of single pulses, are stable and much easier to be detected (Liu et al., 2012). The stability of this "integrated" profile is of great importance to pulsar timing and nanohertz GW detection. Also, the integrated profile is a unique identifier of pulsars, since the integrated profile is a fingerprint of the pulsar emission mechanism, influenced by the pulsar's magnetosphere and the IISM it passed through. We can identify a pulsar by just looking at its integrated profile.

While the shape of the integrated pulse profiles is extremely stable at specific frequencies, in some cases we can still notice temporal variations as well as frequency-dependent pulse shape evolution. The temporal variations are thought to be caused by either mode changes, where the integrated profile switches between two or more quasi-stable modes, or the relativistic effect of geodetic precession, which occurs in one component of a binary system when the spin angular momentum vector of that component is misaligned with the orbital angular momentum vector (Bailes, 1988). Mode changing, first discovered by Backer (1970) in PSR B1237+25, is a broad-band change in the emission process. Although it has not yet been fully understood, some concepts to interpret this have been put forward (for details, see Lyne et al., 2010).

1.1.4.2 Spin Down Energy Loss Rate and Characteristic Age

Although I previously mentioned that pulsars have extremely stable spin periods, one typical property of pulsars is the gradual increase of the spin period, which is mainly related to the emission of EM waves. If we simply consider the pulsar as a rotating dipole magnet and

expect that the pulsar is undergoing a steady loss of rotational kinetic energy which slows the pulsar down slowly over time, the spin−down loss rate of rotational kinetic energy, which is known as "spin-down luminosity", can be defined as,

$$\dot{E}_{\rm rot} = -\frac{{\rm d}(I\Omega^2/2)}{{\rm d}t} = -I\Omega\dot{\Omega} = 4\pi^2 I\dot{P}P^{-3}, \tag{1.1}$$

where $I = kM_pR^2$ is the moment of inertia, with typically $k \simeq 0.4$ is the inertia constant, and $M_p = 1.4\,M_\odot$ and $R = 10$ km are the mass and the radius of the pulsar respectively. $\Omega = 2\pi/P$ is the rotational angular velocity, with P the spin period of the pulsar and $\dot{P}$ is the first spin period derivative.

In accordance with classical electrodynamics (Jackson, 1962), if we assume that the loss of rotational energy is only due to magnetic dipole radiation, a rotating dipole magnet with dipole magnetic moment $|\mathbf{m}|$ will emit EM waves at its rotation frequency, and the emitted radiation power $\dot{E}_{\rm dipole}$ can be defined as,

$$\dot{E}_{\rm dipole} = \frac{2}{3c^3}|\mathbf{m}|^2\Omega^4\sin^2\alpha, \tag{1.2}$$

where α is the magnetic inclination angle, the angle between the magnetic moment and rotational axis and c is the speed of light. We can then combine Equations 1.1 and 1.2 to obtain the evolution of the rotational angular velocity $\dot{\Omega}$ given by,

$$\dot{\Omega} = -\frac{2|\mathbf{m}|^2\sin^2\alpha}{3Ic^3}\Omega^3. \tag{1.3}$$

However, magnetic dipole radiation is not the only contribution to the loss of kinetic energy in reality, as shown by the fact that the index of the power-law dependency between Ω and $\dot{\Omega}$ is usually not 3 (e.g. Kaspi & Helfand, 2002). Kramer et al. (2006a) demonstrated that angular momentum can be lost through relativistic winds of outflowing particles as well. For this reason, the rotational frequency is usually expressed in a more general way in accordance with the pulsar rotational frequency $\nu = 1/P$,

$$\dot{\nu} = -K\nu^n, \tag{1.4}$$

where K is a constant while n is known as the braking index. The pure magnetic dipole radiation model generally predicts $n = 3$. By further taking the time derivative of Equation

1.4 and eliminating the constant K, we can derive the value of the braking index as,

$$n = \frac{\nu\ddot{\nu}}{\dot{\nu}^2}, \tag{1.5}$$

where $\ddot{\nu}$ is the second derivative of the spin frequency. Theoretically, based on Equation 1.5, we can obtain the braking index by measuring the pulsar's spin frequency as well as its first and second derivatives. However, this approach is always hard to realize since it is dominated by timing noise. Only for the youngest pulsars, especially with large $\ddot{\nu}$, can we measure the braking index on a human timescale. So far, only 10 pulsars of the more than 2800 known pulsars have measured braking indices (Kim & An, 2019), with braking index values typically ranging from 0.9 ± 0.2 (Espinoza et al., 2011; Lyne et al., 2015) to 3.15 ± 0.03 (Archibald et al., 2016).

One of the most important applications of spin-down and the braking index is to measure pulsars' characteristic age, τ_c. Except for very few exceptions that we can observe its supernova event, it is nearly impossible to directly observe a pulsar's age.

Equation 1.4 can be expressed in terms of P and $\dot{P}$ as:

$$\dot{P} = KP^{2-n}. \tag{1.6}$$

To calculate τ_c, I firstly take K as a constant and assuming $n \neq 1$, then we can integrate Equation 1.5 to derived the characteristic age of a pulsar as

$$\tau_c = \int_{P_0}^{P} P^{n-2} dP = \frac{P}{(n-1)\dot{P}} \left[1 - \left(\frac{P_0}{P} \right)^{n-1} \right], \tag{1.7}$$

where P_0 is the pulsar's initial spin period. Assuming that magnetic dipole radiation is the only cause of kinetic energy loss and that the spin-down is sufficient, thus $(\frac{P_0}{P})^2 \lll 1$, the characteristic age can be derived,

$$\tau_c = \frac{P}{2\dot{P}} \simeq 15.8\text{Myr} \left(\frac{P}{\text{s}} \right) \left(\frac{\dot{P}}{10^{-15}} \right)^{-1}, \tag{1.8}$$

which is only determined by P and $\dot{P}$. But the thing that has to be noticed is, as I mentioned above in the aforementioned assumptions, it is just a rough estimate of a pulsar's real age, in particular, it doesn't work well for very young pulsars and MSPs.

1.1.4.3 Characteristic Surface Magnetic Field Strength

Another important application of spin-down and the braking index is to measure pulsars' characteristic surface magnetic field strength. Since it is also impossible to measure the magnetic field strength directly, we can merely estimate it by assuming that the spin-down process is purely due to dipole braking. Lorimer & Kramer (2005) have shown that the characteristic magnitude of the magnetic field at the surface of the pulsar with distance r, from the magnetic moment as associated with the field strength by $B \approx |\mathbf{m}|/r^3$, can be derived as

$$B_s = \sqrt{\frac{3c^3}{8\pi^2}\frac{I}{R^6 \sin^2\alpha} P\dot{P}}, \tag{1.9}$$

where α is the angle between the dipole moment and the rotation axis. For typical pulsars, assuming $\alpha = 90$, $R = 10$ km, $I = 10^{45}$ g cm^2, the characteristic magnetic field can be obtained with P and $\dot{P}$ in the expression of:

$$B_s = 3.2 \times 10^{19} G \sqrt{P\dot{P}}. \tag{1.10}$$

1.1.4.4 Flux Density

Pulsars are very weak celestial sources. Assuming a pulsar's radiation passing through a surface dσ in time dt at the frequency of f within the solid angle dω on a ray which points an angle θ away from the surface (Figure 1.4), we can then define the energy received as follows:

$$\mathrm{d}E_f = I_f \cos\theta \mathrm{d}\sigma \mathrm{d}f \mathrm{d}\omega \mathrm{d}t, \tag{1.11}$$

where I_f is the specific intensity[3] of radiation at the frequency f in the direction of the solid angle. Then, we can derive the power, dP, received by the receiver as:

$$\mathrm{d}P = \frac{dE_f}{\mathrm{d}t} = I_f \cos\theta \mathrm{d}\sigma \mathrm{d}f \mathrm{d}\omega. \tag{1.12}$$

Thus the quantitative definition of specific intensity will be:

$$I_f = \frac{\mathrm{d}P}{\cos\theta \mathrm{d}\sigma \mathrm{d}f \mathrm{d}\omega}. \tag{1.13}$$

[3] also known as spectral intensity, spectral brightness or brightness

The total intensity I can be obtained by integrating over all frequencies, described in the following form:

$$I = \int_0^\infty I_f \mathrm{d}f. \tag{1.14}$$

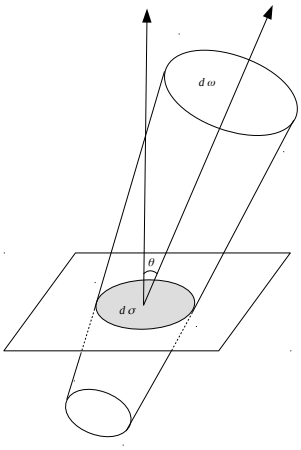

Figure 1.4 A sketch of the definition of flux density. Figure Credit: Palmer & Davenhall (2001).

If a source is discrete, the spectral flux density[4], S_f, can be defined as:

$$S_f = \int_{source} I_f \mathrm{d}\Omega. \tag{1.15}$$

For most pulsars, their flux density at a frequency of 1 GHz is typically < 10 mJy[5] (Lorimer & Kramer, 2005). Flux density measurements are essential for further analysis of pulsar emission properties and the influences in the transmission process. Furthermore, we can also have a prediction of the NS birth rate and their distribution in the Galactic disk if we take into consideration pulsar beaming models and telescope sensitivity. Pulsars are typically steep-spectrum sources and their flux density spectra can be represented by a power law:

$$S_f \propto f^\alpha, \tag{1.16}$$

[4]Notice that various authors define flux and flux density differently. Here I consider flux as the power received per unit area while flux density is the power received per unit area per unit frequency parallel to the line of sight (LOS). In other words, flux is the integral of flux density with respect to frequency.

[5]$1\ \mathrm{Jy} = 10^{-26}\ \mathrm{W\,m^{-2}\,Hz^{-1}}$

with α the spectral index. The flux density spectrum is observed to be diverse, with α spread from 0 to -4, with the average spectral index α estimated by Bates et al. (2013) to be -1.41 ± 0.06. For the majority of known pulsars, a single power-law can represent the mean flux density distribution very well. However, there are a minority of pulsars that need two components or even more complex power-law slopes at low and high-frequency ranges. The low-frequency 'turn-over' and high-frequency 'cut-off' was first reported by Sieber (1973). The spectral turn-over, which usually occurs at around 100 MHz (Lorimer et al., 1995a), turns the power-law slope to become positive. However, there are also a small group of pulsars that show turn-over at high frequencies and are referred to as the gigahertz peaked spectrum pulsars (Blake, 1970). A detailed analysis of spectral turn-overs in 194 pulsars at low frequencies can be found in Bilous et al. (2016).

1.2 Effects of the Ionized Interstellar Medium

The radiation emitted from a pulsar's magnetic pole has to pass through the IISM before being observed by our telescopes. The IISM, which mainly consists of cold, ionized plasma, fills interstellar space. The interaction between pulsar radiation and the IISM can be regarded as two properties: homogenous by considering the IISM with an average electron density (e.g., dispersion and Faraday rotation) and inhomogeneous by considering the IISM with fluctuating electron density (e.g., scattering and scintillation). All these effects could introduce perturbations when we are timing the pulsars and thus will decrease the timing precision. A comprehensive and in-depth understanding of the IISM and these distinct propagation effects will speed up the detection of nano-Hertz GWs.

1.2.1 Dispersion

In the idealized vacuum environment, the EM signal would propagate unencumbered, which means that the signal will travel at the same speed of light c regardless of its frequency. However, interstellar space is not an absolute vacuum, instead, it consists of ionized plasma and neutral gas. When pulsar emission travels through the IISM, its group velocity (v_g) would be reduced by a frequency-dependent factor (Lorimer & Kramer, 2005), which is called the refractive index, μ:

$$v_g = c\mu = c\sqrt{1-(\frac{f_p}{f})^2}, \tag{1.17}$$

where f is the observing frequency and f_p is the plasma frequency, which is defined as:

$$f_p = \sqrt{\frac{e^2 n_e}{\pi m_e}} \approx 8.97\,\mathrm{kHz}\sqrt{\frac{n_e}{\mathrm{cm}^{-3}}}, \tag{1.18}$$

where n_e is the electron density along the LOS, e and m_e are the charge and the mass of the electron respectively.

As shown in Figure 1.5, signals at higher frequencies arrive earlier than at lower frequencies. For broadband emission between a lower frequency f_l and higher frequency f_h (both in MHz), the time delay across this bandwidth then becomes:

$$\begin{aligned} \Delta t &= \frac{e^2}{2\pi m_e c} \times (f_l^{-2} - f_h^{-2}) \times \mathrm{DM} \\ &= 4.15 \times 10^{-6}\ \mathrm{ms} \times (f_l^{-2} - f_h^{-2}) \times \mathrm{DM}, \end{aligned} \tag{1.19}$$

where DM is the dispersion measure of the pulsar, defined as the electron column density along the LOS over a distance l:

$$\mathrm{DM} = \int_0^l n_e \,\mathrm{d}s\ \mathrm{cm}^{-3}\ \mathrm{pc}. \tag{1.20}$$

One practical use of DM is to estimate the distance to the pulsar. Through observing the dispersive delay with a broadband receiver, the corresponding DM can be measured using Equation 1.19. Once the DM is acquired for a pulsar, it is possible to estimate the distance between the pulsar and the Earth by integrating Equation 1.20 with a Galactic electron number density model, such as the "NE2001" model (Cordes & Lazio, 2002) or more recently the "YMW16" model (based on pulsar distance and DM measurements, Yao et al., 2017). These models perform very well in terms of modeling the large-scale structure of the Galactic electron distribution (Schnitzeler, 2012), but may easily fail with small-scale structures due to the lack of enough measurements to accurately constrain them.

1.2.2 Faraday Rotation

Within a magnetic field, free electrons are forced to move circularly due to the Lorentz force. When EM wave goes through a magnetic field, the magnetic field will produce a rotation

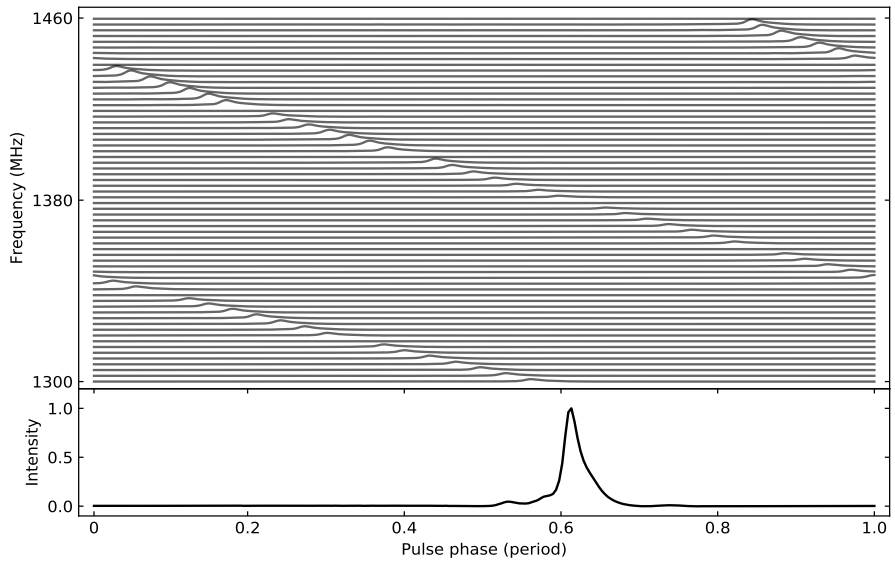

Figure 1.5 Uncorrected dispersive delays for a pulsar observation over a bandwidth of 160 MHz (64 channels of 2.5 MHz width each), centered at 1380 MHz. The delays wrap since the data are folded (i.e. averaged) modulo the pulse period.

of the plane of polarization (Faraday, 1844). This rotation, known as Faraday rotation, is proportional to the component of the magnetic field in the direction of light propagation.

The IISM is weakly magnetized. As EM radiation emitted from a pulsar passes through the IISM, with the component of the interstellar magnetic field in the direction of propagation, $B_{\|}$, the cyclotron frequency (f_B) associated with the ionized IISM is:

$$f_B = \frac{eB_{\|}}{2\pi m_e c}. \tag{1.21}$$

Since $B_{\|}$ typically equals a micro-Gauss, f_B is usually a few Hz. The electrons in the right and left hand circularly polarized waves thereby oscillate with frequencies $f + f_B$ and $f - f_B$, respectively. After propagation through the plasma over a distance l, the Faraday rotation effect will rotate the linear polarization position angle Ψ by

$$\Psi = \int_0^l k \mathrm{ds}, \tag{1.22}$$

with $k = 2\pi/\lambda$ the wave number and λ the wavelength of the signal. For a cold magnetized plasma with cyclotron frequency f_B and plasma frequency f_p, since $f \gg f_p$ and $f \gg f_B$, we can then express k with the refractive index, μ, introduced in Equation 1.17, as

$$k(f) = \frac{2\pi}{c} f\mu = \frac{2\pi f}{c}\sqrt{1 - \frac{f_p^2}{f^2} \mp \frac{f_p^2 f_B}{f^3}}, \tag{1.23}$$

where the "-" and "+" signs are for left-hand and right-hand circularly polarized waves respectively. Since a linear polarization can be regarded as a superposition of left-hand k_L and right-hand k_R circularly polarized wave components of equal amplitude, the net angular shift can be expressed as,

$$\begin{aligned} \Delta\Psi &= \frac{1}{2}\int_0^l (k_R - k_L)\mathrm{ds} = \frac{e^3}{2\pi m_e^2 c^2 f^2}\int_0^1 n_e B_\parallel \mathrm{ds} \\ &\equiv \lambda^2 \mathrm{RM}, \end{aligned} \tag{1.24}$$

where

$$\mathrm{RM} = \frac{e^3}{2\pi m_e^2 c^4}\int_0^1 n_e B_\parallel ds, \tag{1.25}$$

is the rotation measure, n_e is the density of electrons at each point along the path, $B_\parallel$ is the component of the interstellar magnetic field in the direction of propagation at each point along the path while e and m_e are the electron charge and mass respectively.

As we can see from Equation 1.25, RM is a constant value for a given pulsar and thus $\Delta\Psi$ varies with frequency. Once we measured the angle shift at different frequencies, it is possible to estimate the magnetic field $B_\parallel$ of the galaxy by

$$B_\parallel = \frac{\int_0^l n_e B_\parallel \mathrm{ds}}{\int_0^l n_e \mathrm{ds}} = 1.23\mu G\left(\frac{\mathrm{RM}}{\mathrm{rad\ m^{-2}}}\right)\left(\frac{\mathrm{DM}}{\mathrm{cm^{-3}pc}}\right). \tag{1.26}$$

However, because magnetic fields can experience direction reversals within the intervening medium, this method only gives us an upper limit on the interstellar magnetic field strength in the LOS direction.

1.2.3 Scattering

Even though I assumed that the IISM was a homogeneous and stationary medium and has a uniform average magnetic field strength, the fact is that the electron density often shows irregularities and turbulence (Armstrong et al., 1995), in other words, the IISM is neither uniform nor isotropic. When pulsar signals traverse through the turbulent IISM, the signal will get scattered, which will lead to multipath propagation effects. While the majority of the signal propagates along a straight line, still scattered and delayed signals can be received. The radiation that arrives later causes a strongly frequency-dependent effect on the pulse profile shape, producing an exponential tail (referred to as a scattering tail) characterized by a scattering timescale τ_{sc}.

Although the structure and dynamics of the IISM fluctuations are not fully understood, the effects of the IISM have been described by several scattering screen models: 1) a thin screen; 2) a thick screen; 3) multiple screens. Among the three models, the thin screen model (as shown in Figure 1.6), put forward by Scheuer (1968) is the simplest but provides us a useful first-order approximation of the scattering effect. In the thin screen model, the scattering medium is modeled as a thin screen at one single location along the LOS between the pulsar and the Earth.

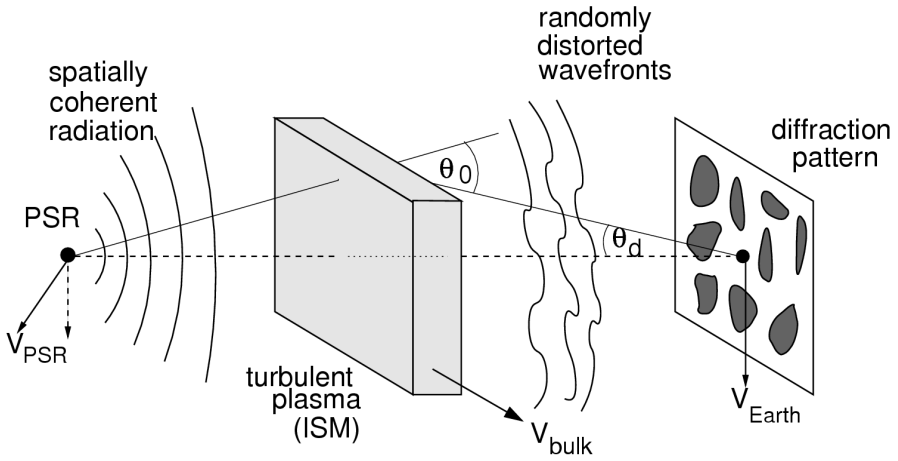

Figure 1.6 A sketch of the thin screen model. Small-angle deviations are caused by inhomogeneities in the IISM. Figure credit: Lorimer & Kramer (2005)

The scattering time delay τ_{sc} is given by

$$\tau_{sc} = \frac{\theta_0^2 l(l-a)}{2ac}, \tag{1.27}$$

where l is the distance to the pulsar, a is the distance between the pulsar and the scattering screen and c is the speed of light while θ_0 is the root mean square scattering angle.

For simplicity, if we model a Gaussian distribution of the IISM inhomogeneities (Lee & Jokipii, 1975; Salmona, 1967), the scattering time scale τ_{sc} can be described with

$$\tau_{sc} \propto l^2 f^{-4}. \tag{1.28}$$

However, some other research (e.g. Lee & Jokipii, 1976; Rickett, 1977) suggests that the turbulence of the IISM is more likely to follow the Kolmogorov spectrum, and thus leads to $\tau_{sc} \propto f^{-4.4}$.

Due to the frequency-dependent scatter-broadening effect shown above, sharp pulse profiles will be smeared into an exponential function at the observing site. A distinct pulse profile could therefore become completely submerged into the noise.

1.2.4 Scintillation

Another effect that is caused by the inhomogeneous IISM is scintillation, which is very similar to the twinkling star phenomenon caused by turbulence in the Earth's atmosphere. Scintillation can produce pulse intensity variations as a function of time and frequency due to the interference effects of the IISM.

Since the phase differences caused by passage through interstellar inhomogeneities are frequency-dependent and the phase difference defines whether interacting waves will constructively or destructively interfere, pulsars will exhibit constructive interference (i.e. bright patches usually referred to as "scintles") with a characteristic bandwidth Δf, which relates to the scattering time delay $\tau_{\rm sc}$ as follows (Lorimer & Kramer, 2005):

$$2\pi\Delta f \tau_{sc} \sim 1, \tag{1.29}$$

which indicates that the scintillation bandwidth $\Delta f \propto 1/\tau_{sc} \propto f^4$. Since scintillation could produce intensity variations in both the frequency and time domain, these scintles can be measured in a two-dimensional plot of pulse intensity as a function of time and frequency, a so-called dynamic spectrum.

1.3 Pulsar Applications and Gravitational Wave Astronomy

As one of the most important predictions of GR, GWs, originating from accelerated masses, are ripples in the curvature of space-time and propagate with the speed of light. The GW stretches and squeezes the actual fabric of space simultaneously in the orthogonal directions. Although Einstein (1916) predicted the existence of GWs, he thought GWs are too weak to be detectable with the technology at that time. However, things changed on 11 February 2016 when the LIGO collaboration declared the first detection of GWs (Abbott et al., 2016). This detection raised the curtain of GW Astronomy. For many centuries, astronomers have only been able to work with visible light. After Maxwell (1865) described the existence of EM waves, astronomers started to observe the universe with other frequency bands, from radio waves to ultraviolet waves, X-rays, and γ-rays. The use of each frequency band of EM waves has broadened our horizon of the universe and led to plenty of new findings. In the same way, GWs have the potential to show us new features of cosmic objects, or rather, new cosmic objects that are largely invisible in EM waves.

1.3.1 Gravitational Waves

It was in 1916 that Albert Einstein published his landmark work, the theory of GR, which reshaped modern physics. The GR theory refined Isaac Newtown's classical physics of gravitation and introduced a more generally applicable concept. Instead of taking space and time as two absolute and independent concepts (as in Newton's classical physics), Einstein linked these two concepts together with the field equations:

$$G_{\mu\nu} \equiv R_{\mu\nu} - \frac{1}{2} g_{\mu\nu} R = \frac{8\pi G}{c^4} T_{\mu\nu}, \tag{1.30}$$

where $G_{\mu\nu}$ is the Einstein tensor, $R_{\mu\nu}$ is the Ricci curvature tensor, $g_{\mu\nu}$ is the metric tensor that determines the space-time interval between two points, R is the Ricci scalar curvature, G is Newton's universal gravitational constant, c is the speed of light in vacuum, and $T_{\mu\nu}$ is the stress-energy-momentum tensor. According to this equation, space and time are interwoven and form a geometric property called space-time. Mass and energy cause space-time to curve.

Based on this concept, several predictions were made, such as the BH, gravitational lensing, and gravitational time dilation. Many of them had been proven over time. Among them, GWs are a key prediction of GR since they are directly related to the evolution and death of massive stars. Objects that possess mass would warp space-time, and the effect a

warp has on other objects is what we observe as gravity. That means space-time is curved around every object that has mass. When a massive object speeds up, it would disrupt space-time and hence generate GWs propagating outward.

GWs are extremely weak signals and even the strongest waves radiated by the most violent and catastrophic events, like supermassive BHs colliding or supernovae, the GW signals arriving on the Earth are so weak to be detected. So for a long time, it was thought that the GWs were undetectable by us. GWs do cause space-time warping and thus lead to the EM signals arriving earlier or later. Detection of this tiny wiggle could prove the passage of GWs.

One primary goal of detecting continuous GWs is to observe NSs in a completely new way as we are observing pulsars now. It is predicted that there will be millions of NSs in the Milky Way Galaxy, but only less than 3000 of them have been detected by us. GWs perhaps could provide us a new method of observing the large amount of "nonluminous stars" and have a deeper understanding of their internal structure, composition, and evolutionary mechanism.

1.3.2 Gravitational Wave Sources

In theory, masses that accelerate produce GWs. So, everywhere in the Universe, even the Earth is filled with GWs. But the GWs produced by a planet and the masses and accelerations available to us are too weak to be detected with our instruments. Luckily, the Universe is filled with extremely massive objects that undergo rapid accelerations and the GWs produced by them could be detected by us. Examples of such things are interacting BHs, or massive stars blowing up, such as supernovae. Observing GW signals and modeling them will significantly expand our view of the Universe. In Figure 1.7, I present several typical GW sources and strain sensitivity as a function of frequency for several GW detectors. In this subsection, I will turn our attention to sources of gravitational radiation.

Continuous GWs: Continuous GWs refer to long-lasting and nearly monochromatic waves that are thought to be produced by orbiting binary systems of NSs or BHs (long before merger), Other systems, such as rotating deformed (non-axisymmetric) NSs could also produce continuous GWs (Bildsten, 1998). However, in order to be continuous, the orbital separation of a binary system has to be relatively large, which means that the signals would be too weak to detect. The study of continuous GWs would yield knowledge on coalescing binaries at early stages or NS structure.

Inspiral GWs: Inspiral GWs are generated by orbiting pairs of massive and dense objects like NSs or BHs. Two massive objects in a binary system are mutually locked by gravity and will draw each other closer and closer in a runaway accelerating in a spiraling

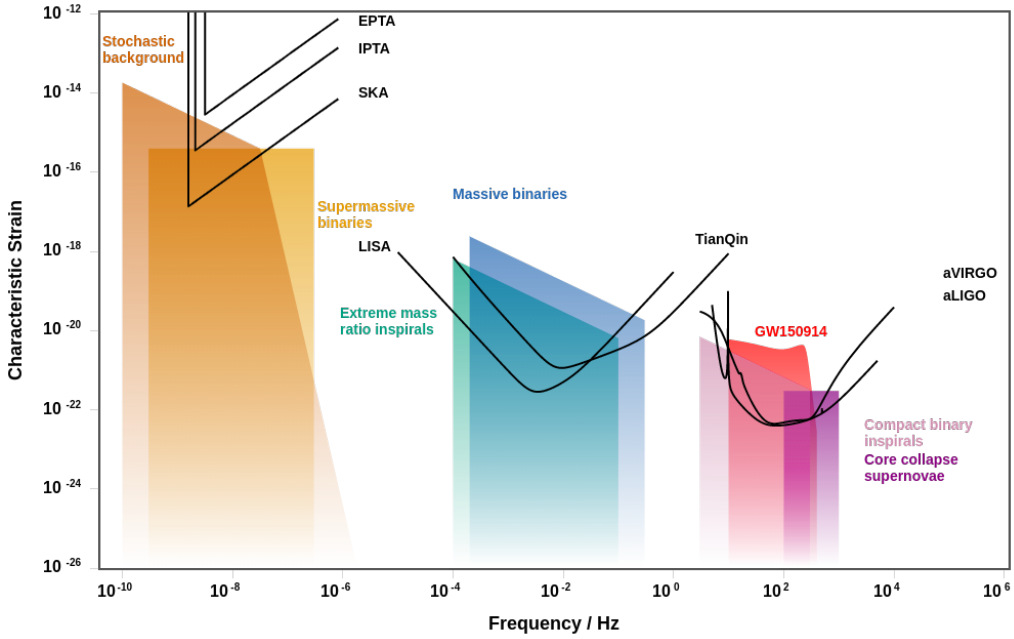

Figure 1.7 GW sources and strain sensitivity as a function of frequency for GW detection with PTAs, LISA, TIANQIN, aVIRGO and aLIGO.
Credit: (Moore et al., 2015).

embrace. During the inspiral process, their orbital separation decreases while their speed increases. This process is similar to the continuous GWs, except that the GW frequency changes with time. Inspiraling binary systems can emit copious amounts of gravitational radiation, and at the end of their life, the binary companions would merge. Coalescence of compact binary systems could generate huge GWs, with the wave frequency increasing with the orbital frequency until the two masses collide and merge into one dense body. The largest amplitude of GWs occurs at the merger phase.

Burst GWs: Among the most violent events known to astronomy, the merging phase of coalescing binary dense stars (Finn & Lommen, 2010) and supernovae are sources to create burst GWs, a kind of GW that comes from short-duration (lasting a few milliseconds) violent events. When the core of an asymmetric massive star collapses, hydrodynamical oscillation of the protoneutron star core would emit strong GWs (Ott et al., 2006). Although supernovae outside the Galaxy are less likely detectable due to a small fraction of the mass transformed into gravitational radiation and the long distance, the rate of core-collapse supernovae within the Galaxy is promising.

Stochastic GWs: Stochastic GWs (also GWB) are small, random gravitational-wave signals that spread all over the Universe all the time and are mixed. These waves are thought to arise from a superposition of incoherent sources and are thus random both in amplitude and directions. The most likely detected GWB would be from SMBHBs (Begelman et al., 1980). This GWB will teach us about Galaxy evolution since these SMBHBs are supposed to form as a consequence of galaxy mergers, i.e., it will help us to constrain the merging history of galaxies in the Universe. In addition, primordial GWs originating from the Big Bang are another potential source. Detection of these relic GWs (Boyle & Buonanno, 2008; Grishchuk, 2005) from the Big Bang will allow us to understand the early Universe. Besides, another possible source is from "cosmic strings" (Caldwell et al., 1996; Damour & Vilenkin, 2005), which are hypothesized to be one-dimensional topological defects. However, a detection of a GWB from cosmic strings would have a profound impact on cosmology.

1.3.3 Pulsars as Gravitational Wave Detectors

To detect GWs directly is one of the most challenging feats of astronomy and astrophysics in the 21st century. Depending on the GW frequency, several kinds of GW detectors have been set up, both ground-based and space-based. However, the principles are almost identical: GWs cause tiny variations in the distance between point masses and we can detect GWs by measuring the light travel time between these points, called the 'arms' of the detector.

Some of the detectors adopted an interferometric method to detect the deviations of the light travel time of laser arms, like the ground-based detector, the Advanced Laser

Interferometer Gravitational-Wave Observatory (aLIGO, LIGO Collaboration et al., 2015), and the space-based detector the Evolved Laser Interferometer Space Antenna (eLISA). The ground-based detectors, which are limited by the length of their arms, are designed to detect the high-frequency ($\sim$ Hz level) GWs. There are several built or planned ground-based detectors that aim to search for high-frequency GWs, such as aLIGO, aVIRGO (Acernese et al., 2015), TAMA (Ando & TAMA Collaboration, 2002), and GEO (Affeldt et al., 2014). And in space, a bunch of GW detectors to detect μHz GWs are on the way, such as the eLISA (Amaro-Seoane et al., 2013), TIANQIN (Luo et al., 2016), the Big Bang Observer (BBO, Harry et al., 2006), and the Deci-Hertz Interferometer GW Observatory (DECIGO, Kawamura et al., 2011).

However, to detect nanohertz GWs, longer arms are needed. Pulsars are excellent candidates, with the "arm" in this case being the path between the Earth and the pulsar. Any fractional change in the length of the arms can be precisely measured through pulsar timing, which allows us to search for tiny perturbations due to GWs.

A promising application of this trait is to use them to detect GWs. As Romani (1989) and Foster & Backer (1990) suggested, an array of MSPs that are distributed uniformly across the sky can be used to detecte low-frequency (with frequencies between 10^{-6} and 10^{-9} Hz) GWs through correlations between the pulsars. As I stated above, GWs are ripples in space-time, and they could therefore cause time variations of pulses' times of arrival (TOAs) and the amplitude of these variations is calculated to be around a few tens to hundreds of nanoseconds.

GWs travel between Earth and pulsars distorting the intervening space-time and thus causing pulses to arrive earlier or later than the modeled TOAs. Besides, the effects of GWs are correlated on all pulsars. We can search for this imprinted correlation to confirm the existence of GWs. This correlation is known as the Hellings-Downs (HD) correlation (Hellings & Downs, 1983). Rather than systematic clock and ephemeris errors that have monopolar and dipolar spatial correlations on the timing residuals, the HD curve (presented in Figure 1.8) reflects the quadrupolar nature of GWs.

Currently, three major PTAs are working on GW detections at nanohertz frequency, namely the European Pulsar Timing Array (EPTA, Desvignes et al., 2016), the North American Nanohertz Observatory for GWs (NANOGrav, Arzoumanian et al., 2016), and the Parkes Pulsar Timing Array (PPTA, Reardon et al., 2016). Together, these three PTAs form an international collaboration, the International PTA (IPTA, Verbiest et al., 2016). The EPTA is a multinational European collaboration, which consists of the Netherlands Institute for Radio Astronomy (ASTRON), the National Institute for Astrophysics/Cagliari Observatory, the Max-Planck Institute for Radio Astronomy, the Paris Observatory/Nançay, the University

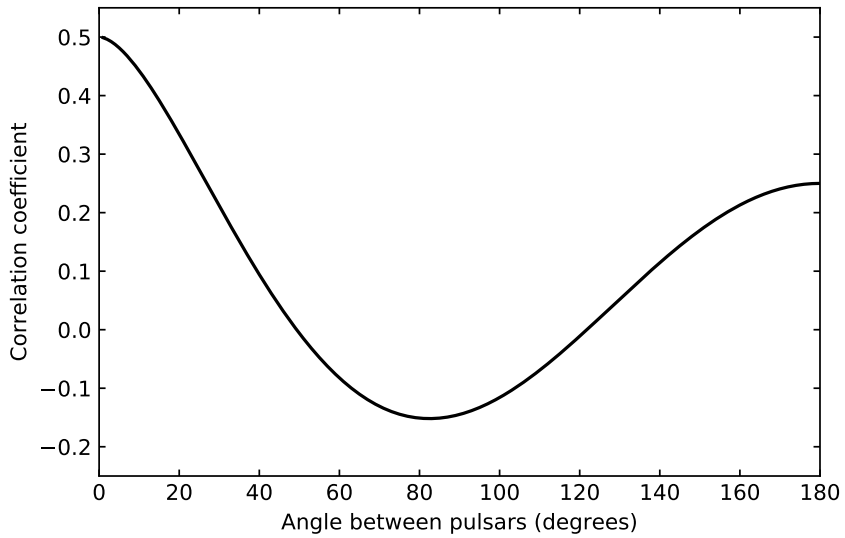

Figure 1.8 The HD curve, which shows the correlation of timing residuals with respect to the angular separation between pairs of pulsars.

of Manchester, the University of Birmingham, the University of Cambridge and Bielefeld University. Five of the largest European radio telescopes are used to observe the MSPs, namely the Effelsberg Radio Telescope (EFF), the Lovell Radio Telescope at the Jodrell Bank Observatory (JBO), the Nançay Radio Telescope (NCY), the Westerbork Synthesis Radio Telescope (WSRT) and the Sardinia Radio Telescope (SRT). The PPTA was built in 2004 as a collaboration between the Commonwealth Scientific and Industrial Research Organization (CSIRO) and Swinburne University of Technology and mainly use the Parkes telescopes while NANOGrav uses the Green Bank and Arecibo radio telescopes.

1.4 Synopsis

This dissertation presents the result of efforts to improve the pulsar timing precision of the EPTA dataset, by optimizing several key aspects of basic pulsar-timing analysis in detail, based on a real and diverse PTA data set which contains all the intricacies and complications full PTA analyses have to deal with. While a full quantitative study of the impact from each optimization choice on the sensitivity to GWs would be computationally prohibitive, I demonstrate the overall sensitivity improvement to GW-like signals which our work provides, by comparing the results from a standard red-noise analysis, applied to the same data set analyzed both according to our standardized and optimized approach and according to the

standard EPTA analysis routine. I furthermore discuss how an optimal, observatory- and pulsar-specific pipeline can be constructed, in an effort to harmonize and uniformize the analysis procedures in a global PTA context like the IPTA. The structure of this thesis is as follows:

In Chapter 2 I begin with a brief introduction to the EPTA dataset obtained with the newest EPTA receivers. An overview of the data reduction methods used in the data pre-processing is then presented, followed by a clarification about why if one wants high precision pulsar timing results for a pulsar array, one must investigate the optimal pre-processing methods on various pulsars. Finally, I identify and describe the pulsar timing issues that investigate and illustrate our motivation and expectation through this research.

In Chapter 3 I investigate and present a comprehensive comparison of TOA creation algorithms, specifically focusing on the creation of timing templates, TOA determination algorithms, and TOA bandwidth.

In Chapter 4 I present a detailed analysis of a large sample of datasets from thirteen EPTA MSPs, I refined the conclusions described in Chapter 3.

In Chapter 5 I analyze the red noise in a selected set of six pulsars, analyzed according to our method and according to the standard EPTA analysis routines. Subsequently I search for a common red noise, such as the GWB, in these two data sets and compare the sensitivity of the two analysis methods to such a signal.

Finally, in Chapter 6 I conclude this dissertation with an overview and discussion of the results presented above and summarize the current status and future perspectives in this field.

Chapter 2

Pulsar Timing Method

As rotating NSs, pulsars are usually detected through radio emissions produced by the lighthouse effect. Their emission beams originate from their magnetic poles and sweep the Earth regularly as a result of misalignment between their magnetic and rotational axes. In most cases, single pulses are either too weak to observe or vary significantly in pulse shape. However, adding many hundreds or even thousands of consecutive pulses 'in-phase' could yield a stable average profile. One primary usage of this stable average profile is to derive pulsar rotational parameters through the pulsar timing technique. Pulsar timing is the technique where we need to precisely measuring TOAs of the radio pulses and comparing them with predicted TOA derived from the timing model, which includes the astrometric, spin, and binary (if applies) parameters of a pulsar. The differences between the observed TOAs and predicted TOAs are known as timing residuals. In this chapter, I describe the process of pulsar timing and introduce the parameters from which timing models are constructed.

2.1 Data Acquisition

Pulsar single pulses are usually very weak, easily submerged in a noisy environment. To obtain the signals and maximize the signal-to-noise ratio (S/N), a kind of state-of-art instrument, radio telescopes, are usually required. A radio telescope requires a very large reflector area to collect enough radio energy and bring it to a focus, an extremely sensitive receiver, an amplifier to boost the signal, and a recorder to digitize and record the signal for real-time or offline analysis. In this section, I introduce the data acquisition system, which is mainly constituted with dish reflector, front-end, and back-end as described below.

2.1.1 Dish Reflector

The radio telescope is the basic instrument for observing and studying radio waves from celestial bodies. It consists of a reflective surface, directional antennas that collect radio waves, high-sensitivity receivers that amplify radio signals, information recording, and a processing system.

The basic principle of a radio telescope is simple. The incident electromagnetic waves are reflected by a precise reflecting surface and reach the common focus in phase. The most visible part of a single-dish radio telescope tends to be the dish reflector. There are many types of it, including parabolic, spherical and cylindrical reflectors etc. The most commonly used is the parabolic dish. Paraboloid reflectors allow us to design/control the point at which the reflected rays are focused and make it easier to achieve in-phase focus. Therefore, many radio telescope dishes are parabolic.

The two main parameters that characterize the performance of radio telescopes are resolution and sensitivity. The former reflects the ability to distinguish two radio point sources close to each other on the celestial sphere. The higher the resolution, the stronger the ability to distinguish two close radio sources. The latter reflects the ability to detect weak radio sources. The higher the sensitivity, the more dim sources that can be detected.

It is convenient to express the sensitivity in terms of the system equivalent flux density (SEFD; units of Jy), which is defined as (Lyubarsky & Kirk, 2001),

$$\mathrm{SEFD} = \frac{2kT_{\mathrm{sys}}}{A_{\mathrm{e}}}, \tag{2.1}$$

where k is Boltzmann's constant, T_{sys} the system temperature, A_{e} is the effective area of the telescope.

More generally, We can also defined the ideal radiometer equation to determine the sensitivity in terms of flux density,

$$\sigma_T = \frac{2kT_{\mathrm{sys}}}{A_e\sqrt{\Delta f\, t}} = \frac{\mathrm{SEFD}}{\sqrt{\Delta f\, t}}, \tag{2.2}$$

where Δf is the total bandwidth and t is the integration time.

From Equations 2.1 and 2.2, we know that the increase in sensitivity mainly depends on the effective collection area of the telescope, the effective aperture of the parabolic antenna or synthetic aperture radio telescope, the observation time length, and the noise of the entire system (including the noise of the receiving system).

2.1.2 Front-end

The Front-end of the receiver system is one of the most sensitive and crucial elements in the astronomical data acquisition system. The front-end, also referred to as the receiver, mainly accomplishes two important objectives, amplifying the signal and converting the radio frequency (RF) signals to lower intermediate frequency (IF) signals. An overview of the front-end is shown in figure 2.1. The RF radio signals collected by the large dish are concentrated onto a horn antenna, which is also known as feed-horn, where the RF signal is captured and channelized into the receiver. The role of a feed-horn is to transform the signal from free-space electromagnetic waves to orthogonal (linear or circular) polarizations electric voltages. The induced electric voltages are then fed into a Low-Noise Amplifier (LNA) to amplify the signals and filtered to improve the S/N.

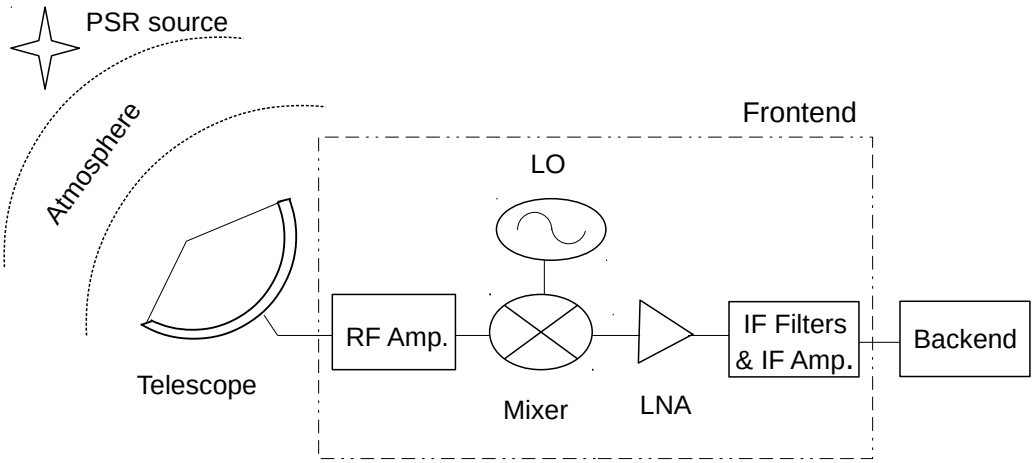

Figure 2.1 Schematic illustration of a front-end.

The LNA plays a vital role in the overall performance of a receiver system. The typical requirement for an LNA in radio astronomy is that the noise temperature, which reflects the level of noise power (for details, please refer to Lorimer & Kramer, 2005), is as low as 50 K and the gain is 20−25 dB (Crossno et al., 2015) . To minimize the potential influence from the electronics thermal noise, the LNA system is traditionally cryogenically cooled to below 20 K. After that, the RF signal will be filtered by a bandpass filter (BPF). Since all stray and source frequencies are pass into the feedhorn, the BPF is specially designed to remove signals from unwanted frequencies. Ideally, the frequency response function of the LNA would be an ideal top-hat function with the desired gain height centered on the observation

frequency, and the unwanted frequencies would be perfectly removed. The range of passable frequency is known as the bandwidth of the receiver. For example, the newly installed UBB receiver at the Effelsberg telescope covers a frequency range from 600−3000 MHz, has a bandwidth of 2.4 GHz (Liu et al., 2014).

From the BPF, the signal is then converted to lower frequencies in the mixer. The mixer blends in the RF signal ν_{RF} with a monochromatic sinusoidal wave ν_{LO} produced by the local oscillator (LO). The RF signal is down-converted using the technique of super-heterodyning (Tiuri, 1964). The output signal consists of the sum and the difference between these two frequencies. But the target signal ν_{IF} at a lower intermediate frequency (IF),

$$\nu_{IF} = \nu_{RF} - \nu_{LO}, \tag{2.3}$$

can be accessed by applying another BPF, which only allows the target signal at the frequency of ν_{IF}, Before sending the IF signal to the back-end, additional amplifiers are usually applied to reach the desired gain.

2.1.3 Back-end

As an essential ingredient of the radio telescope, the back-end system takes the radio signal amplified by the receiver as input. The main function of the back-end is to realize the digitization and basic signal processing of the IF signal and send the processed data to the storage device. The direct current voltage transmitted from the front-end is analog, which can not be directly processed and analyzed by computers. Usually, the signals are converted from analog to digital format via Analog-to-Digital Converters (ADCs) before being passed onto the computers. The sampling rate of the back-end follows the Nyquist-Shannon sampling theorem (Nyquist, 1928; Shannon, 1949).

The back-ends particularly designed for pulsar-related observation, known as pulsar back-ends, are working in various modes. For pulsar searching purposes, the ‘raw’ data is either stored for later processing or analyzed in real-time. In the case of observing known pulsars with timing mode, since the parameters of the pulsar have been already determined, the incoming sub-bands are usually dedispersed and synchronously averaged (folded) over time with the pulsar’s spin period and the spin-down rate. I am only interested in the pulsar timing analysis in this work, so only timing modes are described in this chapter.

2.1.4 De-dispersion and Folding

As I described in Section 1.2, the received pulsar signal is significantly affected when propagation through the IISM, leading to phenomena such as phase shift, amplitude reduction, and pulse profile broadening in the time domain pulse, and thus deteriorates the TOA measurement. Therefore, it is vital to dedisperse the received pulsar signals before measuring TOAs.

De-dispersion intends to eliminate the dispersive effect in the signal frequency band. At present, there are two approaches: incoherent and coherent de-dispersion. Incoherent de-dispersion is based on time series, channelize the signals with filter banks, and eliminate dispersion by shifting each channel according to the delay time relative to the reference channel.

The process of incoherent de-dispersion is to first divide the time domain signal with the observation bandwidth into several narrow channels by the filter bank, and then shift each channel signal in the time domain by an appropriate amount of time delay, and finally align the pulses. The signal amplitudes of all channels are accumulated to obtain the time domain signal sequence after de-dispersion. The advantage of incoherent de-dispersion is that both the data volume and the computation requirements are small. However, the defects are also obvious: the dispersion within each channel is not eliminated, and some phase information would lost in the process.

By comparison, coherent de-dispersion makes use of the transfer function (chirp function) of the interstellar medium in the frequency domain. The dispersive effect of the interstellar medium is equivalent to a function of the phase shifter (Hankins & Rickett, 1975). The phase shifter can be characterized by a transfer function $H(f)$ (Lorimer & Kramer, 2005):

$$H(f_0+f) = \exp\left[\frac{i2\pi Df^2}{f_0^2\,(f_0+f)}\,\mathrm{DM}\right], \tag{2.4}$$

where $i=\sqrt{-1}$, f_0 is the central frequency, $D=4.15\times10^3\ \mathrm{MHz^2\,pc^{-1}\,cm^3\,s}$ is the dispersion measure constant and DM is the dispersion measure defined in Equation 1.20. From the transfer function $H(f)$, it can be seen that the original signal can be completely dedispersed by applying the complex conjugate $H(-f)$ to eliminate the dispersive effect in the Fourier domain.

Among the discovered 2000 pulsars, most of them are too weak to be direct observed within a single pulse. However, since pulsars have an extremely stable rotation period, the S/N can be improved by periodic folding, which synchronously averaging the data at the pulse period (See Section 7.1 of Lorimer & Kramer, 2005, for a detailed step to fold) . The

yield averaged pulse profile represents the average emission from the pulsars as a function of its rotational phase. We know that noise and signal have different properties. The addition of two signals with the same intensity will increase the signal by a factor of 2, while the sum of two noises of comparable levels only increases its intensity by about 1.4 times. Folding the signals in cycles and adding them together can increase the intensity of S/N.

2.2 Data Pre-Processing

The first step I take with the origin data is to combine sub-integrations and sub-bands data to obtain integrated data with a stable average profile and high S/N. For each observation, I adding the sub-integrations and sub-bands, after aligning them using a timing ephemeris to predict the pulse phases. Next, polarization calibration, as well as flux calibration, are performed if possible. Meanwhile, the RFI excision process is applied to the data. The details in calibration and RFI excision steps are described below.

2.2.1 Polarization Calibration

Generally, Pulsars are highly polarized sources. Pulsar emissions are usually strongly linearly polarized, sometimes with a small amount of circular polarization (Han et al., 1998). In addition, there are also a small number of pulsars, such as PSR B1702−19, that have strong circular polarization characteristics (Gould & Lyne, 1998). Through the polarization measurement of the pulsar, we can obtain the pulsar radiation details and the influence of the interstellar medium during its propagation. However, during pulsar observation, the pulsar signal is usually affected by many factors, such as the Faraday rotation effect of IISM and instrument measurement errors, which will change the polarization characteristics of the transmitted signal. The uncalibrated observation signal will cause variation in the intensity and phase of the pulsar's pulse profile, leading to the generation of incorrect TOA, and then the generation of incorrect fitting parameters. Therefore, it is particularly important to perform polarization calibration before generating TOA.

The polarized direction and components vary systematically with the pulse phase. They can be quantified by four Stokes parameters. The Stokes vector (I, Q, U, V) is a linear combination of the power measured in orthogonal polarization, where I represents the total power of the incident radiation, which can be obtained by sampling two orthogonal polarizations, Q and U are used to describe linear polarization, and V represents circular polarization. By using these four Stokes parameters, we can completely describe the specific characteristics of polarized waves.

In order to calibrate the polarization, we usually express the influence of the instrument as a Mueller matrix, **M**, which acts as the transfer function between the measured Stokes vector S_{measured} of the pulsar and the real Stokes parameter S_{true} by:

$$S_{\text{measure}} = \mathbf{M} \times S_{\text{true}}. \tag{2.5}$$

Through calibrating the observation instruments, **M**, can be determined, and thus we can obtain S_{true}. The most common practice to calibrate polarization caused by the observation system is making use of artificial signals also referred to as noise diodes, which are usually observed with the same instrumental set-up just before or after each pulsar observation. Ideally, the noise diode provides a purely linearly polarized reference source contains both on and off states, usually a square wave with a 50% duty cycle. The Mueller matrix can then measured by tracking the gain and parallactic angles. Besides that, van Straten (2013) put forward a measurement equation method, which uses observations of pulsars with well-known polarization properties as reference observations to determine the Mueller matrix for a telescope and thus, the polarimetric response of that system.

2.2.2 Radio Frequency Interference Excision

In radio astronomy, RFI refers to radio signals generated due to human production activities and life, which is consists of the cellular communication signal, FM radio transmission, global positioning system (GPS) aircraft navigation radar signal, etc. It has a significant impact on the reception of weak astronomical signals, resulting in data loss and reduction of data quality. To reduce RFI, radio telescopes are usually located at radio quiet zone areas that are rarely affected by RFI. However, as the sensitivity of radio astronomy instruments improved significantly in the past decades, accompanied by more diverse sources of RFI, interference from non-astronomical signals has become more and more obvious. Therefore, after completing astronomical observations to obtain data, the most important step is to eliminate RFI first.

Two main approaches of RFI excision techniques are applied in this study. The first step I take with the dataset is to perform automated RFI mitigation using a script, *clean.py* from the COASTGUARD[1] pipeline (Lazarus et al., 2016). This script contains four distinct algorithms to clean corrupted data, but within our process, only the surgical option is adopted. In principle, this algorithm distinguishes RFI from four metrics computed for each sub-integration/channel pair, namely the standard deviation, the mean, the range, and the maximum amplitude of the Fourier transform of the mean-subtracted residual. Frequency

[1]https://github.com/plazar/coast_guard/

channels and time sub-integrations with two or more metrics are 5σ away from the median will be identified as RFI and thus zero weighted. The archive files are then re-checked with the *psrplot* tool from PSRCHIVE[2] (Hotan et al., 2004a) package, any noticeable remaining RFI is identified by eye and removed by PSRCHIVE/*pazi*. Meanwhile, the PSRCHIVE/*paz* routine is also applied at this step to the sub-band edge.

2.3 Times of Arrival and Residuals

As described at the beginning of this chapter, pulsar timing analysis are mainly based on the determination of observed TOAs, $T_{\rm obs}$. In addition, through measured the difference between $T_{\rm obs}$ and the model predict TOAs $T_{\rm pred}$, we can obtain the timing residuals. In this section, a comprehensive introduction of the $T_{\rm obs}$ determination process and models used to predict $T_{\rm pred}$ are presented.

2.3.1 Time of Arrival Determination

Determination of TOAs with the highest possible precision is one of the primary steps in pulsar timing analysis. These TOAs are defined as the timestamps that each pulse emission arrives at the telescope. The TOA that corresponds to the chosen reference point, also know as the fiducial point of the profile (usually the zeroth phase bin of the pulse), is typically recorded in the Modified Julian Date (MJD) format. TOAs can be created precisely by determining the phase offset between each observed pulse profile and a reference profile using cross-correlation algorithms. The reference profile is known as a template and is usually derived by combining several pulses with high S/N or using an analytic profile produced from fitting a high S/N profile with several Gaussian functions (Foster et al., 1991; Kramer et al., 1994), or a smoothed noise-free templates of a high S/N profile produced with PSRCHIVE/*psrsmooth* (Demorest et al., 2013) script. Each of the observed pulses can be cross-correlated with a template using another PSRCHIVE routine, *pat*, to yield the TOAs. Several algorithms can be used, among them, the Fourier domain with Markov chain Monte Carlo (FDM) and the Fourier phase gradient (PGS, Taylor, 1992) PGS are often adopted.

As stated above, the reason we adopt integrated profiles is based on their morphological stability compared to single pulses which are highly influenced by IISM and intrinsic noise inherited from the pulsars' spin irregularity. Assuming that the intensity of the profile of an individuals pulse, $P(t)$ is a shifted and scaled version of the template, $T(t)$, plus a radiometer

[2]http://psrchive.sourceforge.net/

noise $N(t)$ (for details, see Taylor, 1990):

$$P(t) = a + bT(t-\tau) + N(t), \tag{2.6}$$

which can be expressed either in the time or in the phase domain within one folding period. a is an arbitrary intensity shift while b is the intensity scaling factor. The time or phase offset between the templates and observation profile, τ, defines the topocentric TOA or site-arrival-time (SAT). Several algorithms can calculate the offset between their fiducial points, either in the time domain or frequency domain. If the template matching process is carried out in the time domain, the precision will be limited by the sampling bins. A more common way to determine the TOAs in the frequency domain with the PGS algorithm or the FDM algorithm. The phase shift can be converted back to the time domain by multiplying it with the pulsar period. With those two frequency domain algorithms, the timing precision can be smaller than a tenth of the sampling bin size.

The error in the TOA determination process is approximately the ratio of the pulse width, W, to the S/N, which is defined as the ratio of the power of a signal to the noise fluctuations. Based on the of Equation 2.2 (Dicke, 1946), the TOA uncertainty can be expressed as:

$$\tau_{\mathrm{TOA}} \approx \frac{W}{S/N} \propto \frac{S_{\mathrm{sys}}}{\sqrt{t_{\mathrm{obs}}\Delta f}} \frac{1}{S_{\mathrm{mean}}} \frac{W}{\sqrt{P}}, \tag{2.7}$$

where S_{sys} and S_{mean} is the system equivalent and pulsar's mean flux density, respectively. Here, t_{obs} is the integration time, Δf is the bandwidth and P the spin period of the pulsar.

During this process, a very stable local frequency standard is used to time-stamp the observations. This clock is usually a hydrogen maser clock, which utilizing the intrinsic properties of the hydrogen atom at a frequency of 1420 MHz to provide a sharp and constant oscillating signal. Hydrogen maser clocks are generally well behaved and reliable in a short time scale, but these deviate significantly on longer time scales (months to years). However, these can be corrected to UTC using information obtained via the GPS (for details, please refer to Hobbs et al., 2006).

2.3.2 Timing Model

The pulsar timing model is an extensive theoretical framework to predict the pulse TOAs. To model the rotational behavior of the pulsar correctly, we generally require TOAs to be detected at an inertial point. Thus the TOAs generated by the topocentric telescopes have to transform to a corresponding proper pulse emission time at the pulsar. This transformation must take into account the effects of propagation through the IISM, as well as massive

bodies and companion stars influences both in the solar system and the pulsar side. First, the topocentric TOAs (known as site arrival time, SAT) can be transformed to the Solar System barycentre (SSB), which can be regarded as an inertial system. The TOAs at barycentre, (known as the barycentric arrival time, BAT) can be expressed Taylor (1992) in the form:

$$T_{SSB} = t_{SAT} - t_0 + \Delta_{clk} - D/f^2 + (\Delta R_\odot + \Delta E_\odot - \Delta S_\odot) - (\Delta_R + \Delta_E + \Delta_S + \Delta_A), \quad (2.8)$$

where t_0 is a reference TOA; Δ_{clk} represent the offset between the telescope clock and the terrestrial time standard; since observations are usually carried out at large bandwidth, a dispersion delay D/f^2 due to pulse propagation through IISM at frequency f is also included in the timing model; $\Delta R_\odot$, $\Delta E_\odot$, $\Delta S_\odot$ terms are the R*ö*mer, Einstein, and Shapiro delay, respectively, which are used to describe the corrections within the solar system of converting topocentric TOAs to barycentric TOAs; Δ_R, Δ_E and Δ_S are similar terms corresponding to binary pulsar's orbital motion; the last term, Δ_A is the aberration effects in the pulsar orbit.

2.3.2.1 Barycentering Terms

The TOAs measured in the Earth frame are topocentric and are easily affected by the tiny irregularity of spin and orbital due to the elliptical motion of the Earth and the influence of other planets in the Solar system. In this case, we selected the inertial point, the Solar System barycentre, as a reference point and modeled all the factors to correct the time error between BAT and SAT. The transformation from SAT to BAT requires precise knowledge of the location of the Solar System Barycentre, predicted using a Solar System Ephemerides.

Initially, the TOAs measured with the hydrogen maser clock at the observatory are constantly compared to the GPS based Coordinated Universal Time (UTC), a time standard that is measured by the US National Institute of Standard and Technology (NIST). UTC is determined based on the International Atomic Time (TAI), a weighted average of the time kept by more than 400 atomic clocks in over 50 national laboratories around the world. The difference between UTC and TAI is an algebraic sum of leap seconds:

$$\mathrm{UTC} = \mathrm{TAI} + 1.000\,\mathrm{s} \times n\,, \quad (2.9)$$

where n is the leap times and is now 37 since 1 January 2017. Once published by the Bureau International des Poids et Mesures (BIPM[3]), TAI itself has never revised again. However, the TAI can be further converted to a smooth running time standard called Terrestrial Time

[3]https://www.bipm.org

(TT) in the format of :

$$\mathrm{TT} = \mathrm{TAI} + 32.184\,\mathrm{s}\,. \tag{2.10}$$

This theoretical time standard is published by BIMP yearly and can be considered as the time of an ideal atomic clock on the Earth's geoid.

Thus TOAs measured in the observatory frame are translated to the TT frame. However, as we stated above, the TOAs measured at the observatory have to be transferred to the SSB format due to the non-inertial movement of the Earth in the Solar system. During the transformation, we have to take the R*ö*mer delay and relativistic effects of Shapiro delay and Einstein delay into consideration. In this section, I will only introduce delays in the Solar system and assuming that the pulsar is solitary. A detailed introduction of those delays in the binary system will be presented in the following section. Ignoring the effects in the binary system, Equation 2.8 can be simplified as:

$$T_{SSB} = t_{SAT} + \Delta_{clk} - D/f^2 + (\Delta R_\odot + \Delta E_\odot - \Delta S_\odot). \tag{2.11}$$

Here, Δ_{clk} terms represent the transformation of the local observatory H-maser clock time to the TT time standard I state above. The D/f^2 terms are the frequency correction and describe the delay introduced by propagation delay caused by interstellar dispersion.

The Römer delay, $\Delta R_\odot$, is the geometric delay that accounts for the differences between the arrival time at the observatory and SSB, which is due to the annual orbital motion of the Earth and its daily spin motion. Since this effect has annual variations in the pulse arrival times, precise positions of the Earth, as well as other masses within the Solar system are required. This precise ephemeris of the Solar system is published by Jet Propulsion Laboratory (JPL) regularly with several models, like JPL DE 405. The Einstein delay, $\Delta E_\odot$, occurs due to the time dilation associated with the orbital acceleration of the Earth, and gravitational red-shift within the Solar system. To calculate these delays, accurate information of masses and positions of all the significant objects in the Solar system are needed. The last term, Shapiro delay, $\Delta S_\odot$, is a relativistic delay caused by the curvature of space-time when light travels through a region with massive bodies in the Solar System. That's to say, the largest delays are coming from the Sun and the Jupiter, with a maximum delay of around 120 μs and 200 ns respectively.

2.3.2.2 Ionized Interstellar Medium Terms

As I mentioned in Section 1.2, the pulsar signals will be affected by a dispersion effect when propagating through the IISM. While we consider dispersion models as arising from a

homogeneous and stationary environment, there are do exist turbulence in the IISM, and this turbulence can cause DM variations. A precise model of the DM variation is extremely crucial for improving the timing precision. Since the IISM effects are frequency-dependent (Keith et al., 2013), a possible method to correct these variations is multi-wavelength observing and timing. A DM model based on this multi-wavelength observation method can be created and added in the ephemeris for correcting this DM variation.

Besides that, another effect called Doppler Shift also has a significant influence on TOAs determination. Doppler shift could be caused by the Earth's orbit motion which can introduce a frequency shift between the frequency observed in the telescope reference frame and the SSB frame. The Doppler Shift effect can be precisely measured and corrected by using an accurate Solar System Ephemeris (SSE).

2.3.2.3 Binary Terms

Section 2.3.2.1 and Section 2.3.2.2 introduce the effects of the IISM and the Solar system, assuming that the pulsar has no companions. The correction terms mentioned above can well describe the TOAs precisely. However, for a pulsar in a binary system, additional parameters need to be taken into consideration. As in Equation 2.8, the last four components described the extra offset in time delays cased by a binary system. These terms, which describe the motion of pulsar as it orbits the common center of mass of the binary system, follow the same concept in the SSB model. Like precise SSE needs to correct BAT delays, the Keplerian parameters are required to correct the delays in the binary system. These parameters are:

P_b, the orbital period of the binary, measured in days;

ω_p, the longitude of periastron, is the angle measured from the ascending node to the periastron in the direction of motion of the pulsar;

e the orbital eccentricity, which between 0 and 1, given a semi-major axis a_p and a semi-minor axis b_p:

$$e = \sqrt{1 - (\frac{b_p}{a_p})^2}. \tag{2.12}$$

T_0, the epoch of periastron passage, a reference epoch when the pulsar passed through periastron and is given as MJD;

$x_p = a_p \sin i/c$, the projected semi-major axis, measured in light-seconds. Here a_p is the semi-major axis of the pulsar orbit along the LOS and i is the angle of orbital inclination.

For simplicity, if relativistic effects can be ignored, the binary motion of the pulsar can be sufficiently described with the above five parameters within a purely Newtonian classical

model. These five parameters can be obtained through the pulsar timing method. However, the inclination angle between the orbital plane and the plane of the sky is unknown, unless the Shapiro delay effect on the TOAs can be measured. A standard practice we normally use is to consider the inclination angle as a random distribution, a 90% confidence interval for i is between 26° and 90°, based on that and Kepler's third law, we can obtain the binary mass function

$$f_{mass} = \frac{4\pi^2}{G}\frac{x_p^3}{P_b^2} = \frac{(M_c \sin i)^3}{(M_p + M_c)^2}, \tag{2.13}$$

where M_p and M_c are the masses of the pulsar and its orbiting companion respectively while G is Newton's gravitational constant. We can put a limit on the pulsar's mass with this function. If the mass of the companion can be measured through other methods, we can then determine the pulsar mass with Shapiro delay.

As I previously mentioned, the formulae described above have ignored the relativistic effects. Even though some of the pulsars can be sufficiently described with Kepler's laws, some of the pulsars in the binary system require an extra series of "post-Keplerian" (PK) parameters:

The rate of relativistic advance of periastron, $\dot{\omega}$, is the rate which the orientation of the orbit rotates through space and is predicted by GR to be:

$$\dot{\omega} = 3(\frac{2\pi}{P_b})^{5/3}(\frac{G(M_p + M_c)}{c^3})^{2/3}\frac{1}{1-e^2}, \tag{2.14}$$

The orbital decay due to GW emission, $\dot{P}_b$. The predicted size of this effect is given in GR by:

$$\dot{P}_b = -\frac{192\pi}{5c^5}(\frac{2\pi G}{p_b})^{5/3}\ \frac{1 + (73/24)e^2 + (37/96)e^4}{(1-e^2)^{7/2}}\frac{M_p M_c}{(M_p + M_c)^{1/3}}. \tag{2.15}$$

However, one thing that needs to be emphasized is that this is only part of the contribution to the orbital period derivative we observed.

The Shapiro delay, first proposed by Shapiro (1964) for test GR in the Solar system, has two components: the amplitude of the effect (also the range), r and the evolution (also the shape), s. These two relativistic parameters are given by

$$r = \frac{GM}{c^3}, \tag{2.16}$$

$$s = \sin i = \frac{cxG^{-1/3}}{M_c}(\frac{2\pi M}{P_b})^{2/3}. \tag{2.17}$$

These two parameters can describe the delay in the pulses to travel through the curved space-time region.

The last parameter, the transverse Doppler and gravitational red-shift parameter, γ, which is also referred as the Einstein delay, is caused by the pulsar orbital acceleration and gravitational shift:

$$\gamma = \frac{G^{2/3}e}{c^2}(\frac{P_b}{2\pi})^{1/3}\frac{M_c(M+M_c)}{M^{4/3}}. \tag{2.18}$$

For a relativistic system, if two GR effects are measured in addition to the Keplerian parameters, we can determine all other parameters easily.

2.3.3 Timing Residuals

Once the TOAs have been determined, several pulsar timing packages can be adopted to calculate and fit the timing residuals, such as TEMPO[4], TEMPO2[5] (Hobbs et al., 2006) and PINT[6]. Among them, TEMPO2 is the widely-used one. All the required ephemeris are included and effects such as propagation are implemented at $\sim$ 1 ns precision. The main goal of all these packages is to compare the observed TOAs against the theoretical values predicted by the timing model, to generate timing residuals with the lowest root mean square (RMS) by minimizing the reduced chi-squared vaules, χ_r^2, such that these two quantities effectively describe the goodness of fit of the model. The quality of the timing model and the fitting results can be described by the χ_r^2 (e.g. Taylor & Weisberg, 1989):

$${\chi_r}^2 = \frac{1}{\mathrm{N_{TOA}} - \mathrm{N_{par}} - 1}\sum_{i=1}^{\mathrm{N_{TOA}}}(\frac{\phi_i(\mathrm{obs}) - \phi_i(\mathrm{pred})}{\sigma_i})^2\,, \tag{2.19}$$

where $\mathrm{N_{TOA}}$ and $\mathrm{N_{par}}$ is the number of TOAs and number of model parameters fitted respectively, $\phi_i(\mathrm{obs})$ and $\phi_i(\mathrm{pred})$ represent the ith TOA of from detected pulse and predicted models separately, and σ_i is the uncertainty of the ith TOA. If the timing model is correct and good enough to predict the TOAs within the uncertainties, we would expect to get $\chi_r^2 = 1$,

[4]http://tempo.sourceforge.net
[5]https://bitbucket.org/psrsoft/tempo2
[6]https://github.com/nanograv/PINT

which also means that the post-fit timing residuals would have a Gaussian distribution with zero means.

However, we commonly obtain $\chi_r^2 > 1$, This case mainly comes from or underestimation of TOA uncertainties or extra non-Gaussian noise that was not modeled or scaled properly. After all the supported terms have been added to the timing model, if the χ_r^2 remains high, this can be sometimes attributed to under-estimated uncertainty. To settle this issue down, two factors can be added into the timing model: EFAC and EQUAD. The EFAC parameter accounts for incorrect scaling of TOA uncertainty and correct it through increasing the uncertainty by some amount: $\sigma^2 = \mathrm{EFAC}^2 \times \sigma_{\mathrm{TOA}}^2$, while EQUAD accounts for unmodeled sources of noise and will add additional uncertainty (in μs) to X (in μs) in quadrature: $\sigma^2 = \mathrm{EQUAD}^2 + \sigma_{\mathrm{TOA}}^2$.

Even after fitting the residuals with an optimal ephemeris, the RMS of the residuals are still very high and the timing precision does not correspond with our expectations. That's to say, there is still extra noise, perhaps red (power spectrum are frequency-dependent) or white (a flat spectrum at all spectral frequencies), that cannot be explained by the timing model. Since the causes of those noises are still under investigation, I will introduce some of the widely recognized noise that could exist in the timing results.

Among the noises, the predominant red noise originates from DM variation. Several factors could cause DM variations. For example, turbulent spatial variations and eclipses in binary systems could create DM variation. Reardon et al. (2016) find evidence for linear trends and sinusoidal, annual variations in the pulsar data obtained with Parkes telescopes. The magnitude of variations in some of the pulsars observed with Parkes surpass the value predicted in the models used (Petroff et al., 2013). The DM variation is only apparent on long time scales, while for short-term timing observation, it can be considered as too small to detect. However, for GW detection with pulsar timing arrays, we usually need high precision timing data at more than ten years scale. The DM variations in this scale are negligible in this period and could only be mitigated through multi-frequency observations. While pulsars are renowned for their capacity of high time stability, they do exhibit intrinsic spin noise that is caused by sustained, random fluctuations of the rotational spin rate of the pulsars. This spin noise could come from changes in internal structure or magnetosphere torque. Moreover, there is also evidence that glitches are also covariant with timing noise model (Lower et al., 2020). Since the spin noise could be highly correlated with the GW stochastic background (Lentati et al., 2016), we need more pulsars to be included in the current PTA regime.

The radiometer noise is the main contribution to the white noise and comes from the radiometer process. According to Equation 2.2, radiometer noise is given by

$$\sigma_{\rm rm} \propto \frac{T_{\rm sys}}{n_p t \Delta f}, \tag{2.20}$$

where $T_{\rm sys}$ is the system noise temperature, n_p is the number of polarisations, t is the integration time and Δf is the observing bandwidth. According to this formula, we can see that the influence of radiometer noise can be mitigated through increasing the integration time and observing with larger and more sensitive telescopes. The second source of white noise is SWIMS (Osłowski et al., 2011), which is also referred to as pulse-phase jitter noise (Cordes, 1993). SWIMS being stochastic noise, affect the pulse shape and thus influence the determination of TOAs and their uncertainties. As radiometer noise can be reduced by wide-band receivers, and observing with large dish telescopes, the SWIMS will play an increasingly visible role in limiting the timing precision. Assuming that the pulse profile is Gaussian shape and the Gaussian probability density function (PDF) for pulse phase jitter is defined as, according to Cordes & Shannon (2010),

$$\sigma_j = 0.28 \mu s (\frac{W_i}{1\ {\rm ms}})(\frac{N}{10^6})^{-1/2}(\frac{f_j}{1/3})(\frac{1+m_I^2}{2})^{1/2}, \tag{2.21}$$

where W_i is the intrinsic pulse width, N is the number of pulses, f_J is the dimensionless jitter parameter and for most pulsars, f_J is from 1/3 to 1/2, m_I is the amplitude modulation index.

2.4 Outliers in Pulsar Timing Array Datasets

Ideally, the probabilistic model of TOA residuals for a well-timed pulsar should follow a Gaussian distribution with zero means. However, in the presence of non-Gaussian noise, the Gaussian model is sensitive to outliers. Outliers in the timing residuals always show significant deviations from zero and therefore lead to incorrect estimation of timing and noise parameters, and procrastinate the detection of nano-Hertz GW.

In the following sections, an outlier rejection scheme is presented for the TOAs derived from Frequency-resolved templates as well as our EPTA dataset. I introduced several criteria in our algorithms and compared this algorithm with other three different methods and criterion threshold. I then compared these algorithms and apply an optimal combination to our dataset.

2.4.1 Outlier Origin

Outlier TOAs are typically produced due to corruption of the pulsar data by the addition of spurious signals or through effects that introduce additional delays, as described below.

2.4.1.1 Radio Frequency Interference

enables the discovery and regular observation of faint pulsars, on the other, it makes radio astronomy much more sensitive to man-made RFI. RFI in radio astronomy observations mainly results from the unwanted electromagnetic signal from wireless electronics, digital and analog terrestrial and satellite communication, radar signals, etc. These signals could very significant with frequency and time during each observation.

As a precision experiment, pulsar timing is naturally susceptible to the effects of these man-made signals. Although plenty of RFI mitigation algorithms, both hardware, and software-based, have been put forward and applied in the pulsar data analysis, inevitably, some low-level RFI is not removed automatically. The presence of the remaining RFI could make the data useless. Since the pulsar signal itself is weak and the current pulsar timing analysis is in high precision, a small amount of RFI could easily distort the integrated pulse profile, resulting in unpredictable errors in the measured TOAs and their related uncertainties. Some of the seriously affected TOAs will behavior as outliers in the timing residuals. As I describe above, outliers mainly come from the low-S/N regime, we can also identify outliers with the S/N criterion. Arzoumanian et al. (2015) carefully investigated the signal-to-noise cutoff criterion and decided to remove TOAs obtained from profiles S/N less than 8. After that, manual identification was carried out to remove remaining outliers caused by very low-level RFI, instrumental errors, etc by inspecting the original archives. In this work, I adopt this approach and manually eliminated outliers after removing TOAs with profiles S/N less than 8.

2.4.1.2 Scintillation

As described in section 1.2.4, pulsars will show large flux density variations due to the interstellar scintillation. Scintillation causes pulsar radiation to vary as a function of frequency and time, causing interference, the interference maxima in the dynamic spectrum, known as scintles. The characteristic bandwidths and timescales of scintles at L-band are typically on the order of hundreds of MHz and hours, but since broadband receivers are now widely used, the pulse profile could be dominated by the scintles at either the top or the bottom of the observing band i.e. 2.2, leading to frequency-averaged pulse shape variation with frequency and time due to this random weighting.

In the frequency-resolved data, some sub-bands or channels could become very weak and dominated by noise. During the RFI mitigation step, these sub-bands and channels are not removed, this causes certain sub-band to produce outliers in the frequency-resolved timing. These outliers could significantly influence the timing results and must be removed before further timing analysis.

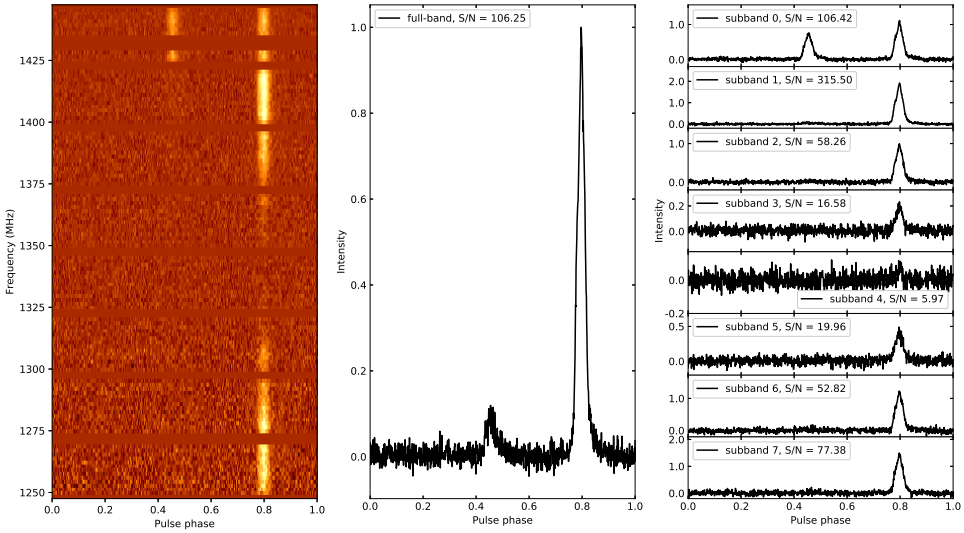

Figure 2.2 An illustration of the outliers in sub-band, the top band is due to band edge reflection while the middle band is significantly influenced by scintillation. Data for this example is from J1744-1134 observed with Effelsberg telescope.

2.4.1.3 Facility Error

Uncorrected instrumental effects also cause profile variability. Bad calibration of the polarization will cause distortions in the pulse shape. The main goal of polarization calibration is to recover the pulsar profile properly, regardless of the influence of IISM. Some pulsar sources, such as PSR J1022+1001 point by van Straten (2013) require a high level of polarization calibration to reach the best timing precision.

Another facility factor that could produce outliers in timing residuals is clock error. Unknown discrete time-offsets would also lead the whole observation to act as an outlier. For example, Asterix back-end at Effelsberg has experienced several discrete time-offsets while the corrections are only preliminary determined.

Besides, as shown on the top band of Figure 2.2, the effect of band edge reflection, also known as a ghost image, would lead to the appearance of excess power at the edges of each channel. The ghost artifact signal is mainly due to the imperfect ADCs sampling process (Kurosawa et al., 2001; Verbiest & Shaifullah, 2018).

2.4.1.4 Solar Wind

The solar wind (SW) is a stream of plasma and particles flowing outward from the upper atmosphere of the Sun to space. This plasma and particles is a mix of electrons and ions and alpha particles. Similar to the IISM, the SW could introduce a characteristic dispersive delay to many of the Galaxy pulsars.

Under current PTA precision, it is possible to timing some MSPs to a precision close to 100 ns over ten years. However, there are several major factors, such as the SW, that could cause significant time delays. For instance, Lyne et al. (1988) investigated several observations of the Crab pulsar (PSR B0531+21) within 5 degrees from the Sun and found that the time delay as a result of the SW could reach as much as 500 μs at 610 MHz. You et al. (2007a) studied observations of PPTA pulsars with small ecliptic latitude at 1400 MHz and show that the SW effect can contribute TOA errors of 100 ns when the LOS to the pulsar passes within around 60 degrees of the Sun. Tiburzi et al. (2019, 2021) also demonstrated the SW effects depend strongly on the LOS angle to the Sun and can become extremely large when the LOS to pulsars at a small solar angle.

There are several ways to mitigated the SW influence on pulsar timing. Generally, The TEMPO2 is equipped with several models to account for the SW. The default model is based on the assumption of a constant, spherically symmetric model that is only determined by the electron density at 1 au and the angle between the LOS to the pulsar and the Sun. Alternatively, due to the fact the SW variability induces DM variations, You et al. (2007b) and Keith et al. (2013) demonstrated two models to measure the DM changes due to the SW using the Wilcox Solar Observatory and multi-frequency observation respectively. In addition, (Madison et al., 2019) presented a technique to filter out long-timescale DM variations due to IISM and extract the imprint of the SW from the full collection of DM measurements.

However, since the SW is a very complicated phenomenon and many features are not well understood, it is difficult to eliminate the impact thoroughly. Normally, owing to few observations at extremely small solar angles, the PTA experiments just remove observations taken within a certain angle from the Sun. In this work, I adopt this practice and removed the observations with a solar angle smaller than 10 degrees.

2.4.2 Outlier Rejection Scheme

The existence of outliers will significantly affect the precision of pulsar timing, especially in the frequency-resolved timing framework of faint pulsars, the ratio of outliers may be as high as 20%, which makes it difficult to manually identify and eliminate outliers, so in this subsection, I will briefly introduce several commonly used outlier elimination algorithms.

According to Hotan et al. (2005), the normally used cross-correlation method used during the template matching process will turn unreliable in the low S/N regime and thus yield underestimated TOA uncertainties. Besides, the distribution of Normalized residuals in this regime will also fail to fit the Gaussian curve in this condition.

To evaluate the quality of the observation-to-template matching process, a standard reduced chi-squared for the goodness-of-fit (GOF) is returned along with the TOA estimation (Verbiest et al., 2016). GOF is the total squared difference between observation and template normalized by the statistical degrees of freedom. But the GOF could only be obtained at the 'FDM' algorithm with PSRCHIVE/*pat* package. Another method, however, is based on the median absolute deviation. For example, TOAs that located three times away from a robust linear fit for f^{-2} through Huber regression (Huber, 1964; Wang et al., 2017) will be identified as outliers and eliminated (Tiburzi et al., 2019). However, this method is inapplicable in the case which has limited TOAs.

As I describe above, outliers mainly come from the low-S/N regime, we can also identify outliers with the S/N criterion. Arzoumanian et al. (2015) carefully investigated the signal-to-noise cutoff criterion and decided to remove TOAs obtained from profiles S/N less than 8. After that, manual identification was carried out to remove remaining outliers caused by very low-level RFI, instrumental errors, etc by inspecting the original archives. In this work, I adopt this approach and manually eliminated outliers after removing TOAs with profiles S/N less than 8. After that, manual identification was carried out to remove remaining outliers caused by very low-level RFI, instrumental errors, etc by inspecting the original archives.

Chapter 3

A Comparative Analysis of TOA Creation Methods

This chapter was also submitted for publication as a research article to Astronomy & Astrophysics.

Abstract: Extracting precise pulse times of arrival (TOAs) and their uncertainties is the first and most fundamental step in high-precision pulsar timing. The creation of TOAs is a complex and multi-faceted enterprise. In addition, there is some diversity in the practices used around the world.In this paper, we present a comprehensive comparison of TOA creation algorithms, specifically focusing on the creation of timing templates, TOA determination algorithms and TOA bandwidth. We compare the value of data-derived template profiles as compared to analytic profiles and evaluate the three most commonly used template-matching algorithms. Finally, we study the relation between timing precision and TOA bandwidth to identify any potential breaks in that relationship. As a practical demonstration, we apply our selected methods to European Pulsar Timing Array data on the three test pulsars PSRs J0218+4232, J1713+0747 and J2145−0750. Our demonstration shows that data-derived and smoothed templates are typically preferred to some more commonly applied alternatives; the Fourier-domain with Markov-chain Monte Carlo (FDM) template-matching algorithm is generally superior to or competitive with other algorithms; and while the optimal TOA bandwidth is strongly dependent on pulsar brightness, telescope sensitivity and scintillation properties, some significant frequency averaging seems required for the data we investigated.

3.1 Introduction

Millisecond pulsars (MSPs, first discovered by Backer et al., 1982) are neutron stars which have been spun up or "recycled" to rotation periods shorter than $\sim$30 ms through accretion of matter from a binary companion star (Alpar et al., 1982; Bhattacharya & van den Heuvel, 1991). Their extremely stable rotation periods make MSPs ideal laboratories to test a diversity of extreme astrophysical phenomena that cannot be accessed on Earth. Their applications include investigating the interstellar medium (Demorest, 2011; Keith et al., 2013), testing relativistic gravity (Kramer et al., 2006b; Taylor & Weisberg, 1982), building a pulsar-based time standard (Hobbs et al., 2019), constraining masses in the Solar System (Caballero et al., 2018) and detecting gravitational radiation (e.g., Shannon et al., 2015).

Detecting nano-Hertz gravitational waves (GWs) using pulsar timing is one of the main foci in pulsar-timing research at present (see the recent reviews by Burke-Spolaor et al., 2019; Tiburzi, 2018). It had been predicted (Jenet et al., 2005) that a detection can be achieved by monthly observations of 20 to 40 MSPs over five to ten years if these sources are characterized by white timing residuals with a root-mean-square (RMS) of $\sim$ 100 ns. In order to achieve this ambition, three major Pulsar Timing Arrays (PTAs, see Foster & Backer, 1990; Romani, 1989) were constructed: the Parkes Pulsar Timing Array (PPTA, Manchester et al., 2013), the European Pulsar Timing Array (EPTA, Desvignes et al., 2016; Janssen et al., 2008) and the North-American Nanohertz Observatory for Gravitational waves (NANOGrav, Demorest et al., 2013). These three were subsequently combined in the International Pulsar Timing Array (Perera et al., 2019; Verbiest et al., 2016). Even though substantial progress has been achieved in improving timing precision and sensitivity in subsequent data releases, both at the regional and global level, a detection has so far not been achieved, primarily due to two limiting factors. Firstly, even the most up-to-date and highest-quality data sets (like, e.g., the NANOGrav data set from Alam et al., 2021a,b) have too few pulsars with timing precision below or at the 100-ns level. Secondly, there are a number of corrupting effects, whose impact on timing precision requires careful consideration (Shannon & Cordes, 2012; Verbiest & Shaifullah, 2018). One example of recent progress in that regard, is the influence of the Solar-System Ephemerides, which was known to affect GW experiments (Tiburzi et al., 2016), but it was not properly taken into account until more recently (e.g., Arzoumanian et al., 2018b). Beyond this, several fundamental aspects of pulsar-timing analyses were identified as potential targets for optimization and harmonisation efforts during the first global PTA data combination (Verbiest et al., 2016). Three particular recommendations from that work will be described below and investigated in detail throughout this paper.

Firstly, all standard pulsar-timing analyses are based on matching a so-called template or "standard" profile to the observations. There are, however, several different ways in which

such template profiles can be constructed. As outlined by Lorimer & Kramer (2005), traditionally template profiles are constructed through addition of a large number of observations, thereby resulting in a pulse profile with a far higher signal-to-noise ratio (S/N) than any given observation. Such templates have the advantage that they by definition fully resemble the actual pulse shape, but the noise of the original observations is also contained in the template and hence may cause inaccurate correlations commonly referred to as "self-standarding" (Hotan et al., 2005). Three strategies have been devised to mitigate this issue: firstly, the template profile can be smoothed; secondly the template can be restricted to contain only the single brightest observation (which is then removed from the subsequent timing analysis and only used as template profile); and thirdly the template can be modeled with noise-free analytic functions (Lorimer & Kramer, 2005). As can be seen in, e.g., Demorest et al. (2013); Desvignes et al. (2016); Kerr et al. (2020) several of the above-mentioned approaches are presently in use, but no comprehensive comparison of the various template-creation options has been published.

Secondly, after a template profile has been created, the time of arrival (TOA) of a given observation is derived from the cross-correlation between the observation and the template. Traditionally this has been done in the Fourier domain, by fitting the phase-gradient of the cross-power spectrum of the template and the observation (Taylor, 1992), commonly referred to as the Phase Gradient Scheme ("PGS") method. However, the standard implementation of this approach has often been found to report underestimated uncertainties. One suggested solution determines the TOAs in the same way, but derives the TOA uncertainties from a Monte-Carlo analysis (referred to as the "FDM" algorithm). This latter solution has been suggested (Verbiest et al., 2016) as being superior. Furthermore, Hotan et al. (2005) proposed a Gaussian-interpolation ("GIS") cross-correlation algorithm (CCA) in the time-domain, which is supposedly better suited to low-S/N data sets. While recent pulsar-timing efforts have increasingly adopted the FDM algorithm, usage of the PGS method is still widespread (Desvignes et al., 2016), in some cases (Demorest et al., 2013) with lower bounds imposed on the pulse S/Ns in order to avoid the worst underestimation of TOA uncertainties. Here too a comprehensive, comparative evaluation of the possible alternatives has so far not been undertaken.

Lastly, potential corruptions in the derived TOAs can arise from the usage of data-recording systems with large ($\gtrapprox$0.3) fractional bandwidths (Verbiest & Shaifullah, 2018). This is particularly the case if the pulse-profile changes shape across the band *and* the scintillation bandwidth is of the same order as (or slightly smaller than) the observing bandwidth. Both of these conditions appear to be likely if the fractional bandwidth is large (Dai et al., 2015; Levin et al., 2016), causing the frequency-averaged profile shape to

vary from one observation to the next. If the TOAs are derived from frequency-averaged observations and template, then the aforementioned variations will be reflected in the TOAs and in the TOA uncertainties, worsening the overall timing precision. One solution to this problem is to carry out two-dimensional template matching where both observation and template have frequency resolution and where in addition to the phase offset (or TOA) a frequency drift (or dispersion measure) is determined (Liu et al., 2014; Pennucci et al., 2014a). An alternative solution is to derive multiple TOAs across the bandwidth of the observation (Arzoumanian et al., 2015; Demorest et al., 2013), either against a frequency-averaged template or through matching each channel of the observation against the corresponding channel in the template. In all of this, it is an unsolved question which TOA bandwidth would be optimal: too narrow a bandwidth would leave little signal and create TOAs that have high levels of radiometer noise, too wide a bandwidth and the scintillation effects risk becoming significant – the optimal TOA bandwidth is likely strongly pulsar dependent.

To date, PTAs either fully frequency averaged their TOAs (Desvignes et al., 2016), used timing-model extensions to correct for profile-shape variations (Demorest et al., 2013) or have carried out a mixed approach where both frequency-averaged and frequency-resolved TOAs have been derived (Kerr et al., 2020).

The three detailed aspects of TOA creation outlined above are investigated in this paper. Specifically in Section 3.2 we introduce the data and pulsars we use to test and compare the aforementioned aspects of timing on these data; in Section 3.3 we describe the various analysis methods that were compared: template creation is discussed in Section 3.3.1, template matching algorithms in Section 3.3.2 and optimal TOA bandwidth determination in Section 3.3.3. We discuss our findings on the three test pulsars in Section 3.4 and summarize of our findings in Section 3.5.

3.2 Observations

Our analysis is based on data from the newest generation of data recorders at four of the radio telescopes that constitute the EPTA: the Effelsberg radio telescope (designated as EFF), the Jodrell Bank Lovell radio telescope (JBO), the Nançay decimetric radio telescope (NCY) and the Westerbork synthesis radio telescope (WSRT). Details on the observing systems used at each of these observatories are given below. The pulsars used for this initial investigation are PSRs J0218+4232, J1713+0747 and J2145−0750. These three pulsars were chosen because they represent a variety of characteristics. Specifically, PSR J1713+0747 is very bright, with a small duty cycle, and is one of the most precisely timed MSPs in PTAs. PSR J0218+4232 has a relatively high dispersion measure (DM), is fainter and consequently not as well timed.

Table 3.1 Basic parameters for the pulsars in our sample. Parameters are merely indicative and have been rounded. As an indication of the timing precision, the weighted RMS residual is quoted for the IPTA combination that provided the best timing precision for the given pulsar, rounded to one significant digit. ECORR refers to the mean "frequency-averaged EQUAD parameter" (Arzoumanian et al., 2014) and is a measure for the strength of SWIMS present in a given pulsar.

Parameter	J0218+4232	J1713+0747	J2145−0750	References
Period (ms)	2.3	4.6	16.1	Bailes et al. (1994); Foster et al. (1993); Navarro et al. (1995)
DM (cm/pc^3)	61	16	9	Bailes et al. (1994); Foster et al. (1993); Navarro et al. (1995)
Orbital Period (days)	2.0	67.8	6.8	Arzoumanian et al. (2018a); Desvignes et al. (2016)
Flux density S1400 (mJy)	0.9	9.1	10.3	Dai et al. (2015); Kramer et al. (1998)
Pulse Width W50 (%)	43	2.4	2.1	Manchester et al. (2013); Stairs et al. (1999)
IPTA Timing RMS (μs)	7	0.2	1	Perera et al. (2019); Verbiest et al. (2016)
IPTA ECORR	–	0.16	1.3	Perera et al. (2019)

Table 3.2 Description of the observational set-up for the data used in this paper. Given are the telescope identifier (see text), the name of the data recording device (referred to as "back-end"), the centre frequency f_c of the observations, the observing bandwidth BW (not considering RFI or band-edge removal), the number of frequency channels N_{chan} and the number of phase bins across the profile N_{bin}. Note that for our analysis the number of phase bins was in all cases reduced to 256.

Telescope	back-end	f_c (MHz)	BW (MHz)	N_{chan}	N_{bin}
EFF	PSRIX	1347.5	200	128	1024
JBO	Roach	1532	400	400/1600	2048
NCY	NUPPI	1484	512	128	2048
WSRT	PuMa II	1380	160	512	512

PSR J2145−0750 is in between the other two in terms of brightness and timing precision, but has a significantly longer spin period and appears to have more significant stochastic wide-band impulse-modulated self-noise (or SWIMS, Osłowski et al., 2011, commonly also known as pulse-phase jitter).

Some basic properties for these three pulsars are given in Table 3.1; the observatory-specific details of the observations used are given in Table 3.2 and the number and date ranges of the observations are given in Table 3.3.

In addition to the telescope-specific RFI-mitigation strategies described below, all data were visually inspected through the software suite PSRCHIVE (Hotan et al., 2004a; van Straten et al., 2012) before TOAs were derived as described in Section 3.3. Specifically, since the data near the edge of each sub-band are corrupted by aliasing and spectral leakage problems, these channels are excised with the PAZ program.

Table 3.3 Summary of observations used in this paper. For each pulsar-telescope combination the number of observations N_{obs}, MJD range and observing time span T is given.

PSR	Tel ID	N_{obs}	MJD	T (yrs)
J0218+4232	EFF	53	55600–57705	5.8
	JBO	128	55666–58559	7.9
	NCY	467	55854–58558	7.4
	WSRT	65	54775–57131	6.5
J1713+0747	EFF	96	55633–58713	8.4
	JBO	301	55905–58610	7.4
	NCY	368	55800–58558	7.6
	WSRT	112	54155–57195	8.3
J2145−0750	EFF	62	55633–57733	5.7
	JBO	122	55880–58495	7.2
	NCY	265	55803–58555	7.5
	WSRT	85	54520–57135	7.2

3.2.1 Effelsberg Radio Telescope

The Effelsberg radio telescope is a homological Gregorian design with a 100-m paraboloidal primary reflector and a 6.5-m ellipsoidal secondary reflector, which makes the Effelsberg radio telescope the world's second-largest fully movable telescope. It operates at wavelengths from about 90 cm to 3.5 mm (i.e. observing frequencies from 300 MHz to 90 GHz).

The data from Effelsberg presented in this research were acquired with a typical cadence of 3–4 weeks between 2011 and 2019 with an integration time per source of about 30 min per observation. The data recorder (henceforth referred to as "back-end") used was the PSRIX pulsar-timing system (Lazarus et al., 2016), which is based on ROACH boards and carries out coherent de-dispersion on CPUs using the DSPSR (van Straten & Bailes, 2011) package. The observations were taken with the P-217 and P-200 receivers, centered at 1.3475 GHz in a frequency-multiplexing mode where eight 25-MHz-wide sub-bands are independently dedispersed and written to disk. This results in observations with a total of 200 MHz of bandwidth, 128 frequency channels, 1024 phase bins of 4.47 μs width, 10-second integrations and full polarization information.

These data were combined in time and frequency with the PSRADD command of the PSRCHIVE package (Hotan et al., 2004a; van Straten et al., 2012). Subsequently radio-frequency interference (RFI) was removed automatically with CLEAN.PY, the RFI excision script of the COASTGUARD package (Lazarus et al., 2016), using the "surgical" algorithm.

3.2.2 Lovell Radio Telescope

At Jodrell Bank Observatory the 76-m Lovell telescope is used in a regular pulsar-monitoring program, from which the observations used here were taken. Specifically, these observations were taken at 1.532 GHz centre frequency over a time-span of ∼7.5 years with a typical cadence of three weeks and typical integration time of 15 minutes. For PSR J1713+0747 the cadence was closer to one week. The back-end used for these observations was a ROACH-based back-end very similar to the one used at the Effelsberg observatory and described by Lazarus et al. (2016), and using the DSPSR package (van Straten & Bailes, 2011) for real-time coherent de-dispersion.

The JBO observations have an effective bandwidth of 400 MHz split over 25 16-MHz-wide sub-bands, each channelized into 1 or 0.25 MHz wide frequency channels. The number of phase bins varies between 256 and 2048 depending on the pulsar observed.

To remove the RFI, the spectral kurtosis method for real-time RFI removal (Nita et al., 2007) was applied during the DSPSR pre-processing, after which the data were run through some basic RFI-removal scripts and finally were visually inspected for excluding the remaining RFI.

3.2.3 Nançay Decimetric Radio Telescope

Built in 1965, the Nançay Decimetric Radio Telescope (NCY) is a Kraus-type telescope with a collecting area of 6912 m^2, equivalent to a 94-m parabolic dish. Since 2011, NCY observations of pulsars are done with the ROACH-based NUPPI back-end (Cognard et al., 2013), a version of the Green Bank Ultimate Pulsar Processing Instrument (DuPlain et al., 2008) designed for Nançay. With a total bandwidth of 512 MHz, the NUPPI back-end splits the full bandwidth into 128 channels, each channel with 4 MHz bandwidth. The observations used here were centered at 1484 MHz and were coherently dedispersed in real-time on GPU units that are part of the NUPPI system.

The pulsars were observed with NUPPI since 2011 with a cadence that varied between five and ten days and with an integration time between 45 and 60 minutes per observation. Various automated RFI excision schemes were applied in post-processing offline.

3.2.4 Westerbork Synthesis Radio Telescope

The Westerbork Synthesis Radio Telescope (WSRT), located in the Netherlands and operated by the Netherlands Institute for Radio Astronomy (ASTRON), is an east-west interferometric

array with 14 25-m parabolic dishes, which in terms of collecting area is equivalent to a 94-m single telescope.

Pulsar monitoring at the WSRT has been carried out at 350 MHz, 1.38 GHz and 2.27 GHz with the Pulsar Machine II (PuMaII) back-end (Karuppusamy et al., 2008). Pulsar observations are recorded in eight 20-MHz-wide sub-bands, for a total observing bandwidth of 160 MHz with 512 ($= 8 \times 64$) frequency channels. Coherent de-dispersion is performed offline with the DSPSR package.

The observations used in this paper were taken at a centre frequency of 1380 MHz, had a cadence of roughly one month and a total integration time of about 30 minutes.

3.3 Data Processing Techniques

In this section we describe the different algorithms and methods we use and compare. Specifically, the template creation methods are described in Section 3.3.1, the template-matching algorithms are outlined in Section 3.3.2 and the analysis to determine the optimal TOA bandwidth is described in Section 3.3.3. All of these algorithms and methods make use of the PSRCHIVE and TEMPO2 (Hobbs et al., 2006) software packages.

3.3.1 Template Creation and Comparison

The ideal template describes the pulse profile shape in perfect detail, without additive noise. A vital and complicating aspect in this regard is the fact that the achievable timing precision for a given profile shape is a strong function of the higher-frequency components present in the profile shape, i.e. of sharp features in the profile (e.g., van Straten, 2006). Consequently, depending on the pulsar in question, noise-mitigation methods like smoothing or modeling of template profiles may require particular care in order to prevent negative impacts on the timing potential of a given pulsar.

Common approaches towards template generation were already discussed in the introduction, thus here we summarize the four different methods we compare:

Single-brightest observation (henceforth "single"): Here we take the observation with the highest S/N for use as a template and remove it from the observations to be timed. This approach has the advantage that all true features of the pulse profile are present in the template, but the disadvantage that the template tends to have higher noise levels than in alternative approaches. While this approach is convenient for pulsars that have large variations in S/N since the noise present in the template for such pulsars may be negligible in comparison to the noise present in the typical observation. However,

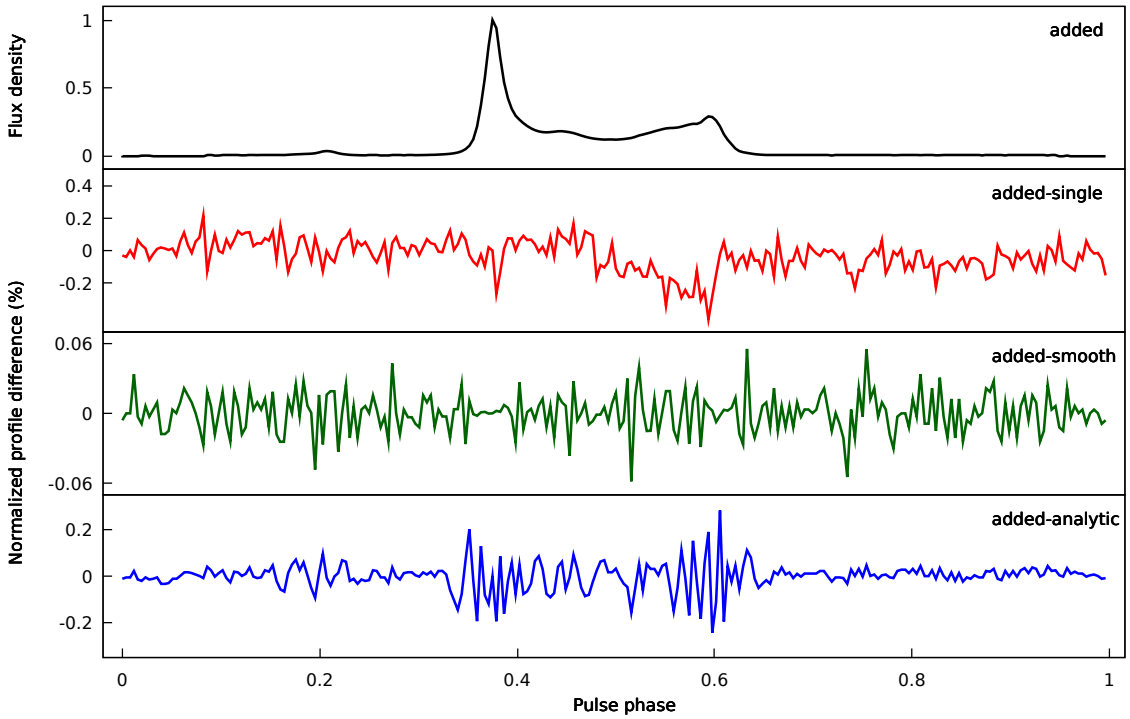

Figure 3.1 Peak-normalized added template profile and profile differences for PSR J2145−0750 data from the NCY.

in the case that the dataset is composed of a limited number of observations, it can be disadvantageous to exclude the most valuable (i.e. brightest) observation from the timing.

All observations added (henceforth "added") : This approach also has the advantage that by definition all true profile features are present in the template; and particularly for pulsars with stable S/Ns the added template profile would have a much higher S/N than the single template. The main disadvantage is the risk of self-standarding (Hotan et al., 2005), which is typically expected to be significant for profiles that are comprised of less than multiple hundreds of observations. For pulsars that scintillate significantly, the increase in S/N will be less dramatic and even larger numbers of observations may be required to avoid the issue of self-standarding.

Added with smoothing (henceforth "smoothed"): Here the added profile is taken as a basis and a smoothing filter is applied subsequently. Specifically in the following we will use templates smoothed with the default wavelet-based smoothing algorithm (Demorest et al., 2013), i.e. with a Daubechies wavelet with factor 8. Limited testing

with variations of the smoothing parameters and wavelets used indicated that these generally did not result in significantly different results for our analysis. The advantage of this approach is that the self-standarding issue should be removed as the noise in the template is largely suppressed, but this comes at the cost of a potential loss or suppression of sharp features in the pulse profile. An added complication is that smoothing algorithms can introduce artefacts in the template. The precise application of the smoothing algorithm could in itself be expanded to a far more extensive study, as results may also depend on the number of phase bins across a profile (i.e. the extent to which high-frequency profile features are resolved or not), but for the present work we restrict ourselves to the most standard application of this method, in order to limit the dimensionality of our optimization problem.

Analytic profile (henceforth "analytic"): For this profile, von Mises functions were fitted to the added profile. Given the high S/N of the added profiles, a large number of components was typically required. Components were added and fitted interactively to avoid overfitting and to ensure as good a template profile as possible. This method has the clear advantage that the template profile is truly noise-free, but often not all sharp features may be represented in the profile, either because they are mis-identified as noise or because the analytic function cannot be indefinitely extended without affecting the stability and convergence of the least-squares fit. Consequently self-standarding is of no concern, but timing precision may be compromised. Another advantage of as analytic template (do with Gaussians) is that it can be scaled to any profile resolution, e.g., same template for different set ups.

An illustration of how the different methods compare is included in Figure 3.1 which shows the profile shape of the added template for the NCY data of PSR J2145−0750 and the profile differences of the added template with the other three templates. As expected the difference with the single and smoothed templates is primarily white noise. Some apparently non-white variation is noticeable (at the 0.2% RMS as integrated level) in the single-pulse difference plot towards the end of the pulse profile, which may be due to calibration errors that would average out in the added profile but which may affect individual observations more significantly, or due to the fact that the frequency-averaged pulse profile can vary because of scintillation. The profile difference with the smoothed template consists purely of white noise that is independent of pulse phase; and the difference with the analytic profile shows how in this particular case this approach does not succeed in accurately describing the profile, leaving some high-frequency profile-shape differences particularly in the vicinity of the pulse edges. It is noteworthy that many of the features that are removed in the wavelet smoothing, are also removed by the analytic modeling. In other words, the difference profiles of the

smoothed and of the analytic templates show a significant number of matching features, particularly in the off-pulse phase range. Furthermore the difference between the single and added profile is also significant and not merely consistent of noise. This is likely due a combination of profile evolution across the bandwidth and scintillation. While the added profile would have scintillation effects mostly averaged out (hence showing the profile shape averaged across the bandwidth), the single-brightest observation is severely affected by a scintle at the bottom of the band.

Note that throughout the presented work the aforementioned templates are used only in their frequency-averaged form, except for the analysis focused on the optimal TOA bandwidth. In that case the single, added and smoothed templates were also created in frequency-resolved form[1].

3.3.2 Time of Arrival Determination Algorithms

After creation of a template profile, the TOA of a given observation can be determined by matching the observation to this template. Specifically, the observation $\mathscr{O}$ can be related to the template $\mathscr{T}$ as (Taylor, 1992):

$$\mathscr{O}(\phi) = a + b\mathscr{T}(\phi + \tau) + n(\phi),$$

where ϕ is the rotational phase, a is an arbitrary offset, b is a scale factor, τ is the phase offset between observation and template and $n(\phi)$ is a noise term. In order to solve for τ, a variety of possible algorithms have been proposed. We will compare three of the more commonly used algorithms, described briefly below.

Fourier Phase-Gradient (PGS): The most common template-matching algorithm used to date (and the default algorithm used in the PSRCHIVE software package) is the so-called PGS algorithm described in detail by Taylor (1992). Based on the Fourier shift theorem, it matches the template to the observation by fitting for a slope in the Fourier space. A clear advantage of this approach is that the result does not depend on the phase resolution of the data and as such can result in significantly more precise measurements than time-domain cross-correlation methods (which, according to Taylor, 1992, are limited to a precision about ten times smaller than the data's resolution). The main disadvantage of this method is that in the low-S/N regime it underestimates the TOA

[1] A comparative analysis of frequency-resolved analytic templates (as developed by Liu et al., 2014; Pennucci et al., 2014b) is deferred to a separate study, given the inherent complexity and multi-dimensional analysis necessary for such work. The comparison of frequency-averaged data-derived, analytic and smoothed templates which we present here will meaningfully inform such a future frequency-resolved analysis

uncertainty since the TOA distribution no longer follows a Gaussian distribution (see the discussion in Arzoumanian et al., 2015, Appendix B.).

Fourier-Domain with Markov-Chain Monte-Carlo (FDM): One proposed solution to the underestimation of low-S/N TOA uncertainties is to probe the likelihood–phase shift dependence with a one-dimensional Markov-Chain Monte-Carlo, from which the TOA variance can be derived. This results in TOA values that are identical to those of the PGS algorithm, but TOA uncertainties that are more realistic (i.e. larger), particularly for low-S/N observations.

Gaussian Interpolation Shift (GIS): This algorithm carries out a standard cross-correlation of the template and observation in the time domain; and determines the phase offset by fitting a Gaussian to the cross-correlation function, whereby the centroid of the resulting Gaussian is defined as the TOA; the offset required to double the χ^2 of the template-observation comparison is defined as the TOA uncertainty (Hotan et al., 2005). As mentioned above, this time-domain method has limited precision, but it was proposed as a more robust TOA determination method in the low-S/N regime.

The application of a Gaussian in determining the peak position of the cross-correlation function should result in timing precision exceeding 10% of a phase bin, although this likely depends on the exact pulse shape.

3.3.3 Time of Arrival Bandwidth and Jitter Noise

As receiver systems for pulsar timing have had an exponential growth in their observational bandwidth, the traditional approach of using frequency averaging observations to create total profiles (and TOAs) has become sub-optimal. The primary reason for this is the potential for making the derived TOAs less precise due to the combined effects of scintillation and frequency evolution of the pulse profile shapes.

At the other extreme, TOAs determined using native frequency resolution (referred to hereafter as "fully frequency-resolved TOAs") significantly decreases the S/N, occasionally leading to the low-S/N regime where some template-matching algorithms don't provide reliable uncertainties anymore. Consequently, there must be an optimal TOA bandwidth which maximizes the TOA precision by limiting the deleterious effects of both low S/N in fine frequency channels and those due to scintillation and profile evolution.

Here we have investigated such an optimal TOA bandwidth for a set of pulsar and back-end combinations, by quantifying the achievable timing precision as a function of the TOA bandwidth. To do so, we combined the best template-matching algorithm with a

frequency-resolved version of the optimal template profile, and then carried out the timing of each pulsar and back-end combination of our test dataset for a range of possible TOA bandwidths. This allowed us to investigate the improvement in the goodness of fit via the reduced chi-squared of the linearized least squares fit and the RMS of the timing residuals, as well as the number of TOAs that remain after removing TOAs corresponding to total intensity profiles with S/N less than 8, following Arzoumanian et al. (2015).

Since radiometer noise is proportional to the square root of the TOA bandwidth while jitter noise or SWIMS (Cordes & Downs, 1985; Liu et al., 2012; Osłowski et al., 2011) behaves as a constant noise term, added in quadrature to the radiometer noise to achieve the timing RMS, the expected result of the analysis is that the RMS converges to a constant value as the TOA bandwidth increases:

$$\sigma_{\mathrm{res}} = \sqrt{\frac{C}{TB} + \sigma_{\mathrm{J}}^2}, \tag{3.1}$$

Here σ_{res} is the residual RMS of the post-fit residuals, C is a constant defined by the radiometer equation, T is the integration time of the TOAs, B is the bandwidth of the TOAs and σ_{J} is the RMS introduced by SWIMS. This last term is proportional to $1/N \propto 1/T$, with N being the number of pulses contained in each TOA[2].

Although the above analysis could be used to accurately determine the SWIMS amplitude for the observed pulsars, several complications prevent precise determination of σ_{J}. Firstly, RFI removal leads to a variable effective bandwidth for a significant number of TOAs. Secondly, at small bandwidths many TOAs have very large error bars and artificially reduce the RMS as the models then become over-specified. Finally, not all observations have the same length, implying that any value derived for σ_{J} from a formal fit of Equation 3.1 to a sequence of $\sigma_{\mathrm{res}}(B)$ measurements is related to an ill-defined integration length. Finally, in cases where the scintillation bandwidth is significantly larger than a single frequency channel, but smaller than the observing bandwidth, unweighted frequency-averaging of data will result in enhanced timing RMS for TOA bandwidths that are smaller than the scintillation bandwidths, as TOAs within scintles will continue to improve their uncertainties with the square root of the TOA bandwidth, but once the TOA bandwidth exceeds the scintillation bandwidth, data from channels away from scintles will dampen the TOA precision. This will result in an artificial worsening of the timing residual RMS for TOA bandwidths beyond the scintillation bandwidth; and consequently will lead to an overestimate of the SWIMS amplitude σ_{J}. An example of this latter phenomenon is shown in Figure 3.2.

[2]For the relatively limited fractional bandwidths considered in this work, this term is unrelated to the TOA bandwidth (Sallmen et al., 1999)

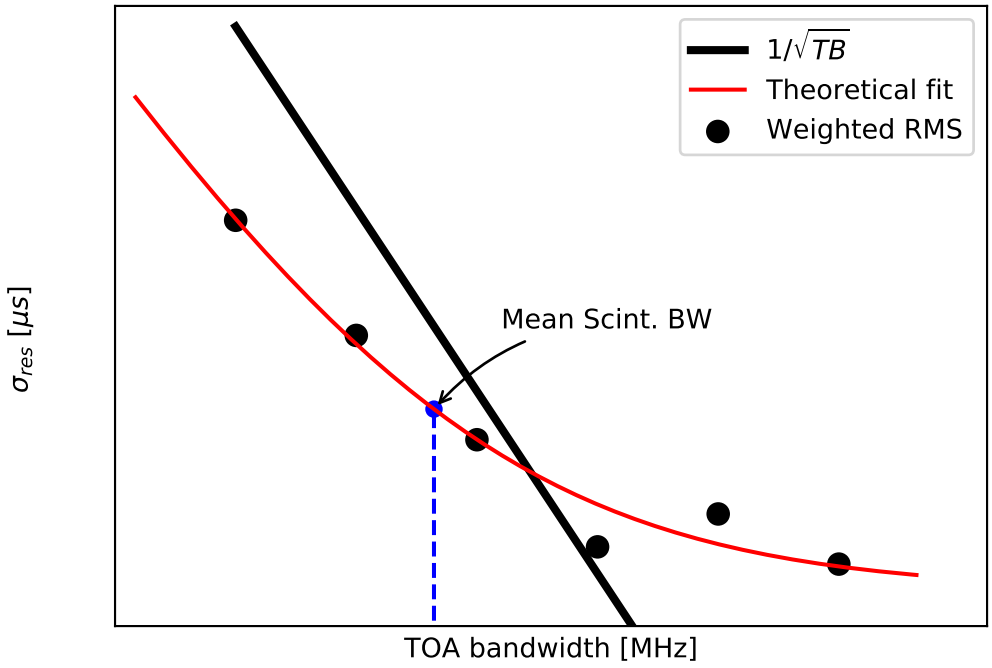

Figure 3.2 A sketch of the dependence of σ_{res} on TOA bandwidth, for an idealized dataset. The black dots represent RMS values, the blue dashed line indicates the median scintillation bandwidth and the red line is a fit of Equation 3.1. The black line is for the case of pure radiometer noise, i.e., with no jitter noise noise ($\sigma_j = 0$) and for a unity radiometer constant (C=1).

While the above considerations prevent a meaningful connection to the physical phenomenon of SWIMS, our analysis does allow a phenomenological determination of which TOA bandwidth optimally balances the various effects that impact the final timing RMS.

3.4 Results and Discussion

To evaluate the timing precision as a function of the choice of template and CCA described in Sections 3.3.1 and 3.3.2, we adopted the relevant timing models presented in Desvignes et al. (2016). Those timing models were updated by combining the TOAs presented there, as well as the data utilized in this work.

For each combination of the templates and CCAs described in Section 3.3, we then perform a TEMPO2 (Edwards et al., 2006; Hobbs et al., 2006) analysis, fitting now only for the pulsar spin and its first derivative as well as position and proper motion parameters. For each fit, the reduced χ^2 and the residual RMS value were recorded.

For this work, we do not model any red noise processes, while the DM models employed are similar to those presented in the analysis of Desvignes et al. (2016), since the aim is limited to comparing the performance of the templates and CCAs given a fixed model.

For each of these TOA sets we also recorded the resulting timing residuals.

Figures 3.3 and 3.4 demonstrates that the GIS scheme is the least reliable, typically leading to heavily underestimated error-bars. As the pulsar brightness increases, the GIS derived TOAs appear to perform slightly better (although this algorithm was developed to be more effective on low S/N observations), but still does not perform as good as either the PGS or FDM methods. Further, the “single” templates perform poorly, leading to TOA sets with the greatest variance as well as, the least precise TOAs. “Added” templates generally lead to the best TOA sets for the brighter sources while for the low S/N PSR J0218+4232 “analytical” or “smoothed” templates are preferred

Figure 3.3 presents a pulsar and telescope-wise analysis of the timing performance. Here the poor performance of the GIS TOAs is clearly visible, across all systems. Further, it is evident that FDM and PGS results often cluster for the two stronger sources, with FDM results generally leading to almost identical reduced χ^2 and RMS values, independently on the template creation method. This shows that the effect of template choice can be somewhat mitigated for such sources when these CCAs are used. Finally, the PGS and FDM clusters appear to trade places in terms of the reduced χ^2.

The timing residuals for each of the TOA sets were further assessed to check for the presence of a large unmodelled signal. Using a 2-tailed Kolmogorov-Smirnov test we compared the distribution of these residuals against those expected for residuals containing a purely

Gaussian or power-law signals or, a combination of both. We find that the timing residuals for all TOA sets are Gaussian or a Gaussian and power-law mixed distributions, suggesting that the updated timing models are sufficient given our data. As a result, the residuals have close to normal distributions as shown in Figure 3.4a, except for PSR J0218+4232 when the GIS CCA is used with the added template. Further, the kurtosis of the residual distributions (see Figure 3.4b) shows that while FDM TOA always produce thin-tailed distributions, in the case of stronger in-band profile evolution as shown by PSR J2145−0750 the PGS CCA can lead to a fat-tailed distribution (having a non-zero kurtosis value), i.e. leading to some TOAs appearing to be significantly offset. Such TOAs limit any automated outlier removal procedures and thus FDM TOAs are preferred for large, automaticaly generated datasets even if the overall timing RMS is not minimised.

For each pulsar, the timing performance as a function of the TOA bandwidth was assessed using TOAs created with the 'added' template with the FDM CCA, by splitting the archives into multiple channels. The exact choice of the number of channels is specific to the telescope to accommodate for the different bandwidths. At Effelsberg, the NCY and WSRT the archives were either fully scrunched in frequency or split into channels in multiple of two up to maximum of 32. Due to a different native resolution at Jodrell Bank, the data were either scrunched in frequency or split into five or multiples of ten, up to a maximum of forty channels.

Following the method described in section 3.3.3, for each choice of number of channels, a standard TEMPO2 timing analysis was carried out, fitting for the same timing parameters as in Section 3.3 and the resultant RMS for each pulsar and telescope is plotted in Fig. 3.5.

From these plots, it is evident that the telescope dependent, achievable RMS decreases asymptotically as a function of the TOA BW, as shown by the fit lines in Fig. 3.5. While the lower telescope gain for JBO clearly limits this achievable, for the other three telescopes a combination of factors influence the final limit on the minimum RMS.

For PSR J0218+4232, where the overall S/N of the profile continuously increases with greater channel bandwidth, the overall timing RMS also continuously decreases. However, beyond $\sim$500 MHz, the RMS starts to be limited by the system noise. Although J0218+4232 is known to exhibit "Large Amplitude Pulses" (Joshi et al., 2004), we do not find a significant influence of those pulses in our data because of the extended integration lengths which imply averaging over several million pulses for each TOA.

For PSRs J1713+0747 and J2145−0750, we find that the asymptotic RMS limit lies close to a TOA BW of about 1 GHz, with there being only a marginal improvement in the minimum RMS after 500 MHz for PSR J2145−0750, while for PSR J1713+0747 that limit

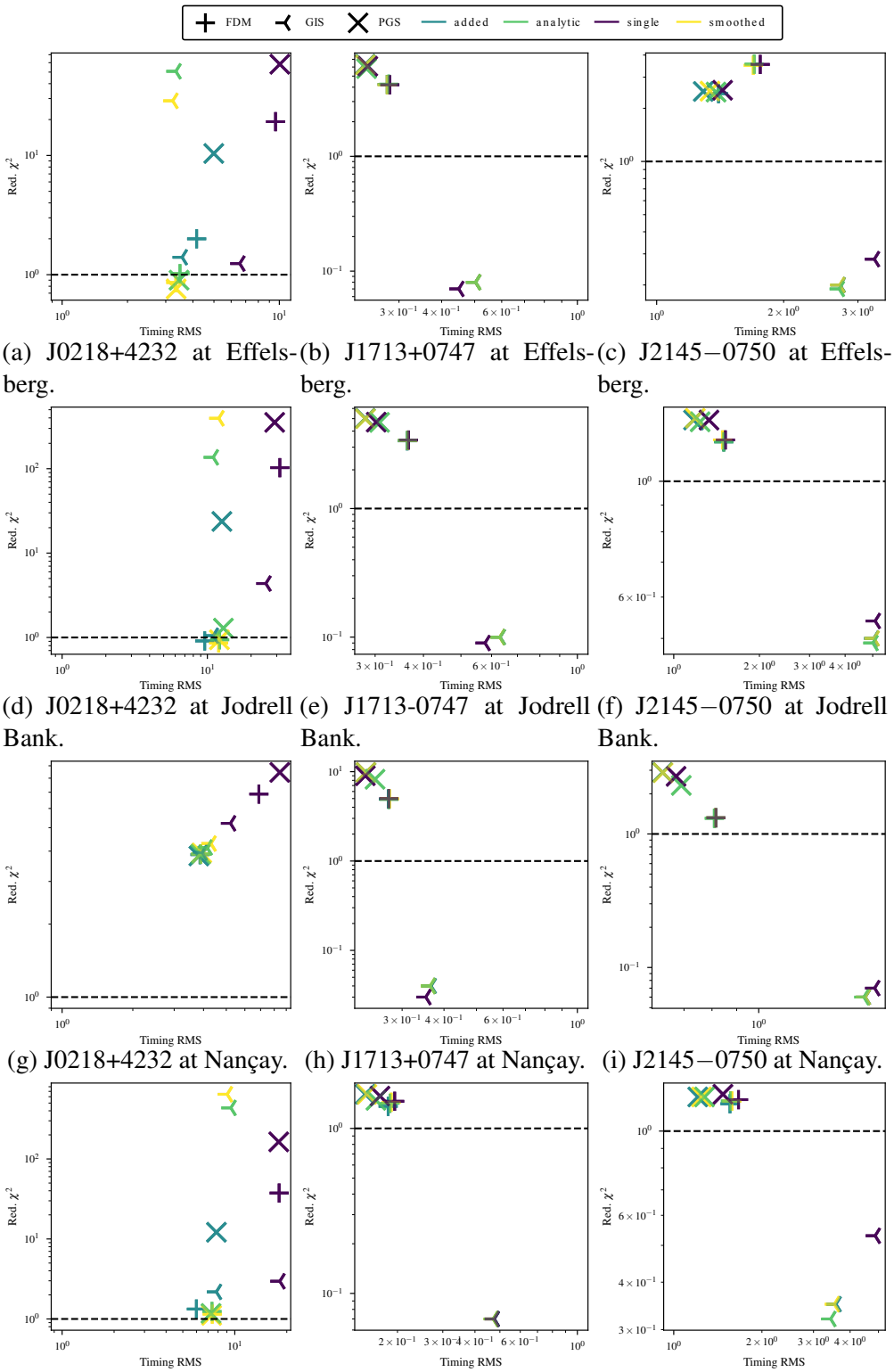

(a) J0218+4232 at Effelsberg.
(b) J1713+0747 at Effelsberg.
(c) J2145−0750 at Effelsberg.
(d) J0218+4232 at Jodrell Bank.
(e) J1713-0747 at Jodrell Bank.
(f) J2145−0750 at Jodrell Bank.
(g) J0218+4232 at Nançay.
(h) J1713+0747 at Nançay.
(i) J2145−0750 at Nançay.
(j) J0218+4232 at Westerbork.
(k) J1713+0747 at Westerbork.
(l) J2145−0750 at Westerbork.

Figure 3.3 Reduced χ^2 and residual RMS for the three pulsars as a function of the selected CCA and template and the different telescopes.

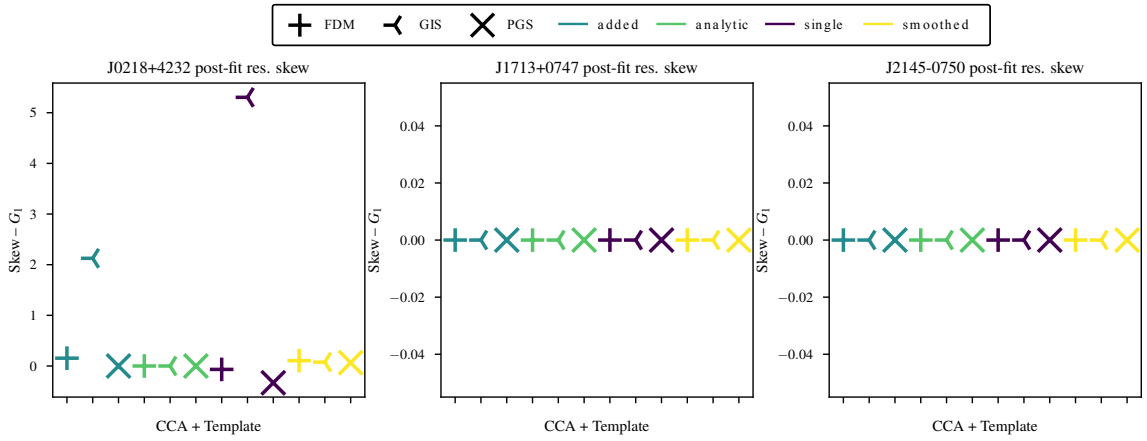

(a) Skew† of the post-fit residuals, for each CCA and template combination.

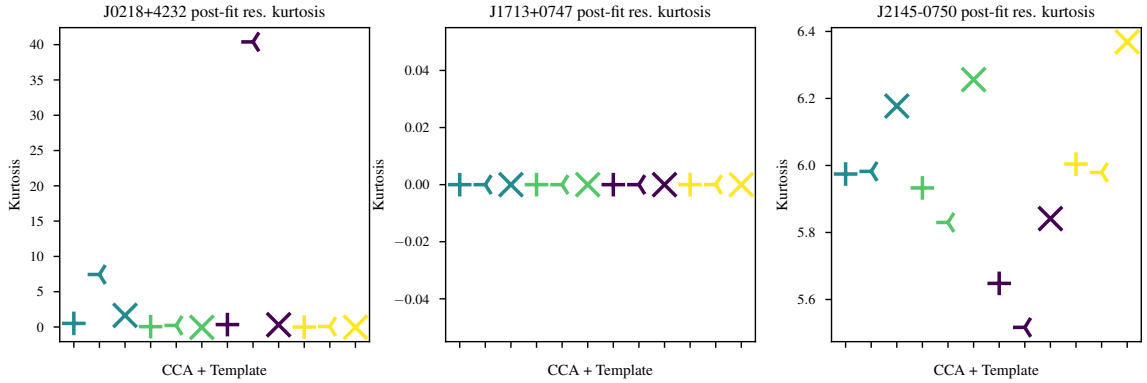

(b) Kurtosis of the post-fit residuals, for each CCA and template combination.

Figure 3.4 Properties of the post-fit residuals obtained for each CCA and template combination. The symbols and colours are identical to those in Fig. 3.3. † The skew measure reported above is the adjusted Fisher–Pearson standardized moment coefficient.

lies at around 100 MHz for the Effelsberg, Jodrell Bank and Westerbork telescopes whilst for the Nançay Radio Telescope this limit moves to ∼500 MHz.

As described in Section 3.3.3, these limiting RMS (henceforth "system limited noise floor"; SLNF) include a measurement of the system and band noise, as defined in e.g., Lentati et al. (2016). Even though this limits the possibility of measuring the intrinsic SWIMS contribution, we still find that for all TOA BWs less than or equal to the scintillation bandwidth for a given pulsar (i.e., the gray bands plotted for Figs. 3.5b and 3.5c) the SLNF is artificially boosted. However, at TOA BWs greater than twice the scintillation BW, the SLNF rapidly falls to its minimum for a given system.

3.5 Conclusions

With regards to the choice of the template generation scheme, we find that the single brightest observation leads to the worst timing performance. For the brighter pulsars the added, smoothed and analytic templates lead to comparable, minimum timing RMS and red. χ^2, but for the lower S/N PSR J0218+4232 added templates can perform worse than the smoothed and analytical templates.

The analysis presented above also upholds the recommendation of Verbiest et al. (2016); the CCA of choice for high precision PTA work being the FDM algorithm. In all pulsar, telescope and back-end combinations tested above, we find that FDM TOAs lead to the most reliable TOAs, simultaneously improving the average timing residual and at the same time leading to a more realistic estimate of the 'system limited timing noise'.

However, we also find that in the case of bright pulsars, PGS derived TOAs can perform similarly. Especially for archival data, where PGS might have already been employed, we suggest that those TOAs may be retained, if recreation of the TOAs using FDM is not possible. However, PGS derived TOAs appear to produce a larger amount of outliers, which places limits on any automated outlier rejection. Further, in almost all combinations, while PGS TOAs lead to a decreased timing RMS, the model fits appear to be worse (i.e., the red. χ^2 is increased) relative to the corresponding values for FDM TOA sets.

In addition, we find the GIS derived TOAs are not suitable for high-precision timing, leading to conservative timing models and a loss of model parameter sensitivity.

Using the FDM CCA with added templates, we find that the optimal TOA bandwidth for minimizing the achievable timing residual RMS is at least twice the scintillation bandwidth for a given system.

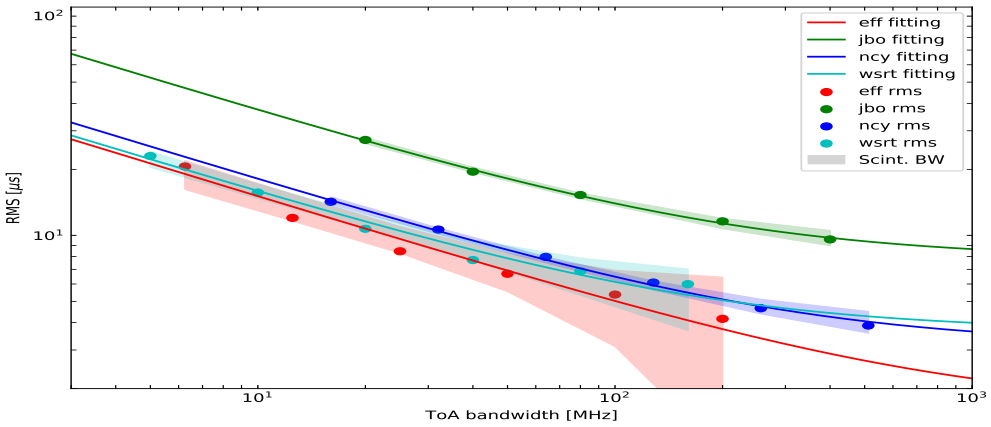

(a) 'System limited' timing noise estimates of J0218+4232.

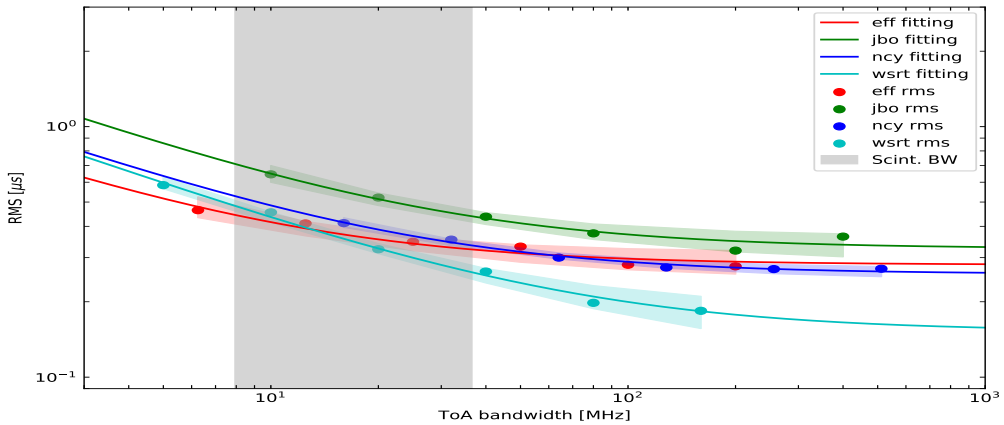

(b) 'System limited' timing noise estimates of J1713+0747.

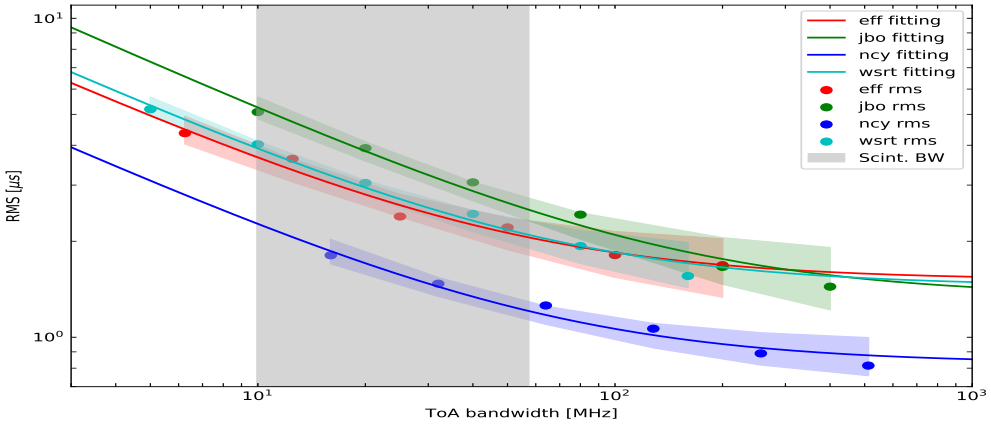

(c) 'System limited' timing noise estimates of J2145−0750.

Figure 3.5 System limited noise floor (SLNF) estimates for the three pulsars, when using the added template with the FDM CCA to generate TOA with the available bandwidth at each telescope divided into the respective number of channels. The shaded regions along the fitted curves are the interquartile ranges for the fit, representing the error bounds on the estimated SLNF. The gray vertical bands show the expected scintillation bandwidth, estimated from the same dataset as we present here (Liu et al, in preparation).

Chapter 4

Improving Pulsar Timing Precision through Optimal TOA Creation

This chapter is going to be submitted for publication as a research article to Astronomy & Astrophysics.

Abstract: The measurement of pulsar pulse time of arrivals (TOAs) can be done through template-matching of each pulse profile with a standard template. While there are several combinations of templates and cross correlation algorithms (CCAs) that can be adopted to determine TOAs and their uncertainties, utilizing different combinations may lead to inconsistent results. In the previous chapter, using a subsample of pulsars to reflect the different signal-to-noise regimes typical for pulsar timing array (PTA) data, we demonstrated that data-derived templates combined with the FDM cross-correlation algorithm are usually superior except for a few extreme cases. We now extend this analysis to thirteen MSPs, using more than ten years of data from the European PTA (EPTA). Utilizing the frequency-resolved templates, we assess the system-limited noise floor (SLNF) for each pulsar at various telescopes in the band centered around 1.4 GHz. With this method, we also investigate the optimal TOA bandwidth which can balance the radiometer noise and phase-jitter noise. We conclude that the effect of pulse phase jitter noise is not the limiting factor for EPTA timing precision, since the jitter levels we derive are far smaller than the radiometer noise.

4.1 Introduction

Since their discovery, the short spin periods and extremely stable rotation characteristics of Millisecond pulsars (MSPs, Backer et al., 1982) have enabled myriad applications in testing fundamental physics. These applications include high-precision tests of general reality (GR, Freire et al., 2012; Kramer et al., 2006b; Weisberg et al., 2010; Zhu et al., 2015), exploration of the ionized interstellar medium (IISM, Keith et al., 2013; You et al., 2007a), development of pulsar-based timescales (Hobbs et al., 2012), constraints on the equations-of-state for neutron stars (Demorest et al., 2010; Lattimer & Prakash, 2007), measurement of the model-independent properties of the pulsar itself (Verbiest et al., 2008), etc. However, one of the most significant applications of regular pulsar timing observations is the detection and characterization of low-frequency (nano-Hertz) gravitational waves (GWs, see e.g. Hobbs et al., 2010; Verbiest et al., 2009), i.e. fluctuations in the fabric of space-time due to the propagation of GWs, predicted by the theory of GR (Misner et al., 1973, see e.g.,). Due to the extended distance between pulsars and the earth, PTAs, which are composed of an array of MSPs, is most sensitive to low-frequency GW signals (Perera et al., 2019; Verbiest et al., 2016). The potential sources of GWs in this band are likely an ensemble of SMBHBs, whose combined, stochastic signal gives rise to the GWB. GWs have a unique quadrupolar signature in the pulsar timing residuals, and a method based on the correlation between pulsar pairs on the sky, as a function of the angular separation, known as the "Hellings and Downs" curve (Hellings & Downs, 1983) can be used for identifying the signature of GWs.

Pulsar timing analysis determines the differences, also known as timing residuals, between the observed TOAs and the predicted TOAs, based on models for the astrometry and ephemeris of the MSPs in the array. An accurate and detailed model would yield precise timing residuals. However, the timing precision, which is quantified by the value of RMS of the timing residuals, is limited by several categories of noise rooted either in the pulsar itself, propagation path, or the observing system. To improve the timing precision and maximize the probability of GW detection, various analysis methods, as well as hardware upgrades, have been investigated and employed in PTA observations and the data analysis process. However, the influence of different data analysis pipelines in disparate telescopes has not been well investigated. Chapter 3 (Wang et al., 2021) demonstrated a method to compare the influence of diverse template possibilities and CCAs with three pulsars, and concluded that the data-derived and smoothed templates are typically preferred while the Fourier-domain with Markov-chain Monte Carlo (FDM) template-matching algorithm is generally superior to other algorithms. However, due to the limited number of pulsars in chapter 3 (Wang et al., 2021), these results need to be inspected and verified with a larger sample of the EPTA pulsars.

In this paper, we verify the results present in Chapter 3 (Wang et al., 2021) with thirteen MSPs observed with the EPTA telescopes. The selection of these pulsars has followed the significance of EPTA pulsars (see Figure 4.1)as determined by Babak et al. (2016). Thus we inspect the achieved timing precision as a function of the chosen templates and CCAs. In addition, the timing floor of each pulsar in the four EPTA telescopes is also examined. This chapter is organized in the following manner. In Section 4.2, we present an overview of the observations and data reduction methodologies we used in this research. We describe the timing result pulsar by pulsar in Section 4.3. Finally, we discuss these results in detail and briefly summarize our conclusions in Section 4.4.

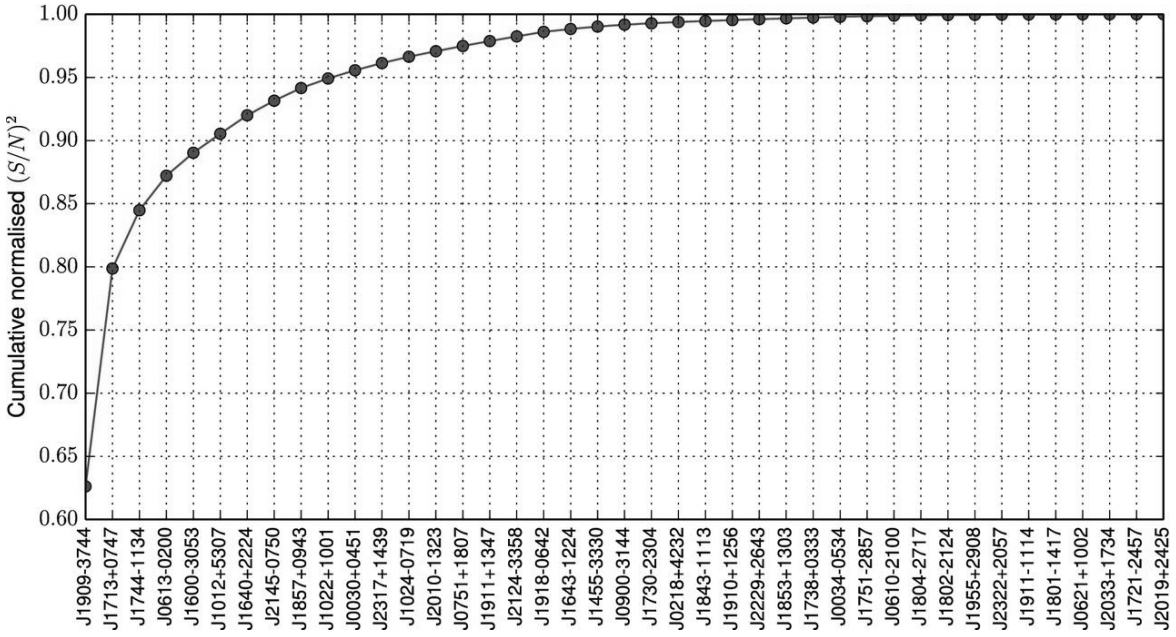

Figure 4.1 Cumulative normalized $(S/N)^2$ from the most constraining pulsar to the least constraining. The plot shows the cumulative *S/N* square over the total *S/N* square. The ranking reveals that the pulsar timing array is significantly dominated by the six most precisely timed pulsars. The other pulsars in the array, i.e. PSR J1640+2224 and subsequent, contribute a far lower degree of sensitivity to the Hellings-Down correlated signal.
Image Credit: Babak et al. (2016)

4.2 Observations and Analysis Procedure

This paper reports on observations of an array of MSPs at L-band [1] from four EPTA telescopes made over a 13-year span from 2007 to 2020. The EPTA is a multinational European

[1] L-band refers to the frequency range of 1–2 GHz in the radio spectrum.

Table 4.1 Details of the observing set-ups of the different EPTA telescopes relevant to this research.

Telescopes	EFF	JBO	NRT	WSRT
Pulsar back-end	PSRIX	ROACH	NUPPI	PuMa II
Frequency (MHz)	1347.5	1532	1484	1380
Bandwidth (MHz)	200	400	512	160
Average length (min)	30	20	50	30
Number of channels	128	400	128	512
Number of phase-bins	1024	512	1024	512

collaboration formed with the primary ambition of the direct detection of low-frequency GWs. The concept and aim of this organization is first described in detail by Stappers et al. (2006) and a more detailed overview of EPTA telescopes, the observing system as well as the primary sources list are described by Desvignes et al. (2016).

The data set described in this paper is collected at EFF, JBO, NRT and WSRT with the newest generation of instruments, respectively; the PSRIX (Lazarus et al., 2016), ROACH (Bassa et al., 2016), NUPPI (Cognard et al., 2013; Liu et al., 2014), and PuMa II (Karuppusamy et al., 2008). All thirteen of the sources investigated in this paper were observed at weekly to monthly intervals for the EPTA program, with the exception of NRT, which observes more frequently. At EFF, the observations were recorded across 200 MHz bandwidth with a centre frequency of 1347.5 MHz. Data collected from both of the multi-beam and single-pixel 21 cm receivers were used for this work. Typically, each pulsar is observed once a month with an integration time of approximately 30 minutes. The pulsars observed with the Lovell telescope at JBO were recorded using the ROACH back-end with a center frequency of 1532 MHz across a total bandwidth of 400 MHz. The NRT observations span around 10 years, from 2011 to 2020, with an average cadence of about 5 to 10 days. Data were recorded at the NRT with a centre frequency of 1484 MHz. The total 512 MHz bandwidth id channelized into 128 channels and coherently de-dispersed. The WSRT observations were carried out at a centre frequency of 1380 MHz across a bandwidth of 160 MHz. At WSRT the pulsars were observed fo $\sim$ 30 minutes each time and with a interval of around one month. The details of the bandwidths, frequency, and average length of the observations in each telescopes are given in table 4.1.

In tables 4.2 and 4.3, we summarize the details of the pulsars, MJD range as well as the number of observations retained after the preliminary data quality inspection.

The timing models used in this research are mostly based on Desvignes et al. (2016), but with the reference clock and the Solar system ephemeris updated to “TT(BIPM2019)” and

Table 4.2 Overview of the pulsars' properties and observations.

PSR	EFF		JBO		NRT		WSRT		Data span
	MJD Range	N_{obs}	MJD Range	N_{obs}	MJD Range	N_{obs}	MJD Range	N_{obs}	(yr)
J0030+0451	55633-58859	55	56095-58495	101	55803-59152	706	56080-57113	35	9.6
J0613−0200	55600-58620	91	56253-58494	83	55817-58851	318	54337-57096	101	12.4
J1022+1001	55660-58769	109	55600-58131	184	55839-58853	280	54154-57153	80	12.9
J1012+5307	55633-59083	103	55655-58495	144	55816-59288	799	54165-57153	83	14.0
J1024−0719	55633-59223	79	55674-59120	158	55891-59153	393	54287-57118	75	13.3
J1600−3053	55661-58621	60	56255-58559	84	55809-58852	624	54155-57131	62	12.9
J1640+2224	55633-58620	94	55653-58467	95	55826-58850	369	54155-57101	86	12.9
J1744−1134	55628-59161	87	55670-58560	94	55805-59212	213	55792-57154	52	9.4
J1857+0943	55633-58824	64	56011-58559	121	55800-58837	235	54337-57177	81	12.4
J1909−3744	-	-	-	-	55812-59277	515	-	-	9.5
J1918−0642	55633-59223	76	55652-58838	86	55874-59138	169	54490-57190	86	13.0
J2010−1323	56206-59223	34	55657-58494	96	55850-59149	298	54492-57148	75	13.0
J2317+1439	55633-58824	58	55662-58495	83	55850-58849	701	54490-57117	78	11.9

"DE438", respectively. Since we do not intend to investigate the parameters of the timing model, only the rotational frequency and its first derivative are fitted for in the study of templates and CCAs. But as the dispersion measure at different sub-bands varies, we fitted the DM, and also its first and second derivatives when possible, for the system limited noise floor (SLNF) investigation.

Before any further processing, the data should first have any radio-frequency interference (RFI) excised. All data, except those from JBO, were initially processed with the *clean.py* tool from the COASTGUARD package (Lazarus et al., 2016) to excise polluted channel-subintegration combinations. Any remaining RFI was then manually and interactively removed by visual examination with the PSRCHIVE (Hotan et al., 2004a) *pazi*/*paz* tools. For JBO data, a newly developed python package CLFD (Morello et al., 2019), which identifies and zero-weights RFI with Tukey's rule (Tukey, 1977) in a three dimensional feature space (standard deviation, peak-to-peak difference and absolute value of the second bin of the profile's Fourier transform), is automatically applied.

4.3 Results

In this section, we describe the individual results for the 13 pulsars in our sample and assess the impact of template and CCA choice for data from the different EPTA telescopes. In addition, we illustrate the system limited noise floor analysis as well as optimal TOA bandwidth determination. We first discuss individual pulsars with distinct results. For pulsars with common results, we describe them together at the end of this section.

Table 4.3 Overview of the pulsars' properties.

PSR	P (ms)	$\dot{P}(10^{-20})$	P_b (day)	DM (cm^{-3} pc)	$S_{1.4}$ (mJy)	Ref.
J0030+0451	4.865	1.02	-	4.33	0.6	Lommen et al. (2000); Verbiest et al. (2016)
J0613−0200	3.062	0.96	1.20	38.79	1.7	Lorimer et al. (1995b); Verbiest et al. (2016)
J1012+5307	5.26	1.71	0.60	9.02	2.8	Lange et al. (2001); Nicastro et al. (1995)
J1022+1001	16.453	4.33	7.81	10.25	6.1	Camilo et al. (1996); Desvignes et al. (2016)
J1024−0719	5.162	1.86	-	6.49	1.5	Bailes et al. (1997); Manchester et al. (2013)
J1600−3053	3.598	0.95	14.35	52.33	2.5	Jacoby et al. (2007); Manchester et al. (2013); Ord et al. (2006)
J1640+2224	3.163	0.28	175.46	18.43	0.4	Desvignes et al. (2016); Foster et al. (1995)
J1744−1134	4.075	0.86	-	3.14	1.0	Bailes et al. (1997)
J1857+0943	5.362	1.78	12.33	13.30	3.3	Segelstein et al. (1986); Verbiest et al. (2016)
J1909−3744	2.95	1.40	1.53	10.39	1.0	Desvignes et al. (2016); Jacoby et al. (2003)
J1918−0642	7.646	2.57	10.91	26.55	0.6	Edwards & Bailes (2001b); Janssen et al. (2010)
J2010−1323	5.223	0.48	-	22.16	1.6	Jacoby et al. (2007)
J2317+1439	3.445	0.24	2.46	21.90	4.0	Camilo et al. (1993); Verbiest et al. (2016)

While we have already demonstrated the poor behavior of the templates from the single brightest observation, as well as the GIS CCA in Chapter 3 (Wang et al., 2021); we recover the same result for the majority of our current sample. Thus we will skip the comparison and description of the single template and GIS CCA analysis in the following text unless a unique result is obtained for a given pulsar, telescope and back-end combination.

4.3.1 PSRs J0030+0451 and J2010−1323

PSRs J0030+0451 and J2010−1323 are two isolated MSPs among our sources. PSR J0030+0451 is one of the nearest known MSPs in the Galaxy, with a distance of ∼325 pc (Arzoumanian et al., 2018a). Its pulsed emission can be detected at various EM frequencies, including X-ray (Becker et al., 2000), radio (Lommen et al., 2000) and γ-ray (Abdo et al., 2009). Since the pulsar is likely to be influenced strongly by the Solar Wind (SW) at low solar angles, the observations taken when the angular separation from the Sun is less than 10 degrees are excluded in our analysis (Tiburzi et al., 2021). PSR J2010−1323 was discovered by Jacoby et al. (2007) during the high galactic latitude survey. At some of the EPTA telescopes only a small number of observations were made of these two pulsars and thus our results must be interpreted with care for those datasets. PSR J0030+0451 was only observed 35 times at WSRT while PSR J2010−1323 had 34 observations. In addition, both of these pulsars possess extremely low S/N, with a mean S/N of 25.30 and 50.02, respectively. This limited number of observations and low mean S/N have a significant impact on the timing analysis and SLNF fitting. These problems are worsened by the outlier rejection scheme as shown in Chapter 3 (Wang et al., 2021), which works primarily on the basis of S/N criterion.

For the extreme cases with EFF and WSRT, the results of template and CCA choices return two completely opposite directions. For PSR J0030+0451 at WSRT, the added templates combined with PGS present an almost halved RMS compared with FDM, and both of these two possibilities are significantly superior than other combinations. However, the situation for PSR J2010−1323 at EFF is totally inversed, where the added template combined with PGS yields an almost doubled RMS compared with FDM, while other combinations present consistent and reasonable results.

Concerning the SLNF analysis, the fitting of these two special cases fail due to the low S/N, since for the small TOA bandwidth cases, a larger proportion of TOAs are removed by our outlier rejection scheme, leading to biased RMS values.

Except the specific cases mentioned above, these two pulsars, when observed with the other telescopes, lead to results in accordance with the conclusions drawn in chapter 3 (Wang et al., 2021): added and smoothed templates are typically preferred to some more commonly applied alternatives, and the FDM template-matching algorithm is generally superior to or competitive with other algorithms. The RMS values obtained with NCY decrease more quickly than other telescopes as a function of TOA bandwidth, and the asymptotic RMS limit appers to be reached with a TOA bandwidth of about 1 GHz.

4.3.2 PSR J1012+5307

PSR J1012+5307 was found by Nicastro et al. (1995) in a 14.5-hour binary system, with an extremely low-mass helium-core white dwarf, $\sim 0.16 M_{\odot}$, companion (Callanan et al., 1998; van Kerkwijk et al., 1996). Making use of data from EFF and JBO, Lange et al. (2001) presented a precision timing model of PSR J1012+5307 and determined the detailed 3D velocity motion for this binary system with a combination of radio timing and optical observations. Lazaridis et al. (2009) revisited PSR J1012+5307 and improved the 3D velocity information with 15 years of EPTA data. One of the noticeable results is the obtaining of a new intrinsic eccentricity upper-limit of $< 8.4 \times 10^{-7}$, making it one of the smallest values for a binary system.

PSR J1012+5307 is one of the most frequently observed pulsars within the EPTA, especially with the NCY telescope. While this pulsar is being observed once per month at EFF, JBO, and WSRT, NCY observes this pulsar roughly every four days. For the EFF data, this pulsar shows a dramatically high χ^2_r which is likely caused by profile variations due to uncalibrated polarization (see Figure 4.2). Except for that telescope, the conclusions are uniform. The combination of added template and FDM yields more reliable and precise TOAs. PGS may result in slightly better RMS but would increase the χ^2_r dramatically.

Through the SLNF fitting in Figure 4.11, it is clear that EFF does not perform well with this pulsar, and increasing the TOA bandwidth does not significantly lower the RMS.

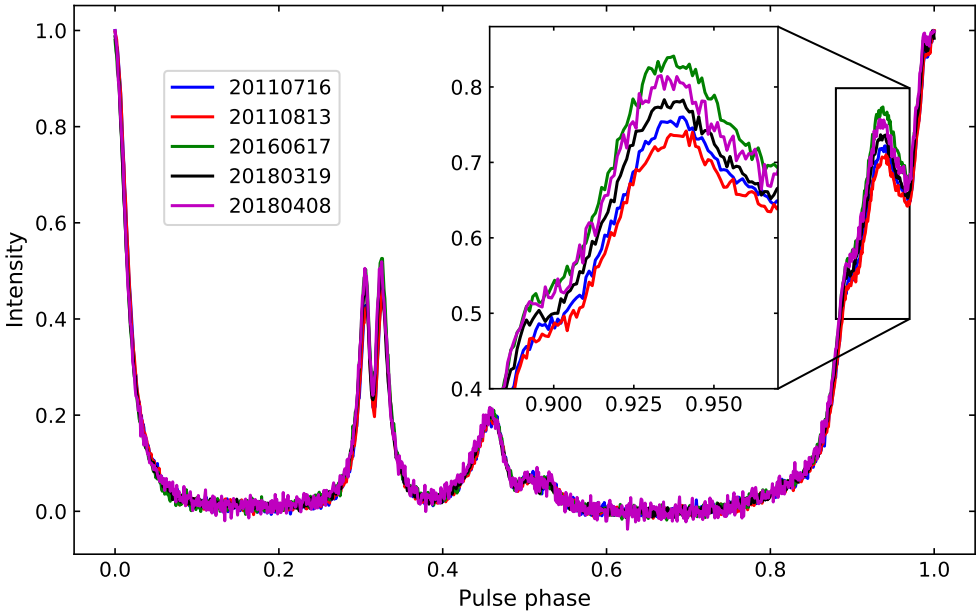

Figure 4.2 Profile variations of PSR J1012+5307 at EFF. The leading component of the main pulse is zoomed in at the subplot. These variations are not found in other telescopes, and thus we attribute these variations to instrumental problems specific to EFF, especially issues with polarization calibration.

4.3.3 PSR J1022+1001

The averaged pulse profile of PSR J1022+1001 at L-band is characterized by two prominent peaks. While the trailing peak component is highly linearly polarized, the leading component does not show strong polarization (Hotan et al., 2004b). The pulse profile of PSR J1022+1001 is observed to show strong intrinsic variations with frequency, e.g. see Figure 4.3, (Liu et al., 2015; Ramachandran & Kramer, 2003). Since the pulsar also strongly scintillates at L-band, the intensity ratio of its leading and trailing peaks varies distinctly with time. While Kramer et al. (1999) assert that the profile variations in the integrated pulse profile cannot be the result of instrumental and propagation effects, van Straten (2013) find that instrumental polarization artifacts are the main contribution to the profile instability. van Straten (2013) put forward a new polarimetric calibration method, referred to as Measurement Equation Template Matching (METM), to resolve this instability. Based on this new method, timing

results from 7.2 years of data of this pulsar from the Parkes radio telescope show that the standard deviation of arrival time residuals derived from METM-calibrated data is two times smaller than with conventional calibration methods.

Besides the profile variation, this pulsar also has a very low ecliptic latitude (as low as -0.06 deg), which indicates that the pulsar signals could be significantly influenced by the SW. Generally, the SW contribution could induce DM fluctuations and an incomplete model of that variation could introduce up to a few microseconds of delay in the TOAs (Tiburzi et al., 2021). However, since only a tiny fraction of the observations were taken within 10 degrees in solar elongation and no special SW corrections are applied to the data, we excluded the observations taken when the Solar elongation is less than 10 degrees.

Within our data set, we noticed significant profile variations within the observed frequency band as well, especially in EFF, JBO, and NCY data. In WSRT data, the profile variations are still noticeable (presumably due to the narrow bandwidth), but not as obvious as other telescopes. Also due to the loss of calibrator files, the observations of this pulsar obtained with EFF are not polarization calibrated, the EFF TOAs consequently show a high χ^2_r-value. Accounting for the high χ^2_r due to the variations, the timing precision at all telescopes consistent with each other, this can be expected due to the extremely strong radiation of this pulsar.

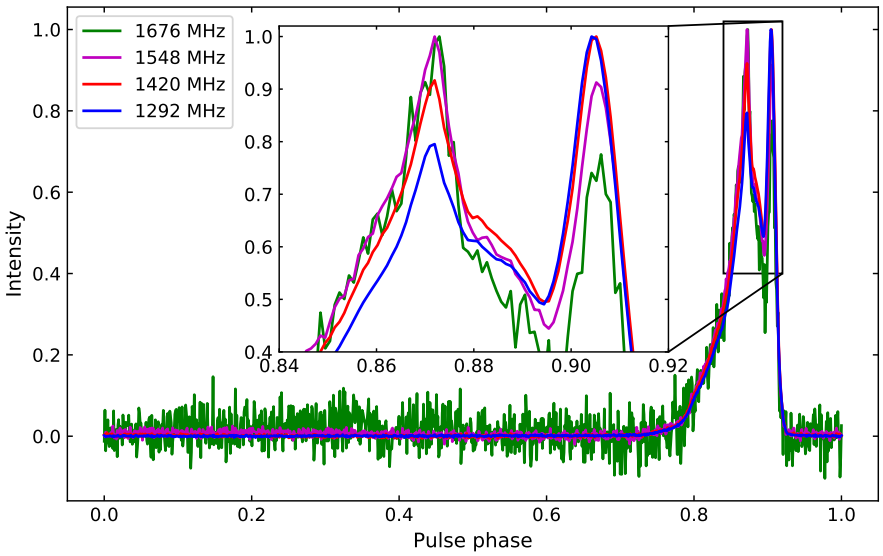

Figure 4.3 An example of profile variation of PSR J1022+1001 at NCY as a function of frequency. The data were polarization calibrated.

For this pulsar, the WSRT data possesses the lowest SLNF, and the RMS decreases as a function of TOA bandwidth, similar to JBO and NCY. However, the EFF data behaves differently. The increase of TOA bandwidth does not improve the RMS as dramatically as others, which is attributable to the lack of calibration for those data.

4.3.4 PSR J1600−3053

PSR J1600−3053 is a relatively bright MSP considering its large dispersion measure as shown in Table 4.3. This binary MSP was discovered in the Swinburne high galactic latitude pulsar survey (Jacoby et al., 2007). Since then, the pulsar has been well timed at very high precision due to its intrinsically narrow pulse profile and high brightness.

During our analysis, we noticed that this pulsar is affected by strong DM variations from the end of 2014 onwards. Figure 4.4 shows the DM time series for PSR J1600−3053 determined with the NCY dataset. We calculated the DM offset with the method described in Donner et al. (2020) and introduced the '-dmo' flag in the TOA files to correct for this variation. After correcting the DM variation effects, the templates and CCAs results are shown in Figure 4.7. We notice that for this pulsar, the added template works very well. The most dramatic improvement appears on WSRT data, where added template accompanied with the PGS method decrease the RMS significantly and the χ^2_r value becomes consistent compared with other telescope data.

For this pulsar, the profile difference (see Figure 4.7), between the added and smoothed analytic templates are obvious, especially with the NCY data. Alternative smoothing functions or fitting with more Gaussians did not remove these features, which may account for the slight worsening of the smoothed and analytic templates behaviors.

As for the SLNF, it is clear that the RMS decreases considerably as the TOA bandwidth keeps increasing, thus the timing precision of this pulsar at EFF would improve significantly with the use of the new 400-MHz bandwidth back-end. Another obvious phenomenon is that the SLNF fit for WSRT data failed with this pulsar, which we attribute to the extremely low S/N (with a mean S/N of ~ 20.46) of the observations. Low S/Ns of observations would lead to underestimated TOA uncertainties and extra outliers, especially at frequency-resolved timing where the S/N would be reduced with the decrease of TOA bandwidth. In addition, low S/N would also lead to many TOAs being removed by the outlier rejection scheme, more than 40% TOAs are removed at TOA bandwidth of 20 MHz or less.

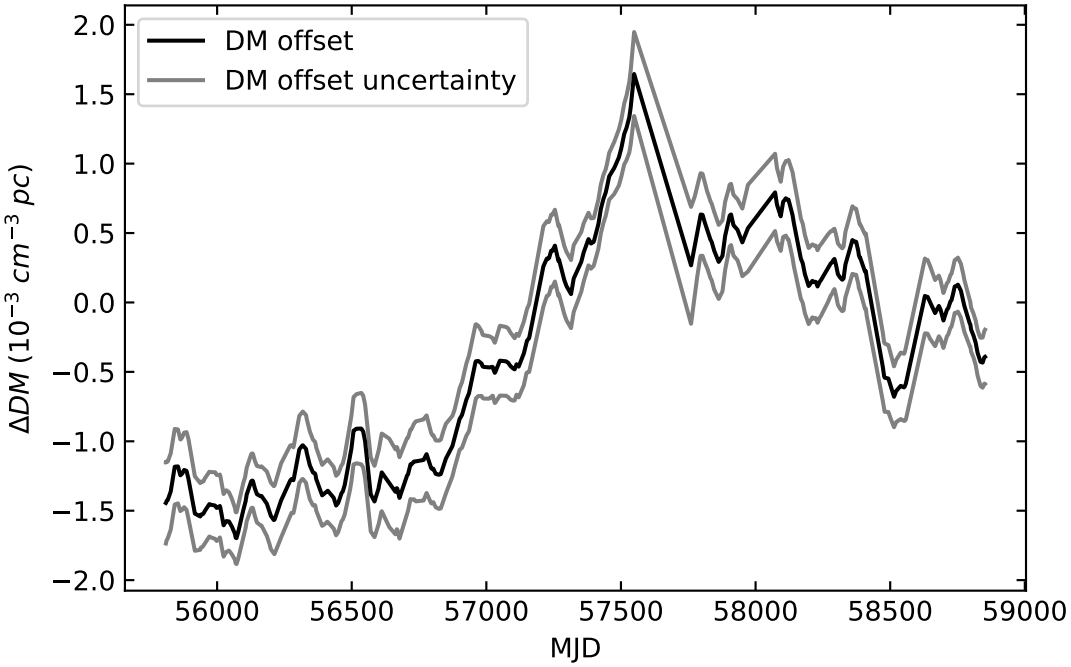

Figure 4.4 DM time series for PSR J1600−3053 that was obtained with NCY data, with a reference DM of 52.321 cm^{-3} pc.

4.3.5 PSR J1909−3744

With a spin-period of 2.95 ms in a 1.53-day binary system, PSR J1909−3744 is the fastest spinning MSP in our data set. Thanks to its extremely stable pulse profile and narrow peak with a small pulse duty cycle ($\sim 1.5\%$), this pulsar remains the most precisely timed pulsar for PTA purposes (Perera et al., 2019; Verbiest et al., 2016). However, due to its low declination, it is only observed by the NCY telescope within the EPTA. Using data from NCY, Liu et al. (2020) managed to achieve a timing precision of approximately 100 ns on a 15-year time scale. Shannon et al. (2014) and Lentati & Shannon (2015) demonstrated that this pulsar presents a surprisingly low level of jitter noise ($\sim$10 ns), which indicates enormous potential in improving the timing precision.

Due to the existence of achromatic red noise and DM noise components (Liu et al., 2020, and Chalumeau et al, in preparation), the original RMS and χ^2_r are as high as 0.241 ms and ~ 25 respectively. In this case, we adopted the red noise model determined in Liu et al. (2020) and the improvements of the timing solution are dramatic. From Figure 4.5, we can see that for this extremely precisely timed pulsar, we did not find any noticeable improvement after trying several combinations of templates and CCAs. In addition, we found that the

difference between the mean error bars is also negligible. With regard to the TOA bandwidth analysis, the noise fitting curve, as shown in Figure 4.6, fits the RMS as a function of TOA bandwidth perfectly. The fitting also indicates that increasing the TOA bandwidth of the NCY back-end alone would not significantly improve the timing precision. The SLNF we estimated for this pulsar is ~ 54 ns.

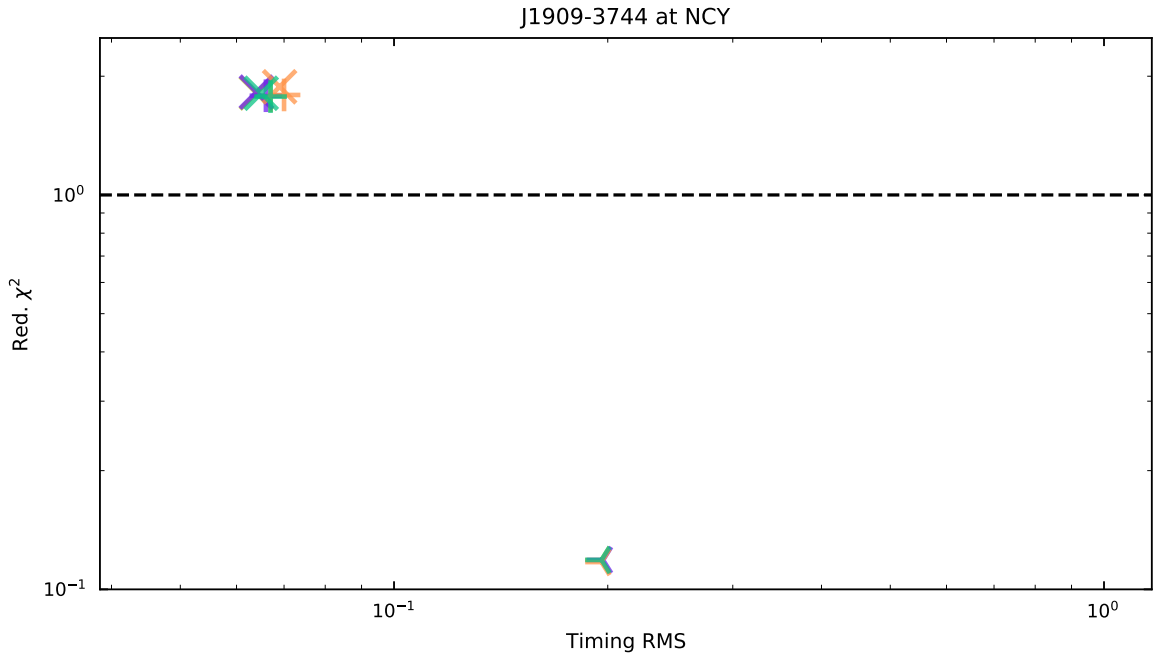

Figure 4.5 χ_r^2 and residual RMS for PSR J1909−3744 at NCY as a function of the selected CCA and template.

4.3.6 PSR J1918−0642

PSR J1918−0642, a 7.65-ms MSP in a 10.91-day binary system, was discovered by Edwards & Bailes (2001a) in an intermediate Galactic latitude survey. Janssen et al. (2010) studied this pulsar with 7.5-year EPTA observations and updated the timing model. One noticeable phenomenon they found is that the flux density of PSR J1918−0642 shows extensive modulation due to refractive and diffractive scintillation.

Desvignes et al. (2016) and Fonseca et al. (2016) revisited this pulsar with 12.5-year EPTA and NANOGrav 9-year data, respectively, and detected the Shapiro delay in this system.

With regard to our analysis of PSR J1918-0642, while results yielded from JBO data are in conformity with the conclusions of Chapter 3 (Wang et al., 2021), EFF, NCY and WSRT TOAs imply that while added templates combined with the FDM template-matching

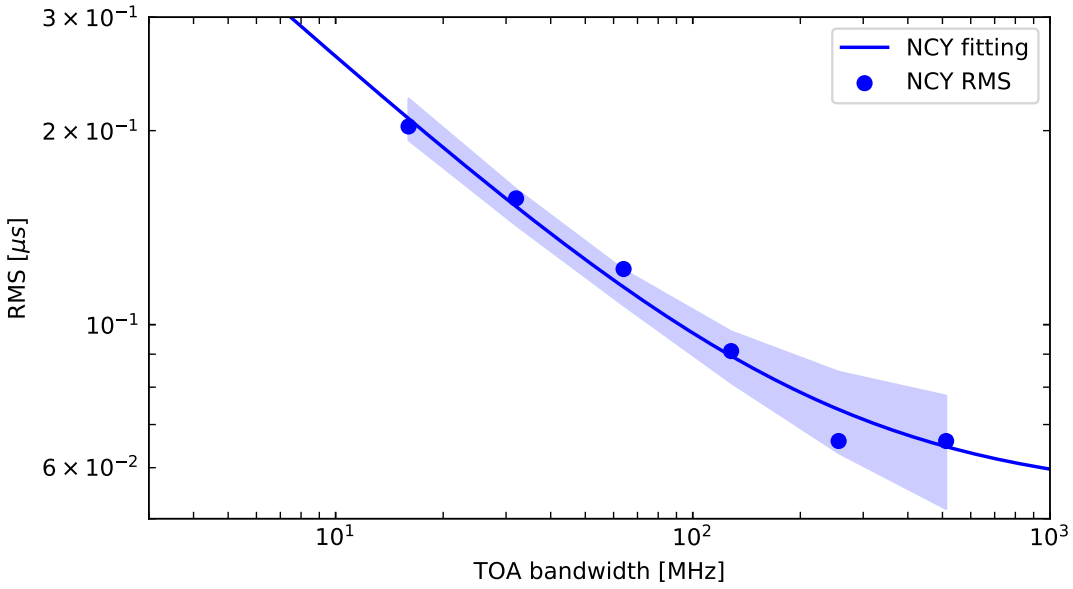

Figure 4.6 SLNF estimates for PSR J1909−3744.

method are consistent with smoothed and analytic templates, they all obtained around 10% higher RMS compared with PGS and added template combination. The most noticeable result shows up at WSRT, where PGS has a 15% lower RMS and χ^2_r.

4.3.7 Other Pulsars

The results from the remaining six pulsars in our data set are identical to the conclusions drawn in Chapter 3 (Wang et al., 2021). It is clear that the FDM algorithm is always superior to or competitive with other algorithms. The added, smoothed and analytic templates are comparable and typically preferred in high precision timing analysis. In some cases, such as PSR J0613−0200, the PGS method combined with added templates would yield a slightly lower RMS, but at the expense of increased χ^2_r. That is to say, for PSR J0613−0200, PGS tends to underestimate the TOA uncertainty. More clearly, PSRs J1640+2224 and J2317+1439 show that the added template combined with PGS cannot determine the TOAs and their uncertainties correctly as both RMS and χ^2_r values are noticeably higher than other possibilities.

For PSRs J1024−0719, J1744−1134 and J1857−0642, the results agree exactly with the results in Chapter 3 (Wang et al., 2021).

4.4 Conclusions

This work reports on the impact of template and CCA choice on timing precision. We targeted a large sample of EPTA pulsars and our investigations clearly show that the GIS method is not suitable for high precision timing at all. No matter which template was applied, GIS generally yielded fairly high levels of RMS. Also, it is noticeable that the GIS method would overestimate the TOA uncertainties, leading to over-fitted timing residuals. FDM is generally superior to the PGS algorithms, although some exceptions exist in our data, but they are typically either due to the limited number of TOAs (i.e. PSR J0030+0451 at WSRT and PSR J2010−0719 at EFF) or unreliable TOA uncertainties (e.g. PSRs J1640+2224 and J2317+1439). Based on the results presented above, we conclude that FDM should be used by default for high precision pulsar timing analysis.

With regard to the template, data-derived and smoothed templates are recommended. Although such templates are at the risk of 'self-standarding' as described by Hotan et al. (2005), we did not find any evidence in our templates for this issue. We noticed that in Hotan et al. (2005) the 'self-standarding' problem diminishes when the S/N is larger than 25. Since most of our observations have high S/N, it does not have a big impact on our investigation. In addition, with the increase of hardware upgrades and development of RFI mitigation algorithms, 'self-standarding' does not continue to be a big issue for PTA analysis. Therefore, we suggest that the added templates should be used by default for current and future PTA TOA determination.

If we group the templates and CCAs by telescope, a few conclusions are very easy to make. First of all, all the templates and CCAs work very stable with NCY data such that the RMS values or the χ^2_r values are all consistent and the differences can be neglected. In other words, it makes little difference on how we select a template or CCA for NCY data. JBO is similar with NCY, except that PGS combined with added templates is sometimes unstable, especially for PSRs J0030+0451 J1640+2224 and J2317+1439, which tend to have significantly high χ^2_r. Apart from the added template, analytic and smoothed templates are consistent on WSRT data. While PGS combined with added template tends to result in high χ^2_r on most pulsars, PSRs J0030+0451 and J1600−3053 have dramatic improvements of RMS with the added template. For EFF, the added template combined with FDM is preferred since they tend to yield either better RMS and χ^2_r or consistent results. However, there are two exceptions, PSRs J1744−1134 and J2010−1323, where smoothed and analytic templates have better and consistent timing results.

On the whole, we think that for the currently timed pulsars for the PTA purposes, template and CCA choices will have smaller impacts with the improvement of telescope sensitivity.

But for the moment, we should pay great attention to CCA and template selection, especially for telescopes with low sensitivity.

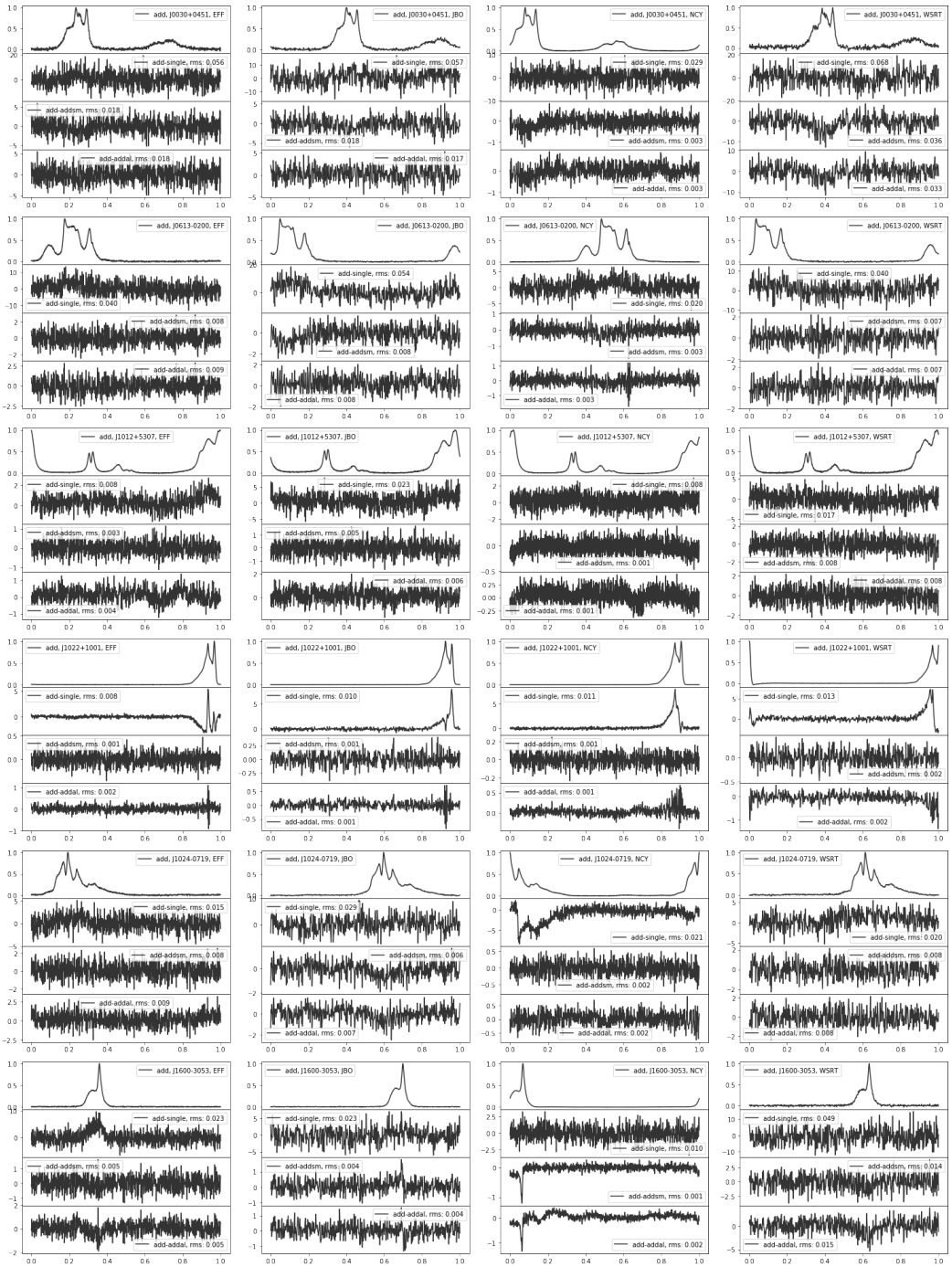

Figure 4.7 Pulsar profiles of the added templates and profile differences between added and single, analytic, smoothed templates. From top to bottom, PSRs J0030+0451, J0613−0200, J1012+5307, J1022+1001, J1600−3053 and J1024−0719. Within each subplot, the profile of each pulsar and the difference between added and single, smoothed and analytic templates are shown from top to bottom respectively. In each row, the EFF, JBO, NCY and WSRT are shown from left to right.

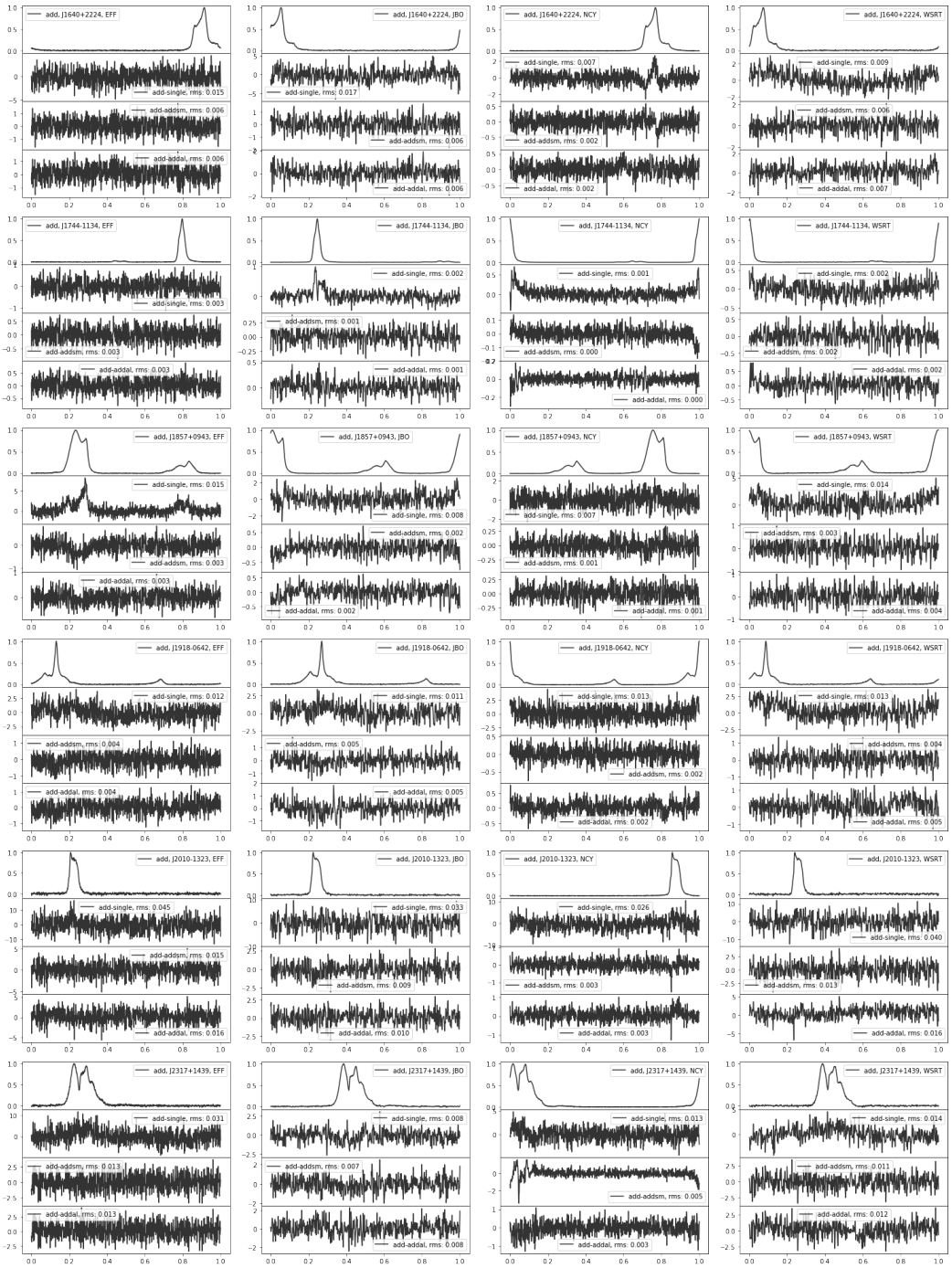

Figure 4.8 Pulsar profiles from added templates and profile differences between added, analytic and smoothed templates.

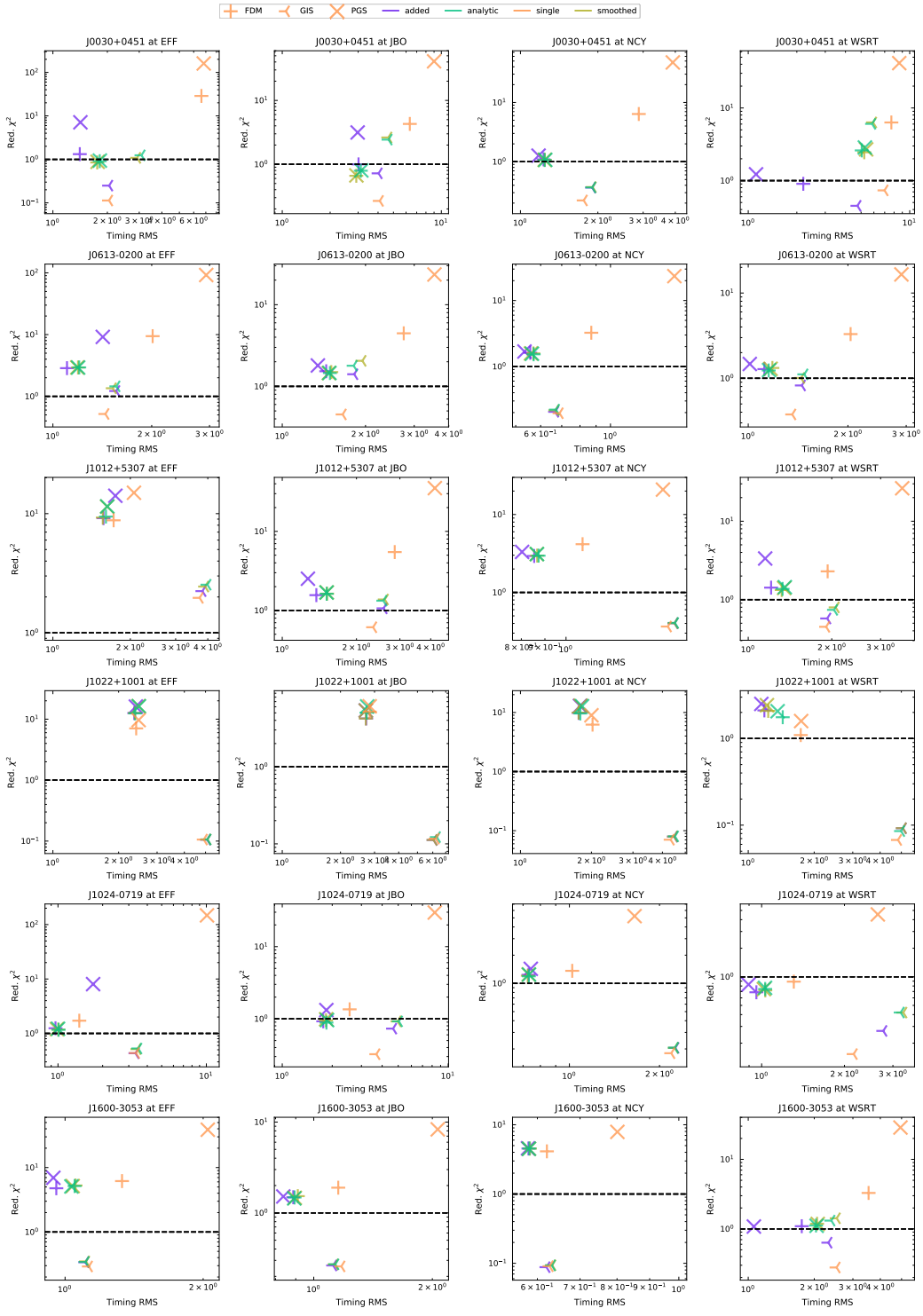

Figure 4.9 χ_r^2 and residual RMS for the three pulsars as a function of the selected CCA and template and the different telescopes.

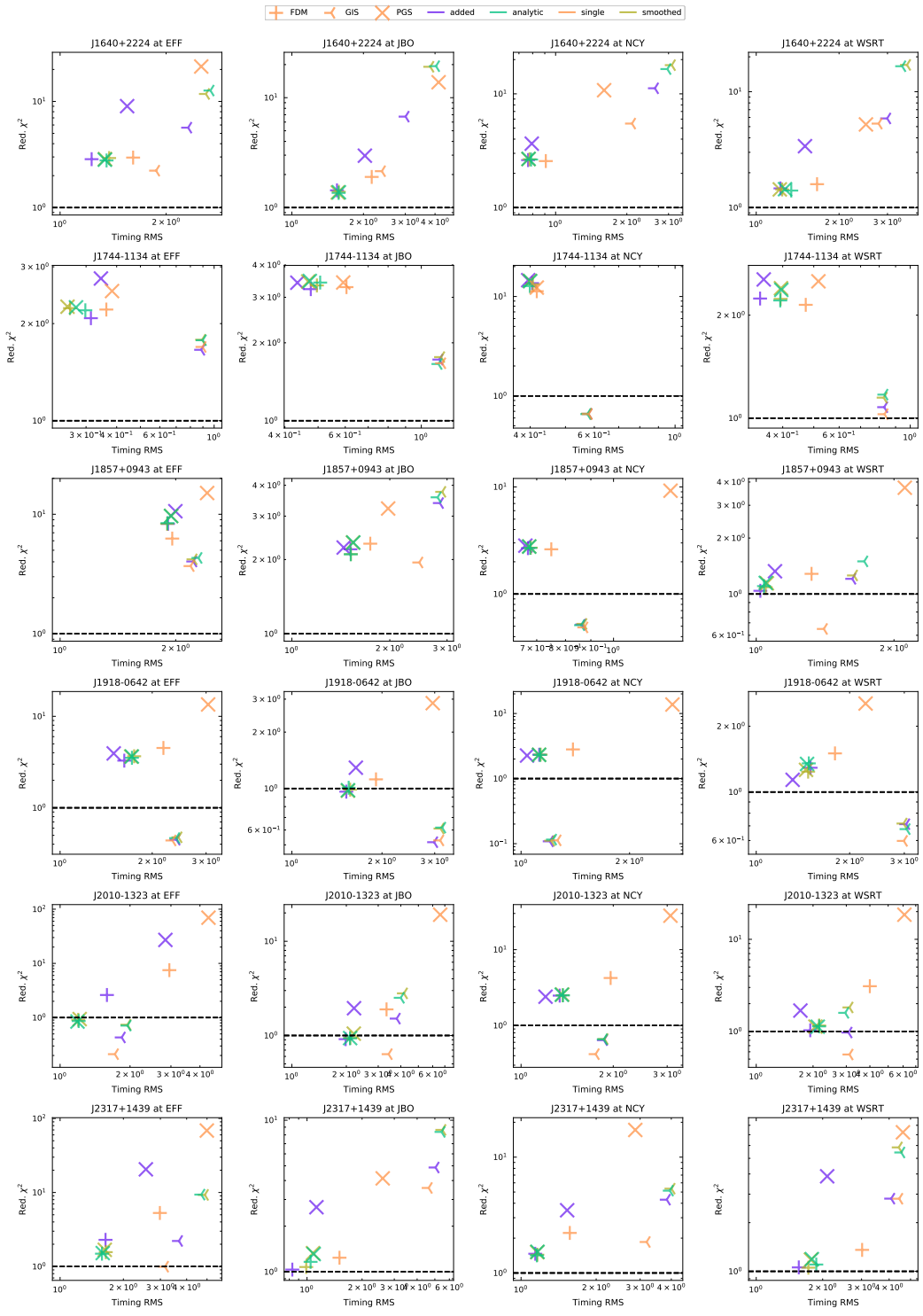

Figure 4.10 χ^2_r and residual RMS for the three pulsars as a function of the selected CCA and template and the different telescopes.

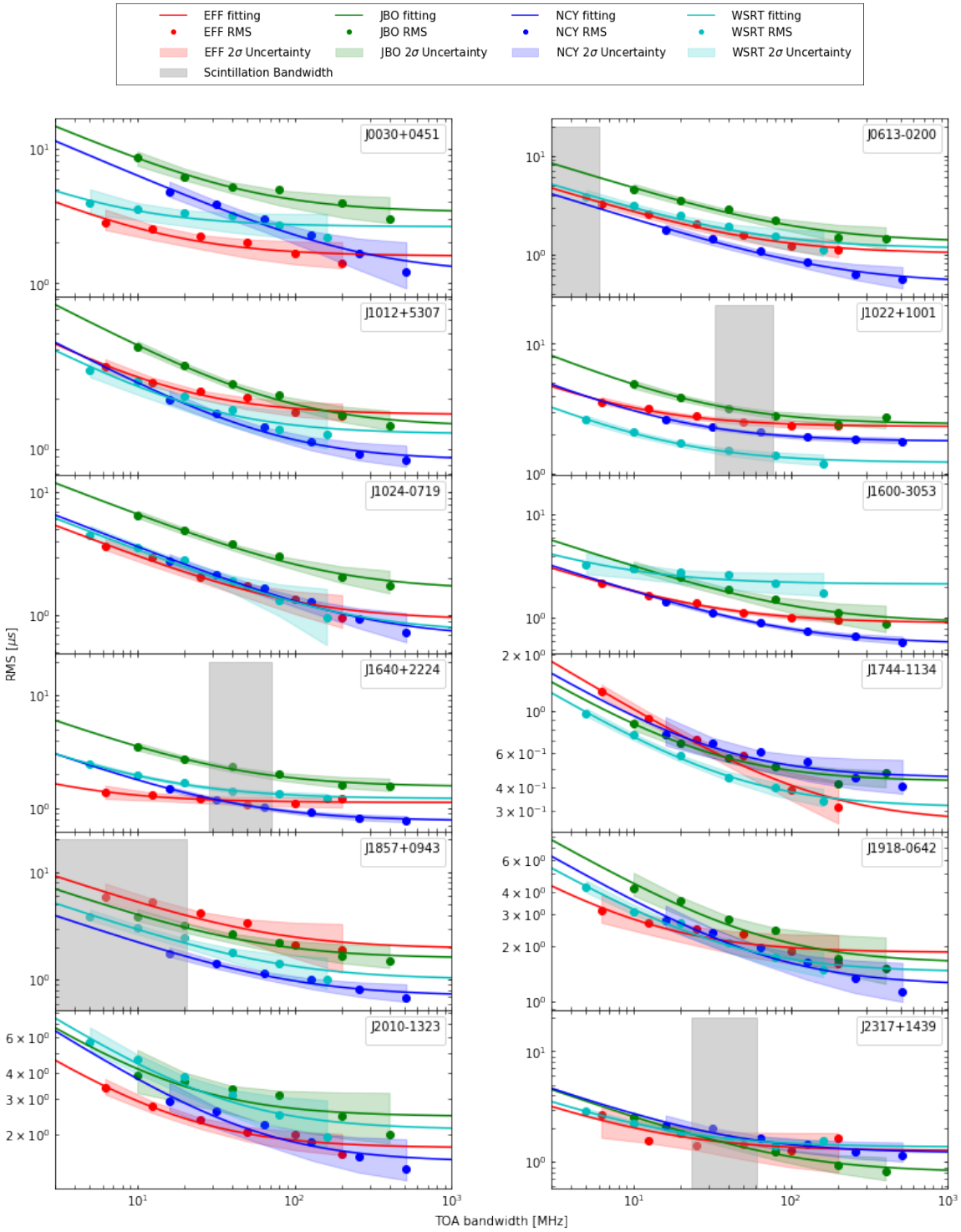

Figure 4.11 SLNF estimates for the 12 pulsars.

Chapter 5

Noise Analysis of Six Pulsars and a Limit on the Gravitational Wave Background

The direct detection of ultra-low frequency GWs utilizing PTAs approaches is a major application of MSPs. The first detection of GWs in the nano-Hertz regime will likely be an isotropic stochastic GWB created by the superposition of GWs from coalescing SMBHB mergers. In this chapter, I analyze the low-frequency noise of data on six selected pulsars obtained with the EPTA telescopes and compare our results with the finalized common-noise analysis carried out by the EPTA community.

5.1 Introduction

The 21st century astronomy belongs to multi-messenger observations (Kelley et al., 2019). Although EM observations have singularly dominated astronomy in the past centuries and yielded many achievements, ranging from the historical observations of constellations in the night sky, Lunar phases, Sun-spots and, the discovery of the outer belt gas giants and their moons to the modern era of mapping the heliosphere, the local bubble (Cox & Reynolds, 1987) and the galaxy, the cosmic microwave background (Penzias & Wilson, 1965), observations of gravitational lensing of EM radiation and even the discovery of pulsars (Hewish et al., 1968). However, some extreme objects, such as BHs, cannot be directly observed by EM observations since EM radiation cannot escape their gravitational fields, although secondary emission from regions very close to the BH can arise from a number of processes. Multi-messenger astronomy, which combines signals from EM radiation, GW emission, and cosmic particles (neutrinos and cosmic rays) allows us to observe these

super-dense and massive objects or the most violent and energetic events often associated with the formation or destruction of these objects simultaneously.

The newest of the observed messengers, GWs are disturbances in the curvature of space-time which could be generated by any accelerated masses, but due to the small associated amplitudes or large distances, only the radiation from massive stars and catastrophic events can be detected by us. As counterparts of the ground-based detectors (e.g. LIGO, Abbott et al., 2004) and space-based detectors (e.g. LISA, Gianolio et al., 2004), PTAs (Foster & Backer, 1990; Romani, 1989) are most sensitive to the low-frequency ($10^{-9} - 10^{-6}$ Hz) GW signals, thanks to their ultra-long 'arms' which are effectively the distances between pulsars and the Earth. PTAs utilize an array of the most stable MSPs (Alpar et al., 1982; Backer et al., 1982) to detect correlated signals in pulsar timing residuals (see Chapter 2). As they propagate through space-time, GWs will introduce a quadrupolar correlation in the timing residuals of the pulsars in the PTA that is distinct from noise induced by local clocks errors, improper polarization calibration, defective SSE, etc. (Verbiest et al., 2016). This quadrupolar signature, known as the "Hellings and Downs" curve, depends only on the sky angular separation between the pulsar pairs (Hellings & Downs, 1983).

Currently, there are three major PTA collaborations involved in low-frequency GW detection: the EPTA (Desvignes et al., 2016; Janssen et al., 2008), the PPTA (Manchester et al., 2013), and the NANOGrav (Demorest et al., 2013). These three PTAs also work together as the International PTA (IPTA, Perera et al., 2019; Verbiest et al., 2016) to maximize the sensitivity. More recently, the Indian PTA (InPTA, Joshi et al., 2018) joined the IPTA community in March 2021. In addition, a number of burgeoning communities, such as the Chinese PTA (CPTA, Lee, 2016), and the South African PTA are beginning to organize themselves.

It is generally accepted that the stochastic GWB, generated from the entire population of inspiraling SMBHBs, cosmic strings, and the primordial background relic (Saito & Yokoyama, 2009; Sanidas et al., 2012), is likely to provide the first detection (Ravi et al., 2015; Rosado et al., 2015). While no detection has been made yet, the PTAs are continuously towards developing increasingly sensitive algorithms and datasets. In a significant step forward, Lentati et al. (2013) laid out a model-independent Bayesian method to estimate the spectral properties of GWB. More recently, a hybrid frequentist-Bayesian statistic method has also been developed (Vigeland et al., 2018). Along with rapid algorithms and methods developments, PTAs have been able to place increasingly constraining upper limits on the GWB. The NANOGrav constraints on the stochastic GWB amplitude have evolved from 1.1×10^{-14} (Demorest et al., 2013) to 1.92×10^{-15} (95%) (Arzoumanian et al., 2020) for a fiducial $f^{-2/3}$ power-law spectrum. With 18 years of observations of six pulsars, the EPTA

constrain the upper limit of strain amplitude $A < 3.0 \times 10^{-15}$ at a spectral index of $13/3$ (Lentati et al., 2015), while the PPTA using a selected sample of its pulsars has been able to provide an upper limit on the strain amplitude of $A < 1.0 \times 10^{-15}$ (Shannon et al., 2015). A summary of the various limits is shown in Figure 5.1.

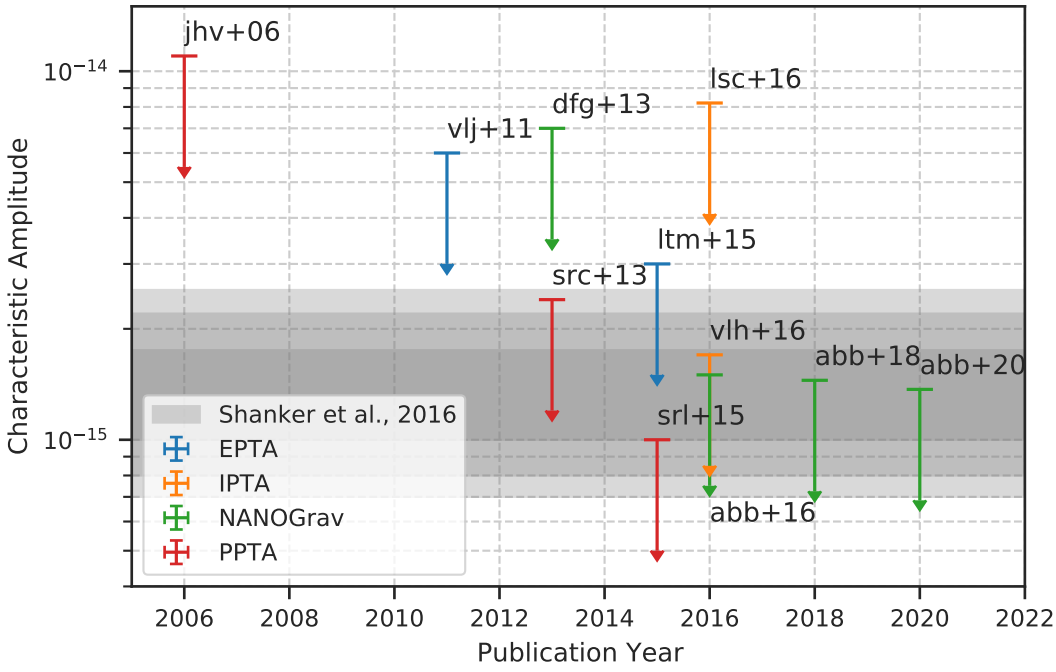

Figure 5.1 Summary of the different upper limits on the GWB from the different PTAs. The dash markers show the limits for the GWB from successive publications by the different PTAs, rescaled to a frequency of yr^{-1}, following (Sesana et al., 2016). The shaded regions shows the expected 1,2 and 3-σ likelihood ranges of the GWB from Shankar et al. (2016). The references are as follows: (jhv+06): Jenet et al. (2006), (vlj+11): van Haasteren et al. (2011), (dfg+13): Demorest et al. (2013), (src+13): Shannon et al. (2013), (ltm+15): Lentati et al. (2015), (srl+15): Shannon et al. (2015), (vlh+16): Verbiest et al. (2016), (abb+16): Arzoumanian et al. (2016), (abb+18): Arzoumanian et al. (2018a), (abb+20): Arzoumanian et al. (2020)

The primary aim of this chapter is to measure the impact of our improved data processing and TOA generation and selection methods on the pulsar timing data and quantify the improvement in the sensitivity to a possible GWB or other common signals. To this end, I select the same pulsars as those which appear in the forthcoming 6-pulsar dataset (The EPTA collaboration, in preparation). Using a very simple noise modeling approach for the individual pulsars, I test models for DM and red noise, as described in Section 5.4.

This chapter is organized as follows. Section 5.2 briefly interpret noise model, GWB model and Bayesian analysis method of PTA data. I detail the single pulsar analysis and common noise analysis methods in Section 5.3, after which, in Section 5.4, I present results of single pulsar analysis and common noise analysis and compared with EPTA dataset. I finally test the sensitivity of both datasets to any common signals, in Section 5.5.

5.2 Data Model and Analysis Method

The TOAs present in this chapter are determined with method described in Chapters 3 and 4. For this work, the TOAs determined with the added template along with the FDM algorithm are used. Depending on the telescope sensitivity, observations were frequency-averaged into sub-bands with bandwidths between 128 and 200 MHz. Therefore, for archives from EFF and WSRT, I averaged the pulses over the entire band, while for the broad-band JBO and NCY data, the averaging was performed to remain two and four sub-bands respectively.

5.2.1 Noise Model

The noise model used in this work is based on the model described in Lentati et al. (2015, and references therein), where the stochastic noise of pulse TOAs is assumed to be composed of two components: Uncorrelated noise (also referred to as white noise) and time-correlated noise (red noise). The former component is usually determined through cross-correlation of pulsar pulse profiles and a template. The template-fitting TOA uncertainties (also known as error bars, σ) are regarded as an estimate of white noise, however, the calculated uncertainties would usually underestimate the white noise level due to the existence of other white noise sources, such as the jitter noise and improper polarimetric calibration. In order to account for the neglected noise, two corrective white noise parameters are introduced in the noise model, namely EFAC, which is a multiplicative scale factor applied to the template-fitting uncertainties, and EQUAD, which adds uncertainties in quadrature. The revised TOA uncertainties, $\hat{\sigma}$ can be expressed as:

$$\hat{\sigma} = \sqrt{(\mathrm{EFAC} \cdot \sigma)^2 + \mathrm{EQUAD}^2}. \tag{5.1}$$

In addition to white noise, the timing residuals for each pulsar contain low-frequency red noise which can be roughly decomposed into two components: chromatic (frequency-dependent) such as DM variations, and achromatic (frequency-independent) red noise (RN) such as intrinsic pulsar spin noise and GW noise. The spin noise is thought to be associated with rotational irregularities of the pulsar itself while the DM-induced red noise is related to

changes of the electron density distribution in the ionized interstellar medium between the Earth and the pulsar. The DM noise model can be further split into two components, a long term process corresponding to the bulk changes in the IISM moving across the LOS, which I fit using a Gaussian process (GP) model, $\mathrm{DM_{GP}}$ and an annual component arising due to the effect of the motion of the LOS due to the Earth's orbital motion, $\mathrm{DM_{annual}}$ which I test for but do not find any support for in our data. Thus our total noise model can be represented as:

$$s = \mathrm{DM_{GP}} + \mathrm{RN} \tag{5.2}$$

5.2.2 Gravitational Wave Background Model

Sazhin (1978) and Detweiler (1979) first suggested that GWs can be detected through pulsar timing methods as GWs would induce an extra red noise in the timing residuals. The PTA concept was then put forward to separate and analyze this GW-induced noise (Foster & Backer, 1990). However, since the GW-induced noise is immersed in other sources of noise, e.g. spin noise and DM variations, characterizing and minimizing all other sources of noise, especially the spin noise in each pulsar is critical for a robust GW detection. In this section, I describe the spectral model of a GWB-induced stochastic noise process with a peculiar correlation between pulsar pairs (Hellings & Downs, 1983).

Generally, GWB sources can be described with a power-law characteristic strain spectrum $h_c(f)$, expressed as:

$$h_c(f) = A_{\mathrm{GWB}} \left(\frac{f}{\mathrm{yr}^{-1}} \right)^{\alpha}, \tag{5.3}$$

where A_{GWB} is a dimensionless strain amplitude at a GW characteristic frequency f of 1 yr^{-1}, α is the slope of the spectrum and it varies depending on the origin of the GWB. For a GWB composed of inspiraling SMBHBs, α is equal to -2/3 (Jaffe & Backer, 2003; Phinney, 2001). In addition, another quantity that is normally used to describe GWB sources is the GWB energy density Ω_{GWB}, which is described as:

$$\Omega_{\mathrm{GWB}} = \frac{2\pi^2}{3H_0^2} f^2 h_c^2(f), \tag{5.4}$$

where H_0 is the Hubble constant. Finally, the observed timing residuals due to the GWB are described by the one-sided power spectral density $S(f)$, as given by

$$S(f) = \frac{1}{12\pi^2 f^3} h_c^2(f) = \frac{A_{\mathrm{GWB}}^2}{12\pi^2} \left(\frac{f}{\mathrm{yr}^{-1}} \right)^{-\gamma} \mathrm{yr}^3, \tag{5.5}$$

where $\gamma = 3 - 2\alpha$, and for the spiraling SMBHBs model, $\gamma = 13/3$.

GW signals, which will appear as achromatic noise in the timing residuals, are a temporally-correlated stochastic process. Unlike other noise components that are either monopolar or bipolar or fully uncorrelated, the GW signal is the only quadrupolar signal we expect and thus can be separated through determination of the angular correlation between pulsar pairs (Hellings & Downs, 1983). To account for the red noise in the pulsar timing dataset, both the chromatic and achromatic processes are described with single power-law spectra as,

$$S_r(f) \propto A_r^2 f^{-\gamma_r}, \tag{5.6}$$

where A_r is the amplitude of the red noise and γ_r is the spectral index for the red noise. The parameters of both the chromatic and achromatic process can be estimated with a Bayesian inference method described in Section 5.2.3.

5.2.3 Bayesian Analysis of Pulsar Timing Array Data

McHugh et al. (1996) initially used a Bayesian technique to produce upper limits on the GWB with PSR B1855+09. Later, van Haasteren et al. (2009) developed a Bayesian algorithm to constrain the GWB amplitude and thus first placed a upper limit on A of 6×10^{-15} with PTA data (van Haasteren et al., 2011). In this work, I only selected Bayesian inference as a tool to determine the strength of the low-frequency noise. Given a set of data d, the posterior distribution for the model parameters is defined by Bayes theorem as

$$p(\theta|d,M) = \frac{p(\theta|M)p(d|\theta,M)}{p(d|M)}, \tag{5.7}$$

where $\theta = \{\theta_1, \theta_2, ...\theta_n\}$ is the set of parameters, M is the model, also known as the hypothesis. The term on the left-hand side is the posterior probability distribution of the parameters given the observed data and model, $p(d|M) \equiv Z$ is the Bayesian evidence, while $p(\theta|M) \equiv \pi(\theta)$ is the prior probability distribution (the initial hypothesis of the probability distribution) of the parameters and $p(d|\theta,M) \equiv L(\theta)$ is the likelihood (probability of the data provided by a given model).

When performing parameter estimation, the Bayesian evidence, Z, which is independent of the parameters θ, can be treated as a normalization constant and ignored. Therefore, the estimation of Bayesian inference can be directly obtained by sampling the unnormalized posterior distribution. Generally, a standard MCMC sampling algorithm is used to obtain random samples drawn from a posterior probability distribution.

However, in contrast to the parameter estimation process, the Bayesian evidence Z is crucial in the model selection process. Model selection is performed based on the evidence or Bayes factors of different models. The evidence, sometimes also referred to as the marginal likelihood, can be obtained by integrating over all possible parameters θ in the set of model M, as

$$Z = \int L(\theta)\pi(\theta)d^n\theta \tag{5.8}$$

where n is the dimensionality of the parameter space. In the case of two models, M_i and M_j for the observed data, model selection can be performed by computing the posterior odds, the ratio R of the two models' probabilities given the observed data:

$$R = \frac{p(M_i|d)}{p(M_j|d)} = \frac{p(d|M_i)}{p((d|M_j))}\frac{p(M_i)}{p(M_j)} = \frac{Z_i}{Z_j}\frac{p(M_i)}{p(M_j)} \tag{5.9}$$

where $p(M_i)$ and $p(M_j)$ are prior probabilities of the two models respectively, $\frac{p(d|M_i)}{p(d|M_j)} \equiv B$ is the Bayes factor between the models M_i and M_j, while $\frac{p(M_i)}{p(M_j)}$ is the a prior probability ratio.

5.3 Comparing Datasets within a Bayesian Pulsar Timing Array Analysis

In order to minimize the computational cost of the Bayesian analysis and remain consistent with the EPTA 6-pulsar analysis (EPTA et al. 2021, in preparation), I analyze the same "restricted dataset" of six best pulsars proposed in Babak et al. (2016). These pulsars, namely, PSRs J0613−0200, J1012+5307, J1600−3053, J1713+0747, J1744−1134 and J1909−3744, dominate the S/N and provide ∼90% of the total EPTA sensitivity to GWs (see Figure 4.1).

The data utilized for this work were generated as part of the sample of 16 pulsars analyzed for Chapters 3 & 4 and the details are presented there. The pulsar timing models are identical to those utilized for the EPTA 6-pulsar analysis, derived using the linear least squares marginalization routines of `Tempo2` (Edwards et al., 2006; Hobbs et al., 2006).

To compare the possible improvement, I use a portion of the dataset the appears in the forthcoming EPTA 6-pulsar analysis, by restricting it to the data from the same telescopes and back-ends as ours which I call the EPTA six-pulsar dataset for brevity. To make the comparison more uniform I restrict our dataset to have the same frequency resolution as the EPTA 6-pulsar analysis.

The main issue I address here is the possible improvement in the sensitivity to the GWB as a result of the improved processing introduced in chapters 3 & 4. However, it must be pointed out that in the case of a multivariate Bayesian analysis *model-selection* is a well-established technique (using Bayes factors, Bayesian evidences or odds ratios). However, there are no straight-forward, bias-free means to compare the performance of *different datasets* given a model. To enable a comparison, I therefore chose a restricted model for the single pulsar noise modeling, as well as for the search for a correlated signal in the 6-pulsar PTA formed from the chosen pulsars.

This implies that our model is chosen to be generic and somewhat sub-optimal and thus the overall sensitivity of our dataset might in fact be greater than the results presented below might imply. At the same time, more rigorous (and informed) single pulsar modeling would also improve the overall PTA sensitivity.

5.3.1 Single Pulsar Analysis & Searching for Common Signals

For the purposes of the single pulsar noise modeling, I marginalized analytically over the `Tempo2` derived timing model, following Lentati et al. (2015) and others. For each pulsar I included a single time-stationary red noise model and a DM power-law model, as described in Section 5.2.1, with both models fitted using 30 frequency bins. Although I also searched for annual DM variations (see e.g., Lam et al., 2016) in our single pulsar dataset, I are not able to find meaningful constraints on these terms and hence I leave out these terms from our final single pulsar noise models. For PSR J1713+0747, I also include a model for DM events as described below.

PSR J1713+0747 is one of the most precisely timed MSPs by all of the main PTA telescopes. However, this pulsar has shown significant discrete DM variations, known as DM events. DM events lead to a sudden discrete change in timing residual. So far, two DM events have been reported. The first event, which was detected by the PTA community (Demorest et al., 2013; Desvignes et al., 2016; Keith et al., 2013), started at approximately MJD 54750 and lasted more than 100 days before the DM reverted back to the prevent level. This period lies outside our dataset and thus I do not investigate it in this work. However, Lam et al. (2018) observed the second DM event that started from approximately MJD 57510. Since DM events are non-stationary, they cannot be accounted for by the long-term DM variation power-law spectrum. In order to model the second DM event, I thus add an exponentially recovering step change to account for it. This introduces three more parameters; the epoch at which the DM event started, the maximum change in the DM and the time required for the DM to recover to the pre-event level, modelled as an exponential recovery.

I performed the single pulsar analysis using the ENTERPRISE (Ellis et al., 2020) using the Parallel Tempering MCMC (PTMCMC) sampler (Ellis & van Haasteren, 2017).

For the search for common signals, I utilize the single pulsar noise models derived in the step above, using these as input values for a PTA analysis with ENTERPRISE. For this step I also utilize the hyper-model analysis (Hee et al., 2016) to compute the Bayes Factor, approximated via the Savage-Dickey density ratio (Dickey, 1971), to compare the evidence for a model with no spatial correlations with that for a model with a Hellings & Downs (1983) type correlation.

5.4 Results

In this section, I first present the results of the single pulsar noise analysis, which shows the amplitude and spectral index of both the chromatic and achromatic noise processes. The single pulsar noise models are then utilized in the search for common signals in the six-pulsar PTA.

Figure 5.2 presents a comparison of the one- and two-dimensional posterior distributions for models of red noise and DM variations. The blue histograms represent results obtained with the EPTA six-pulsar dataset while the green histograms show the results obtained with the reprocessed TOAs. The maximum likelihood values for the power-law DM and red-noise parameters for the individual pulsars are tabulated in Table 5.1.

I find that while the results are broadly consistent between the EPTA 6-pulsar dataset and our dataset, the reprocessed data typically lead to improved constraints on both the DM and red-noise models. The two-dimensional likelihood plots in Figure 5.2 furthermore demonstrate the significant reduction of correlation between DM and red-noise model parameters that the reprocessed data achieve. While improved ToA precision may be partly the cause of this, superior treatment of RFI or improved template-profile reliability may also have significant impacts on the ability of the data set to distinguish between chromatic and achromatic red noise. A full comparative analysis to identify the relative impact of the various measures in our reprocessing analysis would require substantial time and computational resources and is as such outside the scope of this thesis, but these results do demonstrate the overall impact on the reliability of red-noise modeling efforts.

For the DM event of PSR J1713+0747 identified by Lam et al. (2018), the reprocessed dataset yields an amplitude of $\log_{10}\mathrm{A} = -5.9^{+0.14}_{-0.07}$, a recovery timescale of $\log_{10}\tau = 1.4^{+0.2}_{-0.1}$, i.e., $\sim 25^{+14.69}_{-5.16}$ days and the start epoch to be $\sim$ 57510.63 MJD, respectively, although I am not able to constrain the start MJD (identified to be $\sim$57510 from Lam et al., 2018) of the event due to limited observations in our dataset around that date.

Pulsar	Dataset	DM_{gp} γ	DM_{gp} $\log_{10}$ A	RN γ	RN $\log_{10}$ A
J0613-0200	Reprocessed	$3.79^{+0.87}_{-0.61}$	$-13.24^{+0.17}_{-0.22}$	0.82	$-17.76^{+2.84}_{-0.21}$
	EPTA 6-psr	$3.20^{+2.22}_{-1.70}$	$-13.86^{+0.43}_{-1.98}$	3.16	-14.19
J1012+5307	Reprocessed	$4.48^{+1.19}_{-1.06}$	$-14.07^{+0.47}_{-0.43}$	$1.98^{+0.31}_{-0.61}$	$-12.93^{+0.06}_{-0.06}$
	EPTA 6-psr	4.74	$-14.55^{+0.71}_{-0.88}$	$0.89^{+0.35}_{-0.42}$	$-12.95^{+0.06}_{-0.05}$
J1600-3053	Reprocessed	$5.51^{+0.70}_{-0.43}$	$-12.54^{+0.08}_{-0.08}$	$5.22^{+0.41}_{-0.43}$	$-12.43^{+0.06}_{-0.07}$
	EPTA 6-psr	$2.85^{+0.39}_{-0.27}$	$-13.30^{+0.10}_{-0.10}$	$0.02^{+3.68}_{0.0}$	-13.54
J1713+0747	Reprocessed	$1.64^{+1.82}_{-0.34}$	-13.33	$0.02^{+0.62}_{0.0}$	$-13.50^{+0.27}_{-0.46}$
	EPTA 6-psr	$2.22^{+0.92}_{-0.77}$	$-13.74^{+0.17}_{-0.25}$	$1.32^{+1.53}_{-1.30}$	-13.82
J1744-1134	Reprocessed	$2.78^{+1.95}_{-0.65}$	-13.27	2.53	$-13.32^{+0.21}_{-0.70}$
	EPTA 6-psr	$0.59^{+0.85}_{-0.56}$	$-13.37^{+0.23}_{-0.29}$	0.35	-13.42
J1909-3744	Reprocessed	$1.90^{+0.27}_{-0.47}$	$-12.15^{+0.04}_{-0.05}$	$2.46^{+0.44}_{-0.39}$	$-13.09^{+0.07}_{-0.09}$
	EPTA 6-psr	2.06	-13.71	$0.29^{+2.60}_{-0.26}$	-13.91

Table 5.1 Summary of the DM and red-noise (RN) models derived from the EPTA six-pulsar and the reprocessed datasets. The numbers quoted above are the maximum likelihood values, with 1-σ errors. Numbers without error bars imply the posterior was not sufficiently constrained and only the peak value is supplied.

5.4.1 Gravitational Wave Analysis

The 1D marginalized common spectrum amplitude posterior with a fixed spectral index $\gamma = 13/3$, obtained from both our dataset and the EPTA dataset obtained from the six pulsars are shown in Figure 5.3.

I found that our noise analysis yields a clear detection of a common red noise signal with a power-law amplitude $A = 2.34^{+0.75}_{-1.32} \times 10^{-15}$ at fixed $\gamma = 13/3$. While for the EPTA TOAs, I only obtain an upper limit of $A = 2.26 \times 10^{-15}$ at a fixed $\gamma = 13/3$. Using the hyper-model analysis of Hee et al. (2016), I find that a model with a Hellings-Down correlated signal shows no significant preference over a model with no spatial correlations, with a Bayes factor of 1.06. I note that the EPTA six-pulsar dataset, when using the same models, returns a Bayes factor of 0.96, although with such small Bayes factors, any interpretation for or against these models is difficult. Our results are in general agreement with the NANOGrav result presented in Arzoumanian et al. (2020) which shows a common spectrum process with a

amplitude posterior of $1.92^{+0.75}_{-0.55} \times 10^{-15}$ with 90% confidence interval, based on a 12.5-year data set containing 45 pulsars. This red signal detected with our dataset indicates that using the optimal TOA creation method does significantly improve our sensitivity to common red noise.

Although our analysis of six pulsars shows clear evidence for a stochastic red signal, I cannot confirm whether this signal arises from GWs or other unmodeled origins. There are several potential sources of noise that are not isolated in this work, such as SSE errors and the SW. To disentangle this issue, further research of a larger sample of uniformly distributed pulsars with longer observational baselines would be needed.

5.5 Summary and Conclusion

In this work, I have analyzed a six-pulsar subset of the EPTA data set, obtained from the newest back-ends of four EPTA telescopes. Our timing results included optimized TOAs obtained with the approaches as described in the preceding chapters. In parallel with the EPTA six-pulsar analysis, I analyzed the same pulsars and determined the low-frequency noise in the data set obtained with only the newest-generation back-ends. I performed a Bayesian analysis of the low-frequency noise and DM variations with the ENTERPRISE package. In addition, I also compared our results for a common red noise process in all six pulsars' timing residuals. According to our work, I have a clear detection of red noise, but I cannot determine if it is due to the GWB or timing noise or even both. In the meantime, I noticed that the EPTA six-pulsar analysis also presents strong evidence for common red noise. With regard to the GWB detection, no measurement can be confirmed due to the limited number of pulsars. However, as the EPTA community is preparing for a larger dataset that would be composed of more than 20 pulsars with a time span of up to 25 years, the detection of the GWB would be possible in the coming years, especially if the optimization steps demonstrated in our work are included as part of the analysis.

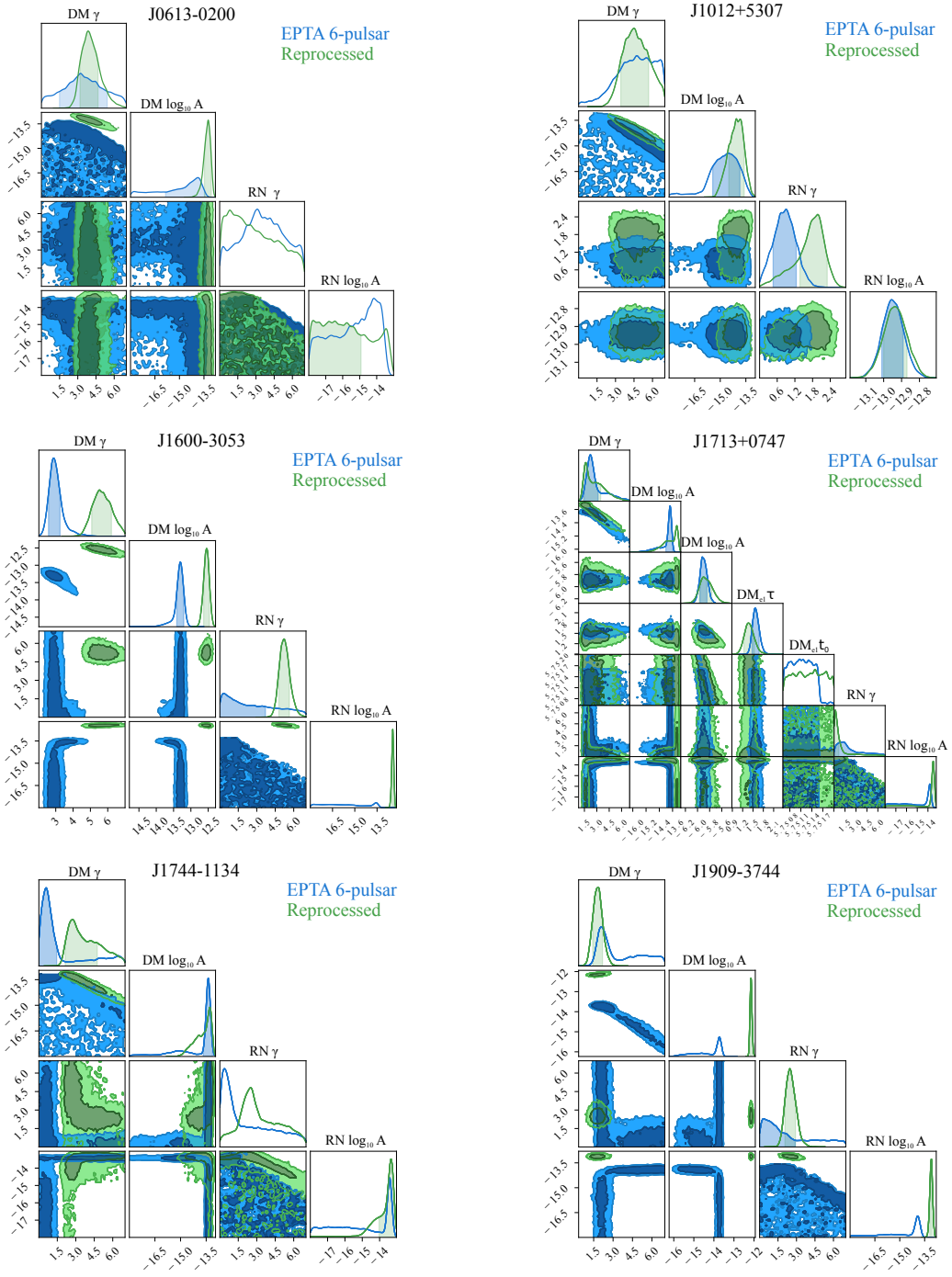

Figure 5.2 The comparison of one- and two-dimensional marginalized posterior distributions for the log-amplitude and spectral index of the power-law model for the red noise and DM variations for the six pulsars dataset observed with EPTA telescopes. Blue histograms indicate posterior distributions obtained with the EPTA six-pulsar dataset while the green histograms indicate the results obtained with TOAs derived in Chapter 4

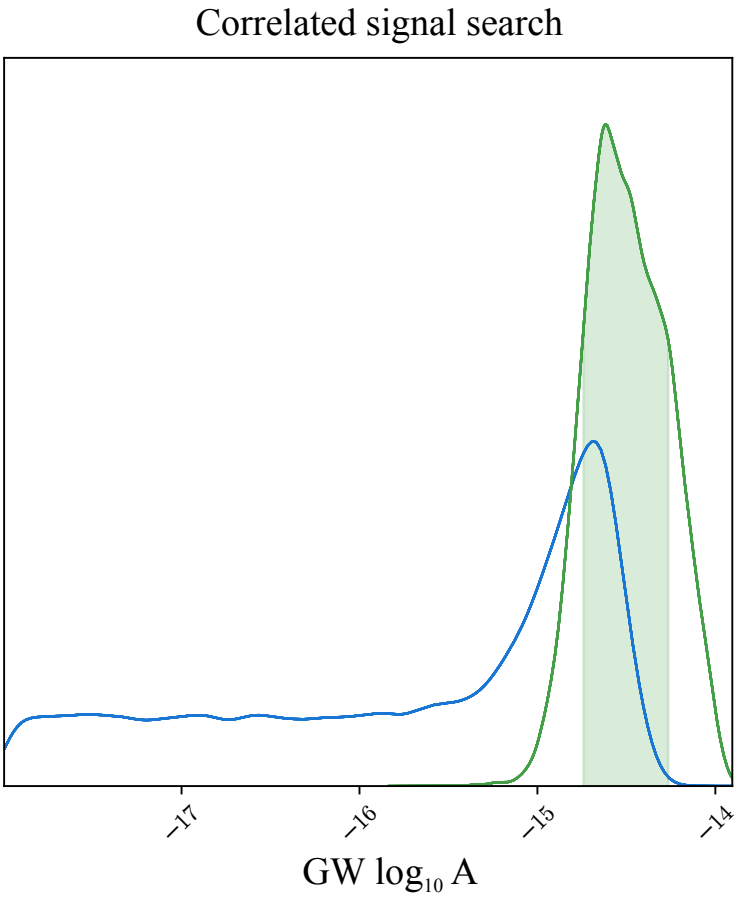

Figure 5.3 The one-dimensional marginalized Bayesian posteriors for the amplitude of a low-frequency spectral process with a fixed spectral index of $\gamma = 13/3$.

Chapter 6

Conclusions and Future Research

The discovery of pulsars and especially MSPs has enabled hybrid applications in astrophysics. One of the most anticipated goals related to pulsars is the detection of nano-Hertz GWs that mainly originate from coalescing SMBHBs. With this purpose, several PTAs that time an array of MSPs regularly, have been formed. High-precision pulsar timing can guarantee such a detection: theoretical calculations have shown that this detection can be made through the timing of $\sim$ 20 MSPs with timing precision at a level of $\sim$100 ns with regular cadence over time spans of five years to a decade (Jenet et al., 2005). However, up till now, only a few MSPs have achieved this precision. Although Siemens et al. (2013) conclude that increasing the number of pulsars in the array would be the best strategy while the cadence and the RMS of the pulsar timing residuals are less important under the current regime, it is still necessary to keep on improving the timing precision. Here are several reasons why I carry on investigating the improvement of the timing precision. First of all, expanding the number of regularly observed pulsars would present a huge challenge for the current telescopes' time allocation, especially for the newly added faint pulsars, which may require more integration time than usual. Secondly, expanding the array beyond the 20 pulsars or so as considered by Jenet et al. (2005), would imply adding much fainter (add consequently less precisely timed) pulsars, which would require timing precision improvements without a doubt. Third, Siemens et al. (2013) regard all pulsars as equal contributions to a GWB detection, but this is not realistic at all. The most precise pulsars usually provide the most significant contributions to the GWB detection sensitivity.

There are several directions to improve the timing precision of MSPs, such as hardware upgrades, noise mitigation, and algorithm optimization. The goal of this thesis is to investigate the influence on timing precision of templates, CCAs, and TOA bandwidth selection, leading to a standardized and unified timing process. Due to the fact that various templates, CCAs, and TOA bandwidths are adopted inconsistently by different researchers and PTAs, TOAs

obtained by different people can show significantly different results. This inconsistency could also have a significant influence on parameter estimation and searches for GWs. In this thesis, I mainly focus our analysis on comparison and investigation of templates and CCA selection. In addition, I also put forward a new method to investigate the system-limited noise floor and optimal TOA bandwidth. In this chapter, a brief summary of our most important conclusions from previous sections will be given below, followed by a discussion of promising future lines of research that follow from our work.

6.1 Summary

Generally, the precision of pulsar timing is quantified by the RMS of TOA residuals. Once the TOAs and their uncertainties are obtained, a least-squares fitting procedure is usually employed to estimate the timing-model parameters. To assess the quality of the fit and of the TOA uncertainties, the reduced chi-squared value, χ^2_r, is evaluated. Ideally the value of χ^2_r is close to unity, indicating a perfect match between the model and the observations at the precision predicted by the measurement uncertainties. However, the χ^2_r is often far from unity. A χ^2_r value lower than unity indicates the measurement uncertainties have been overestimated while a χ^2_r value larger than unity indicates the measurement uncertainties have underestimated the noise or that the timing model is incomplete or incorrect.

There could be several reasons why the χ^2_r value does not equal unity. For example the determination of the TOA uncertainties could be corrupted by the existence of jitter noise (Cordes & Shannon, 2010; Osłowski et al., 2011), or the timing model could be incomplete and lead to the existence of red noise (Coles et al., 2011; Lentati & Shannon, 2015). Both of these noise sources contribute to a high χ^2_r if they are not properly accounted for.

In this thesis, I mainly focus on the RMS and χ^2_r values of 16 MSPs (see Figure 6.1 for the distribution of the MSPs) based on analyses with the various templates and CCA combinations. In Chapter 2 of this thesis, I presented an overview of high-precision pulsar timing techniques. In addition, an outlier rejection scheme is presented to remove non-informative (noise-dominated) TOAs from our data in an objective and reproducible way.

In Chapter 3, I started the investigation of the impact of template and CCA selections and TOA bandwidth. Here I mainly compared four template possibilities, namely the single-brightest observation (referred to as single), all observations added template (added), added with smoothing template (smoothed), as well as the analytic profile (analytic), and three CCAs, namely, PGS, FDM, and GIS. As a practical demonstration, I apply our selected methods to EPTA data on the three test pulsars PSRs J0218+4232, J1713+0747, and J2145−0750. Based on our analysis of these three selected pulsars, I found the following:

- Data-derived and smoothed templates are typically preferred to more commonly applied alternatives (Section 3.3.1).
- The FDM template-matching algorithm is generally superior to, or competitive with, other algorithms (Section 3.3.2).
- The optimal TOA bandwidth is strongly dependent on pulsar brightness, telescope sensitivity and scintillation properties (Section 3.3.3).
- Generally significant averaging of TOAs across frequency is recommended (Section 3.4).

A further investigation and validation of the results are presented in Chapter 4. We performed a detailed analysis of thirteen MSPs from around ten years of EPTA observations. Based on this work, I refined the above-mentioned conclusions as follows:

- The added templates combined with the FDM template-matching method are usually superior to other possibilities (Section 4.3.7).
- For some extreme cases, such as extremely low S/N or too few TOAs, other combinations of template and CCA may work better (Section 4.3.1).
- The effect of pulse phase jitter noise is not a serious factor that influences the EPTA timing precision, since the jitter levels I derived are far smaller than the radiometer noise (Section 4.3.7).
- SLNF was shown to be above the jitter-noise level and was found to be significantly different between telescopes (Section 4.4).

Finally, I searched for red noise based on six pulsars in Chapter 5. I firstly performed a single-pulsar analysis with the Bayesian pipeline ENTERPRISE to obtain the stochastic noise parameters for each pulsar. Then I also investigated the common noise (i.e. a possible GWB) within our dataset. Our results show a clear detection of common red noise with a power-law amplitude $log_{10}A = 2.34^{+0.75}_{-1.32} \times 10^{-15}$ at fixed $\gamma = 13/3$. This result is a lot more constraining than the result obtained with the same data, analyzed according to the standard EPTA methodology. Also, our result is fully consistent and similarly constraining as the result published earlier by the NANOGrav collaboration (Arzoumanian et al., 2020) even though the number of pulsars is fewer and the length of the data set is substantially shorter in our case. I could not confirm whether the signal is from a GWB or not, since six pulsars are insufficient to constrain spatial correlations. I also showed noticeable improvement of our dataset compared with the EPTA work, particularly in terms of breaking correlations between chromatic and achromatic noise.

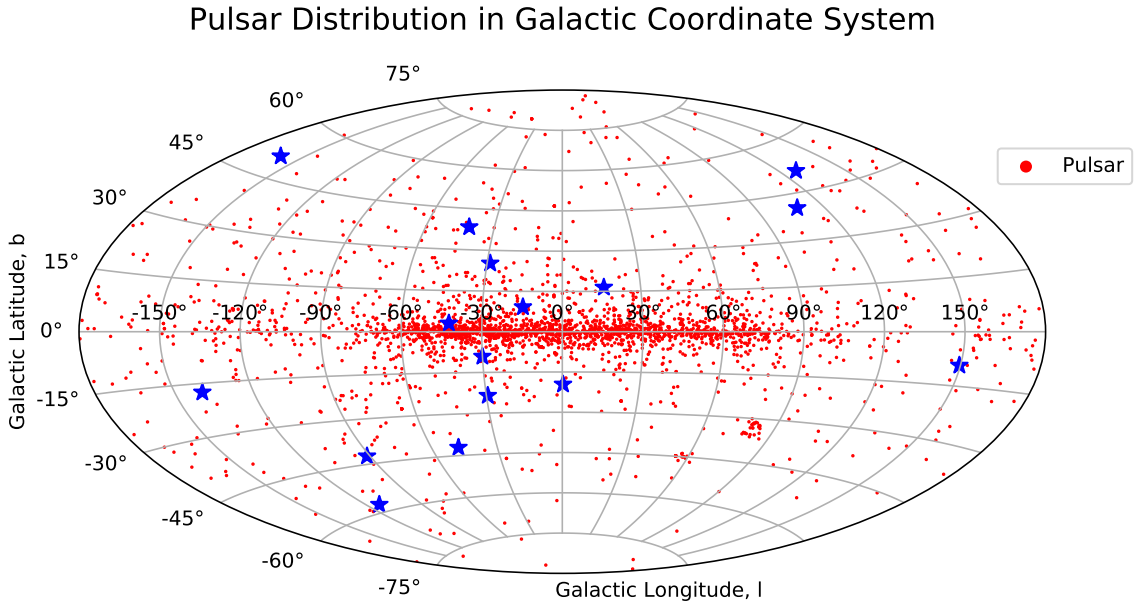

Figure 6.1 Pulsar distribution in the Galactic coordinate system in Aitoff projection. All known pulsars are presented with red dots, and the 16 pulsars investigated in this thesis are plotted with blue stars.

6.2 Further Work

Although the work presented in this thesis is comprehensive and complete, some additional aspects can be investigated to improve future timing precision. Increasingly, wide-band receivers are being built, allowing observations across much wider bandwidths than analyzed in this thesis. This makes it increasingly likely that the template-matching methods investigated in this thesis will be unable to adequately deal with profile evolution and DM changes properly or optimally. Here, while I managed to determine the impact of template and CCA selection on timing precision, I was unable to investigate the optimal strategies in dealing with such wide-band data, especially the 2D (frequency and phase) analytic template method (Liu et al., 2014; Pennucci et al., 2014a), which can be used to measure the pulse phase and also the DM simultaneously. I notice that the 2D template method will be necessary in future high-precision pulsar timing analysis. More work, such as investigating approaches to improving the accuracy of DM measurements, can be undertaken with the mentioned 2D template. The traditional method that determines TOAs through frequency-averaged pulse profiles ignores profile evolution. In addition, the data's frequency information would be lost when performing frequency averaging. The usage of 2D templates would not only mitigate the scintillation effects, but also simplify the timing procedures that are usually needed for describing the profile variation.

As is often the case, solving problems provokes further questions. Our TOA bandwidth analysis method provides another path to investigate the jitter noise. According to the system-limited noise floor analysis, I am unable to determine the optimal TOA bandwidth as well as the jitter noise in our dataset due to the interrelation between system-limited white noise, jitter noise, and EQUADs/ECORRs. However, our investigation shows that system-limited noise floors are clearly telescope-dependent, and the strength is noticeably higher than jitter noise derived with current models (e.g., Lam et al., 2019). These results indicate a hardware problem and need to be investigated in detail to fully capitalize upon their abilities. Several attempts have already started to work toward this direction. For example, Verbiest et al. (2016) derived EQUAD and ECORR values that were inconsistent with some of the jitter noise levels published (e.g., Lam et al., 2019; Shannon et al., 2014), indicating that the noise and TOAs correlation sources may be ill-defined or poorly understood. Here, this SLNF analysis provides one more piece of these problems: by now comparing different instruments from the same telescopes, or by testing different bandwidths or frequency bands, further insights may be gained. Simultaneous observations like those being undertaken during the LEAP runs could also play a key role in this work. A detailed and careful comparison of the single-telescope data from a wide-band LEAP-like system is bound to identify the differences between arrival times at different telescopes, which is our best hope yet to close

in on systematic variations in particular telescopes. In addition, closer investigations of polarization purity and profile consistencies between the different telescopes (particularly for simultaneous observations) could provide another powerful tool to assess inconsistencies caused by non-astronomical corrupting effects.

Finally, it would be possible to search for a GWB with our current dataset. Although it was predicted that GWs would be detected by PTAs as early as 2010, only upper limits have been made and no significant detection has been made yet. The detection of GWs requires high precision TOAs, with the TOAs obtained with the optimal TOA creation pipeline, it is more likely to yield more precise and better-constrained upper limits, and even a real detection.

6.3 Closing Remarks

It has been a great opportunity for me to work as a member of the EPTA, and make my contributions to pulsar astronomy. As pulsar timing precision improves along with the development of new techniques and algorithms, successful detection of nano-Hertz GWs will be realized in the foreseeable future. On that day, our knowledge and understanding of the Universe would be expanded significantly. In the 20th century, the utilization of the full frequency band of EM waves broadened our horizons considerably, so will the GWs in the 21st century. Compared to EM radiation, the information of the radiation source emitting the GW is not subject to various variations or turbulence when passing through the interstellar space, this is a qualitative difference. Through this new method of observing physical objects and phenomena, GWs will truly open a new window on the universe, greatly increase our understanding of the essence of the universe and understanding of time and space itself.

References

Abbott B., et al., 2004, Phys. Rev. D, 69, 122004

Abbott et al. 2016, Physical Review Letters, 116, 061102

Abdo A. A., et al., 2009, ApJ, 699, 1171

Acernese F., et al., 2015, Classical and Quantum Gravity, 32, 024001

Affeldt C., et al., 2014, Classical and Quantum Gravity, 31, 224002

Alam M. F., et al., 2021a, ApJS, 252, 4

Alam M. F., et al., 2021b, ApJS, 252, 5

Alpar M. A., Cheng A. F., Ruderman M. A., Shaham J., 1982, Nature, 300, 728

Amaro-Seoane P., et al., 2013, GW Notes, 6, 4

Ando M., TAMA Collaboration 2002, Classical and Quantum Gravity, 19, 1409

Archibald R., et al., 2016, ApJ, 819, L16

Armstrong J. W., Rickett B. J., Spangler S. R., 1995, ApJ, 443, 209

Arzoumanian Z., et al., 2014, ApJ, 794, 141

Arzoumanian Z., et al., 2015, ApJ, 813, 65

Arzoumanian Z., et al., 2016, ApJ, 821, 13

Arzoumanian Z., et al., 2018a, ApJS, 235, 37

Arzoumanian Z., et al., 2018b, ApJ, 859, 47

Arzoumanian Z., et al., 2020, ApJ, 905, L34

Baade W., Zwicky F., 1934, Phys. Rev., 45, 138

Babak S., et al., 2016, MNRAS, 455, 1665

Backer D. C., 1970, Nature, 228, 752

Backer D. C., Kulkarni S. R., Heiles C., Davis M. M., Goss W. M., 1982, Nature, 300, 615

Bailes M., 1988, A&A, 202, 109

Bailes M., et al., 1994, ApJ, 425, L41

Bailes M., et al., 1997, ApJ, 481, 386

Bassa C. G., et al., 2016, MNRAS, 456, 2196

Bates S. D., Lorimer D. R., Verbiest J. P. W., 2013, MNRAS, 431, 1352

Becker W., Trümper J., Lommen A. N., Backer D. C., 2000, ApJ, 545, 1015

Begelman M. C., Blandford R. D., Rees M. J., 1980, Nature, 287, 307

Bhadra A., 2002, J. Phys. G: Nucl. Part. Phys., 28, 397

Bhattacharya D., van den Heuvel E. P. J., 1991, Phys. Rep., 203, 1

Bildsten L., 1998, ApJ, 501, L89

Bilous A., et al., 2016, A&A, 591, A134

Blake G. M., 1970, Astrophysical Letters, 6, 201

Bochenek C. D., Ravi V., Belov K. V., Hallinan G., Kocz J., Kulkarni S. R., McKenna D. L., 2020, Nature, 587, 59

Boyle L. A., Buonanno A., 2008, Phys. Rev. D, 78, 043531

Burke-Spolaor S., et al., 2019, Astron. Astropys. Rev., 27, 5

CHIME/FRB Collaboration et al., 2020, Nature, 587, 54

Caballero R. N., et al., 2018, MNRAS, 481, 5501

Caldwell R. R., Battye R. A., Shellard E. P. S., 1996, Phys. Rev. D, 54, 7146

Callanan P. J., Garnavich P. M., Koester D., 1998, MNRAS, 298, 207

Camilo F., Nice D. J., Taylor J. H., 1993, ApJ, 412, L37

Camilo F., Nice D. J., Shrauner J. A., Taylor J. H., 1996, ApJ, 469, 819

Chakrabarty D., Morgan E. H., Muno M. P., Galloway D. K., Wijnands R., van der Klis M., Markwardt C. B., 2003, Nature, 424, 42

Chandrasekhar S., 1931, ApJ, 74, 81

Chen K., Ruderman M., 1993, ApJ, 402, 264

Cognard I., Theureau G., Guillemot L., Liu K., Lassus A., Desvignes G., 2013, in Cambresy L., Martins F., Nuss E., Palacios A., eds, SF2A-2013: Proceedings of the Annual meeting of the French Society of Astronomy and Astrophysics. pp 327–330

Coles W., Hobbs G., Champion D. J., Manchester R. N., Verbiest J. P. W., 2011, MNRAS, 418, 561

Cook G. B., Shapiro S. L., Teukolsky S. A., 1994, ApJ, 424, 823

Cordes J. M., 1993, in Phillips J. A., Thorsett S. E., Kulkarni S. R., eds, Planets around Pulsars. Astron. Soc. Pac. Conf. Ser. Vol. 36, pp 43–60

Cordes J. M., Downs G. S., 1985, ApJS, 59, 343

Cordes J. M., Lazio T. J. W., 2002, arXiv e-prints, pp astro–ph/0207156

Cordes J. M., Shannon R. M., 2010, arXiv e-prints, p. arXiv:1010.3785

Cox D. P., Reynolds R. J., 1987, Ann. Rev. Astr. Ap., 25, 303

Crossno J., Liu X., Ohki T. A., Kim P., Fong K. C., 2015, Applied Physics Letters, 106, 023121

Dai S., et al., 2015, MNRAS, 449, 3223

Damour T., Vilenkin A., 2005, Phys. Rev. D, 71, 063510

Demorest P. B., 2011, MNRAS, 416, 2821

Demorest P. B., Pennucci T., Ransom S. M., Roberts M. S. E., Hessels J. W. T., 2010, Nature, 467, 1081

Demorest P. B., et al., 2013, ApJ, 762, 94

Desvignes G., et al., 2016, MNRAS, 458, 3341

Detweiler S., 1979, ApJ, 234, 1100

Dicke R. H., 1946, Rev. Sci. Instrum., 17, 268

Dickey J. M., 1971, The Annals of Mathematical Statistics, 42, 204

Donner J. Y., et al., 2020, A&A, 644, A153

Drake F. D., Craft H. D., 1968, Nature, 220, 231

DuPlain R., Ransom S., Demorest P., Brand t P., Ford J., Shelton A. L., 2008, in Proc. SPIE. p. 70191D, doi:10.1117/12.790003

Duncan R. C., Thompson C., 1992, ApJ, 392, L9

Edwards R. T., Bailes M., 2001a, ApJ, 547, L37

Edwards R. T., Bailes M., 2001b, ApJ, 553, 801

Edwards R. T., Hobbs G. B., Manchester R. N., 2006, MNRAS, 372, 1549

Einstein A., 1916, Näherungsweise Integration der Feldgleichungen der Gravitation

Ellis J., van Haasteren R., 2017, jellis18/PTMCMCSampler: Official Release, doi:10.5281/zenodo.1037579, https://doi.org/10.5281/zenodo.1037579

Ellis J. A., Vallisneri M., Taylor S. R., Baker P. T., 2020, ENTERPRISE: Enhanced Numerical Toolbox Enabling a Robust PulsaR Inference SuitE, doi:10.5281/zenodo.4059815

Espinoza C. M., Lyne A., Kramer M., Manchester R. N., Kaspi V., 2011, ApJ, 741, L13

Faraday M., 1844, Experimental researches in electricity. R Taylor, London

Fermi E., 1926, Rendiconti Lincei, 145

Finn L. S., Lommen A. N., 2010, ApJ, 718, 1400

Fonseca E., et al., 2016, ApJ, 832, 167

Foster R. S., Backer D. C., 1990, ApJ, 361, 300

Foster R. S., Fairhead L., Backer D. C., 1991, ApJ, 378, 687

Foster R. S., Wolszczan A., Camilo F., 1993, ApJ, 410, L91

Foster R. S., Cadwell B. J., Wolszczan A., Anderson S. B., 1995, ApJ, 454, 826

Freire P. C. C., et al., 2012, MNRAS, 423, 3328

Fruchter A. S., Stinebring D. R., Taylor J. H., 1988, Nature, 333, 237

Gianolio A., Racca G., Jennrich O., Reinhard R., Danzmann K., Vitale S., 2004, ESA Bulletin, 119, 4

Gold T., 1968, Nature, 218, 731

Gould D. M., Lyne A. G., 1998, MNRAS, 301, 235

Grishchuk L. P., 2005, Phys. Uspekhi, pp 1235–1247

Gueroult R., Shi Y., Rax J.-M., Fisch N. J., 2019, Nature communications, 10, 1

Han J. L., Manchester R. N., Xu R. X., Qiao G. J., 1998, MNRAS, 300, 373

Hankins T. H., Rickett B. J., 1975, in Methods in Computational Physics Volume 14 — Radio Astronomy. Academic Press, New York, pp 55–129

Harry G. M., Fritschel P., Shaddock D. A., Folkner W., Phinney E. S., 2006, Classical and Quantum Gravity, 23, C01

Hee S., Handley W. J., Hobson M. P., Lasenby A. N., 2016, MNRAS, 455, 2461

Hellings R. W., Downs G. S., 1983, ApJ, 265, L39

Hessels J. W. T., Ransom S. M., Stairs I. H., Freire P. C. C., Kaspi V. M., Camilo F., 2006, Science, 311, 1901

Hewish A., Bell S. J., Pilkington J. D. H., Scott P. F., Collins R. A., 1968, Nature, 217, 709

Hobbs G. B., Edwards R. T., Manchester R. N., 2006, MNRAS, 369, 655

Hobbs G., et al., 2010, Class. Quant Grav., 27, 084013

Hobbs G., et al., 2012, MNRAS, 427, 2780

Hobbs G., et al., 2019, MNRAS, p. 2672

Hotan A. W., van Straten W., Manchester R. N., 2004a, PASA, 21, 302

Hotan A. W., Bailes M., Ord S. M., 2004b, MNRAS, 355, 941

Hotan A. W., Bailes M., Ord S. M., 2005, MNRAS, 362, 1267

Huber P. J., 1964, The Annals of Mathematical Statistics, 35, 73

Hulse R. A., Taylor J. H., 1975, ApJ, 195, L51

Jackson J. D., 1962, Classical Electrodynamics. Wiley

Jacoby B. A., Bailes M., van Kerkwijk M. H., Ord S., Hotan A., Kulkarni S. R., Anderson S. B., 2003, ApJ, 599, L99

Jacoby B. A., Bailes M., Ord S. M., Knight H. S., Hotan A. W., 2007, ApJ, 656, 408

Jaffe A. H., Backer D. C., 2003, ApJ, 583, 616

Janssen G. H., Stappers B. W., Kramer M., Purver M., Jessner A., Cognard I., 2008, in Bassa C., Wang Z., Cumming A., Kaspi V. M., eds, American Institute of Physics Conference Series Vol. 983, 40 Years of Pulsars: Millisecond Pulsars, Magnetars and More. pp 633–635

Janssen G. H., Stappers B. W., Bassa C. G., Cognard I., Kramer M., Theureau G., 2010, A&A, 514, A74+

Jenet F. A., Hobbs G. B., Lee K. J., Manchester R. N., 2005, ApJ, 625, L123

Jenet F. A., et al., 2006, ApJ, 653, 1571

Joshi B. C., Kramer M., Lyne A. G., McLaughlin M. A., Stairs I. H., 2004, in Camilo F., Gaensler B. M., eds, IAU Symposium. p. 319

Joshi B. C., et al., 2018, Journal of Astrophysics and Astronomy, 39, 51

Karuppusamy R., Stappers B., van Straten W., 2008, PASP, 120, 191

Kaspi V. M., Beloborodov A. M., 2017, Ann. Rev. Astr. Ap., 55, 261

Kaspi V., Helfand D., 2002, arXiv preprint astro-ph/0201183

Kawamura S., et al., 2011, Classical and Quantum Gravity, 28, 094011

Keith M. J., et al., 2013, MNRAS, 429, 2161

Kelley L., et al., 2019, BAAS, 51, 490

Kerr M., Reardon D. J., Hobbs G. e. a., 2020, PASA

Kim M., An H., 2019, Journal of Korean Astronomical Society, 52, 41

Knight H. S., Bailes M., Manchester R. N., Ord S. M., Jacoby B. A., 2006, ApJ, 640, 941

Kramer M., Wielebinski R., Jessner A., Gil J. A., Seiradakis J. H., 1994, A&AS, 107, 515

Kramer M., Xilouris K. M., Lorimer D. R., Doroshenko O., Jessner A., Wielebinski R., Wolszczan A., Camilo F., 1998, ApJ, 501, 270

Kramer M., Xilouris K. M., Camilo F., Nice D., Lange C., Backer D. C., Doroshenko O., 1999, ApJ, 520, 324

Kramer M., Lyne A. G., O'Brien J. T., Jordan C. A., Lorimer D. R., 2006a, Science, 312, 549

Kramer M., et al., 2006b, Science, 314, 97

Kurosawa N., Kobayashi H., Maruyama K., Sugawara H., Kobayashi K., 2001, IEEE Transactions on Circuits and Systems I: Fundamental Theory and Applications, 48, 261

LIGO Collaboration L. S., et al., 2015, Class Quantum Grav, 32, 074001

Lam M. T., et al., 2016, ApJ, 819, 155

Lam M. T., et al., 2018, ApJ, 861, 132

Lam M. T., et al., 2019, ApJ, 872, 193

Lange C., Camilo F., Wex N., Kramer M., Backer D., Lyne A., Doroshenko O., 2001, MNRAS, 326, 274

Large M. I., Vaughan A. E., Mills B. Y., 1968, Nature, 220, 340

Lattimer J. M., Prakash M., 2001, ApJ, 550, 426

Lattimer J. M., Prakash M., 2007, Phys. Rep., 442, 109,165

Lazaridis K., et al., 2009, MNRAS, 400, 805

Lazarus P., Karuppusamy R., Graikou E., Caballero R. N., Champion D. J., Lee K. J., Verbiest J. P. W., Kramer M., 2016, MNRAS, 458, 868

Lee K. J., 2016, in Qain L., Li D., eds, Astronomical Society of the Pacific Conference Series Vol. 502, Frontiers in Radio Astronomy and FAST Early Sciences Symposium 2015. p. 19

Lee L. C., Jokipii J. R., 1975, ApJ, 201, 532

Lee L. C., Jokipii J. R., 1976, ApJ, 206, 735

Lentati L., Shannon R. M., 2015, MNRAS, 454, 1058

Lentati L., Alexander P., Hobson M. P., Taylor S., Gair J., Balan S. T., van Haasteren R., 2013, Phys. Rev. D, 87, 104021

Lentati L., et al., 2015, MNRAS, 453, 2576

Lentati L., et al., 2016, MNRAS, 458, 2161

Levin L., et al., 2016, ApJ, 818, 166

Liu K., Keane E. F., Lee K. J., Kramer M., Cordes J. M., Purver M. B., 2012, MNRAS, 420, 361

Liu K., et al., 2014, MNRAS, 443, 3752

Liu K., et al., 2015, MNRAS, 449, 1158

Liu K., et al., 2020, MNRAS, 499, 2276

Lommen A. N., Zepka A., Backer D. C., McLaughlin M., Cordes J. M., Arzoumanian Z., Xilouris K., 2000, ApJ, 545, 1007

Lorimer D. R., Kramer M., 2005, Handbook of Pulsar Astronomy. Cambridge University Press

Lorimer D. R., Yates J. A., Lyne A. G., Gould D. M., 1995a, MNRAS, 273, 411

Lorimer D. R., et al., 1995b, ApJ, 439, 933

Lorimer D. R., Bailes M., McLaughlin M. A., Narkevic D. J., Crawford F., 2007, Science, 318, 777

Lower M. E., et al., 2020, MNRAS, 494, 228

Luo J., et al., 2016, Classical and Quantum Gravity, 33, 035010

Lyne A. G., Pritchard R. S., Smith F. G., 1988, MNRAS, 233, 667

Lyne A., Hobbs G., Kramer M., Stairs I., Stappers B., 2010, Science, 329, 408

Lyne A., Jordan C., Graham-Smith F., Espinoza C., Stappers B., Weltevrede P., 2015, MNRAS, 446, 857

Lyubarsky Y., Kirk J. G., 2001, ApJ, 547, 437

Madison D., et al., 2019, The Astrophysical Journal, 872, 150

Manchester R. N., Hobbs G. B., Teoh A., Hobbs M., 2005, AJ, 129, 1993

Manchester R. N., et al., 2013, PASA, 30, 17

Maxwell J. C., 1865, Philosophical transactions of the Royal Society of London, pp 459–512

McHugh M. P., Zalamansky G., Vernotte F., Lantz E., 1996, Phys. Rev. D, 54, 5993

McLaughlin M. A., et al., 2006, Nature, 439, 817

Miller M. C., Miller J. M., 2015, Phys. Rep., 548, 1

Misner C. W., Thorne K. S., Wheeler J. A., 1973, Gravitation. W. H. Freeman, San Francisco

Moore C. J., Cole R. H., Berry C. P. L., 2015, Classical and Quantum Gravity, 32, 015014

Morello V., et al., 2019, MNRAS, 483, 3673

Navarro J., de Bruyn G., Frail D., Kulkarni S. R., Lyne A. G., 1995, ApJ, 455, L55

Nicastro L., Lyne A. G., Lorimer D. R., Harrison P. A., Bailes M., Skidmore B. D., 1995, MNRAS, 273, L68

Nita G. M., Gary D. E., Liu Z., Hurford G. J., White S. M., 2007, PASP, 119, 805

Nyquist H., 1928, Phys. Rev., 32, 110

Oppenheimer J. R., Volkoff G., 1939, Phys. Rev., 55, 374

Ord S. M., Jacoby B. A., Hotan A. W., Bailes M., 2006, MNRAS, 371, 337

Osłowski S., van Straten W., Hobbs G. B., Bailes M., Demorest P., 2011, MNRAS, 418, 1258

Ostriker J. P., 1968, Nature, 217, 1227

Ott C. D., Burrows A., Dessart L., Livne E., 2006, Phys. Rev. Lett., 96, 201102

Pacini F., 1967, Nature, 216, 567

Palmer J., Davenhall A. C., 2001, Starlink Cookbook, 6

Patruno A., Haskell B., Andersson N., 2017, ApJ, 850, 106

Pauli W., 1925, Zeitschrift fur Physik, 31, 765

Pennucci T. T., Demorest P. B., Ransom S. M., 2014a, ApJ, 790, 93

Pennucci T. T., Demorest P. B., Ransom S. M., 2014b, ApJ, 790, 93

Penzias A. A., Wilson R. W., 1965, ApJ, 142, 419

Perera B. B. P., et al., 2019, MNRAS, 490, 4666

Petroff E., Keith M., Johnston S., van Straten W., Shannon R., 2013, MNRAS, 435, 1610

Phinney E. S., 2001, arXiv e-prints, pp astro–ph/0108028

Pilkington J. D. H., Hewish A., Bell S. J., Cole T. W., 1968, Nature, 218, 126

Prialnik D., 2000, An Introduction to the Theory of Stellar Structure and Evolution. Cambridge University Press

Radhakrishnan V., Srinivasan G., 1981, in Hidayat B., Feast M. W., eds, Proc. 2nd Asian–Pacific Regional Meeting of the IAU. Tira Pustaka, Jakarta, pp 423–432

Ramachandran R., Kramer M., 2003, A&A, 407, 1085

Ravi V., Wyithe J. S. B., Shannon R. M., Hobbs G., 2015, MNRAS, 447, 2772

Reardon D. J., et al., 2016, MNRAS, 455, 1751

Rickett B. J., 1977, Ann. Rev. Astr. Ap., 15, 479

Romani R. W., 1989, in Ögelman H., van den Heuvel E. P. J., eds, Timing Neutron Stars. Kluwer, Dordrecht, p. 113

Rosado P. A., Sesana A., Gair J., 2015, MNRAS, 451, 2417

Russell H. N., 1931, MNRAS, 91, 951

Saito R., Yokoyama J., 2009, Phys. Rev. Lett., 102, 161101

Sallmen S., Backer D. C., Hankins T. H., Moffett D., Lundgren S., 1999, ApJ, 517, 460

Salmona A., 1967, Phys. Rev., 154, 1218

Sanidas S. A., Battye R. A., Stappers B. W., 2012, Phys. Rev. D, 85, 122003

Saslaw W. C., Faulkner J., Strittmatter P. A., 1968, Nature, 217, 1222

Sazhin M. V., 1978, Sov. Astron., 22, 36

Scheuer P. A. G., 1968, Nature, 218, 920

Schnitzeler D., 2012, MNRAS, 427, 664

Segelstein D. J., Rawley L. A., Stinebring D. R., Fruchter A. S., Taylor J. H., 1986, Nature, 322, 714

Sesana A., Shankar F., Bernardi M., Sheth R. K., 2016, Monthly Notices of the Royal Astronomical Society: Letters, 463, L6

Shankar F., et al., 2016, Monthly Notices of the Royal Astronomical Society, 460, 3119

Shannon C. E., 1949, "Proc. I. E. E. E.", 37, 10

Shannon R. M., Cordes J. M., 2012, ApJ, 761, 64

Shannon R. M., et al., 2013, Science, 342, 334

Shannon R. M., et al., 2014, MNRAS, 443, 1463

Shannon R. M., et al., 2015, Science, 349, 1522

Shapiro I. I., 1964, Phys. Rev. Lett., 13, 789

Shibazaki N., Murakami T., Shaham J., Nomoto K., 1989, Nature, 342, 656

Sieber W., 1973, A&A, 28, 237

Siemens X., Ellis J., Jenet F., Romano J. D., 2013, Class. Quant Grav., 30, 224015

Staelin D. H., Reifenstein III E. C., 1968, Science, 162, 1481

Stairs I. H., Thorsett S. E., Camilo F., 1999, ApJS, 123, 627

Stappers B. W., Kramer M., Lyne A. G., D'Amico N., Jessner A., 2006, Chin. J. Astron. Astrophys., 6, 298

Tauris T. M., Takens T. M., 1998, A&A, 330, 1047

Taylor J. H., 1990, in Backer D. C., ed., Impact of Pulsar Timing on Relativity and Cosmology. Center for Particle Astrophysics, Berkeley, p. m1

Taylor J. H., 1992, Philos. Trans. Roy. Soc. London A, 341, 117

Taylor J. H., Weisberg J. M., 1982, ApJ, 253, 908

Taylor J. H., Weisberg J. M., 1989, ApJ, 345, 434

Tiburzi C., 2018, PASA, 35, e013

Tiburzi C., et al., 2016, MNRAS, 455, 4339

Tiburzi C., et al., 2019, MNRAS, 487, 394

Tiburzi C., et al., 2021, A&A, 647, A84

Tiuri M. E., 1964, IEEE Transactions on Antennas and Propagation, 12, 930

Tolman R. C., 1939, Physical Review, 55, 364

Tukey J. W., 1977, Exploratory data analysis. Reading, MA

Verbiest J. P. W., Shaifullah G., 2018, Classical and Quantum Gravity, 35

Verbiest J. P. W., et al., 2008, ApJ, 679, 675

Verbiest J. P. W., et al., 2009, MNRAS, 400, 951

Verbiest J. P. W., et al., 2016, MNRAS, 458, 1267

Vigeland S. J., Islo K., Taylor S. R., Ellis J. A., 2018, Phys. Rev. D, 98, 044003

Wang N., Manchester R. N., Johnston S., 2007, MNRAS, 377, 1383

Wang Y., Keith M. J., Stappers B., Zheng W., 2017, MNRAS, 468, 2637

Weisberg J. M., Nice D. J., Taylor J. H., 2010, ApJ, 722, 1030

Yao J. M., Manchester R. N., Wang N., 2017, ApJ, 835, 29

You X.-P., et al., 2007a, MNRAS, 378, 493

You X. P., Hobbs G. B., Coles W. A., Manchester R. N., Han J. L., 2007b, ApJ, 671, 907

Zhang B., 2020, Nature, 587, 45

Zhu W. W., et al., 2015, ApJ, 809, 41

van Haasteren R., Levin Y., McDonald P., Lu T., 2009, MNRAS, 395, 1005

van Haasteren R., et al., 2011, MNRAS, 414, 3117

van Kerkwijk M. H., Bergeron P., Kulkarni S. R., 1996, ApJ, 467, L89

van Straten W., 2006, ApJ, 642, 1004

van Straten W., 2013, ApJS, 204, 13

van Straten W., Bailes M., 2011, PASA, 28, 1

van Straten W., Demorest P., Oslowski S., 2012, Astronomical Research and Technology, 9, 237

Appendix A

Pulsar Profiles

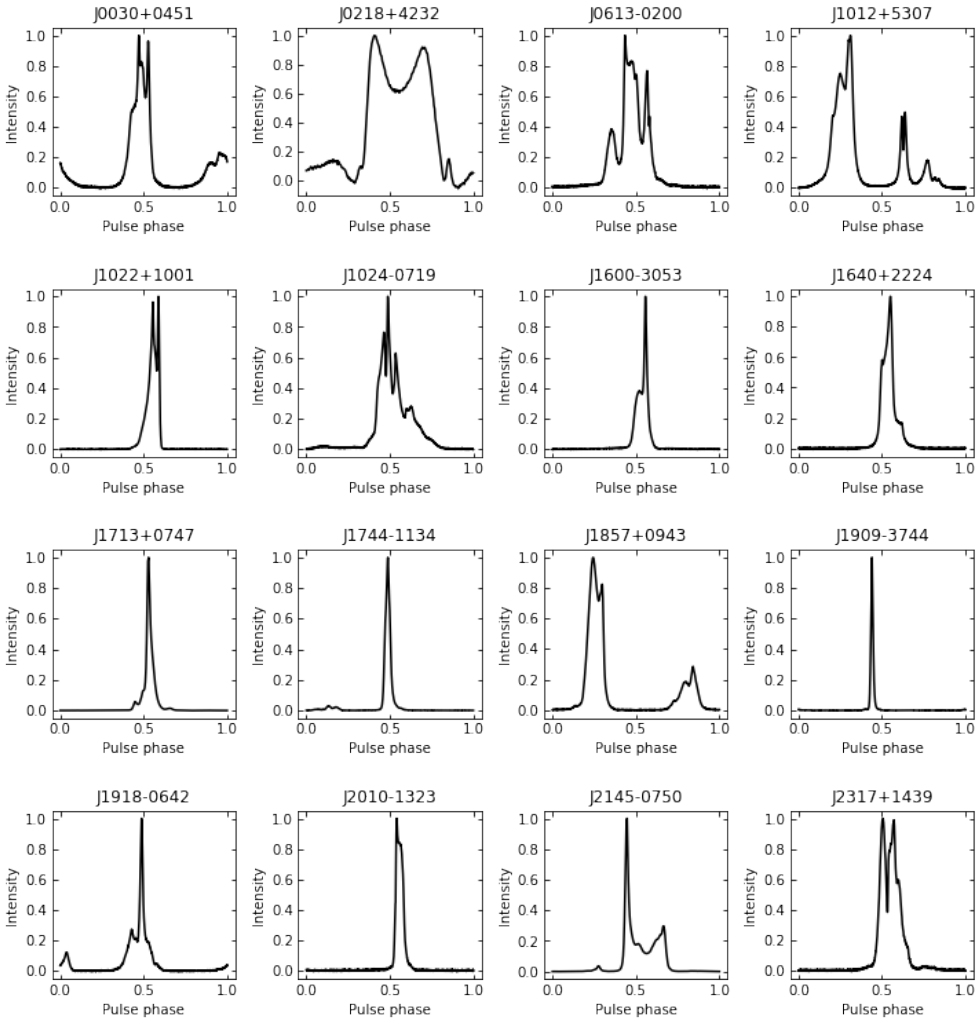

Figure A.1 Profiles of pulsars presented in this thesis.